MICROSCOPIC NUCLEON-NUCLEUS OPTICAL POTENTIALS FROM CHIRAL EFFECTIVE FIELD THEORY

A Dissertation

by

TAYLOR WHITEHEAD

Submitted to the Office of Graduate and Professional Studies of
Texas A&M University
in partial fulfillment of the requirements for the degree of

DOCTOR OF PHILOSOPHY

Chair of Committee,	Jeremy Holt
Committee Members,	Che-Ming Ko
	Dan Melconian
	Charles M. Folden III
Head of Department,	Girgory Rogachev

May 2021

Major Subject: Physics

ABSTRACT

In this dissertation I focus on my work in the development of nucleon-nucleus optical potentials calculated in the framework of many-body perturbation theory with nuclear forces from chiral effective field theory. Building upon previous calculations of the nucleon optical potential in nuclear matter my goal was to construct a global nucleon-nucleus optical potential, suitable for nuclei across the nuclear chart. In the first two works, neutron- and proton-calcium optical potentials are calculated and analyzed. Comparisons are made to experimental data, phenomenology, and other microscopic approaches. The next step was constructing the first microscopic global optical potential. Comparisons are again made, and we find key departures from phenomenology that support the idea that microscopic calculations are better suited for exotic nuclei for which there are no experimental data. Fermi liquid theory, a related many-body topic, is discussed. I end with brief outlines of applications of the optical potential including nucleon spectral functions and effective masses.

DEDICATION

For Lauren

ACKNOWLEDGMENTS

First and foremost, I would like to thank Jeremy Holt for giving me a chance to prove myself when the prospects of completing my Ph.D. were their dimmest. Thank you for your ever-present kindness and patience in mentoring me through my Ph.D.; I'm truly proud of the work we've accomplished in the past few years. Thanks are also due to Sherry Yennello and Lauren McIntosh for their work in managing the CENTAUR program. The peace and mental stability that having a research assistantship gave me significantly increased my productivity and I'm very grateful. I would also like to thank those whose help was truly invaluable along my physics journey; Sunny Guha for his companionship through the rough years of graduate school, Rafael de la Madrid for being an excellent teacher and mentor during my undergraduate years, and to my high school chemistry and physics teacher, Bryan Edwards, for his dedication to teaching at a remarkably high level and preparing the members of his UIL Science team so well for the future.

CONTRIBUTORS AND FUNDING SOURCES

Contributors

This work was supported by a dissertation committee consisting of Professor Jeremy Holt and Professor Che-Ming Ko and Professor Dan Melconian of the Department of Physics and Astronomy and Professor Charles M. Folden III of the Department of Chemistry.

All other work conducted for the dissertation was completed by the student independently.

Funding Sources

Work supported by the National Science Foundation under Grant No. PHY1652199 and by the U.S. Department of Energy National Nuclear Security Administration under Grant No. DE-NA0003841. Portions of this research were conducted with the advanced computing resources provided by Texas A&M High Performance Research Computing.

TABLE OF CONTENTS

Page

LIST OF FIGURES

FIGURE Page

LIST OF TABLES

TABLE Page

1. INTRODUCTION

1.1 Motivation

Exotic nuclei are at the frontier of research in nuclear physics due to their crucial role in the production of heavy elements at astrophysical sites such as neutron star mergers and core collapse supernovae. The experimental study of exotic isotopes across large regions of the nuclear chart will soon be possible for the first time at rare isotope beam facilities around the world. In an effort to facilitate scientific discovery in these experimental studies, the present proposal will develop next-generation optical potentials from chiral effective field theory (EFT) with robust uncertainty quantification. In my latest work, I demonstrate a proof-of-principle derivation of the first microscopic global optical potential. Whereas existing global optical potentials are fit exclusively to experimental data of stable isotopes and extrapolate to reactions involving exotic isotopes with an unknown degree of uncertainty, my approach is purely microscopic and with the addition of uncertainty quantification will be well suited to studying reactions with exotic isotopes. These microscopic optical potentials for exotic isotopes will improve our understanding of how elements are produced in astrophysical environments, contribute to a more consistent theoretical description of nuclear structure and reactions, and assist in scientific discovery in upcoming rare isotope beam experiments.

1.1.1 Astrophysical r-Process

Approximately half of the elements heavier than iron are produced in the rapid neutron capture process (r-process). The r-process occurs in environments with a high flux of neutrons that are captured by seed nuclei on a time scale faster than that of the β decay, allowing the nucleus to grow in mass through neutron-rich regions of the nuclear chart before decaying back to stability. Simulations of the r-process require knowledge of nuclear masses, decay rates, and neutron capture rates for a wide range of nuclei. Current calculations of r-process isotopic abundances have uncertainties of several orders of magnitude due to loosely constrained inputs, particularly neutron capture

rates. Implementation of improved neutron-nucleus optical potentials for these exotic isotopes will reduce neutron capture rate uncertainties, enabling r-process simulations to more accurately model element production and ultimately establish which astrophysical environments host the r-process.

1.1.2 Supernovae and Neutron Stars

The equation of state is an important input for models of core collapse supernovae and neutron star mergers. In both of these processes there is a low-density inhomogeneous mixed phase of dripped nucleons and nuclei. Current calculations of the equation of state for this phase typically do not consider nucleon-nucleus interactions; this can be addressed by the implementation of a global optical potential suitable for exotic nuclei.

1.1.3 Rare Isotope Beam Experiments

There is currently great interest in studying nuclear reactions with rare isotopes, however, these reactions are difficult to perform by conventional experimental methods due to the short half-lives of exotic isotopes. Rare isotope beam facilities capable of measuring reactions involving these exotic isotopes are soon to begin producing unprecedented amounts of reaction data. The analysis of these data from unexplored regions of the nuclear chart will require robust reaction models with quantified uncertainties.

1.1.4 Advances in Nuclear Theory

Chiral EFT provides a perturbative framework for calculating realistic nuclear interactions consistent with QCD. Recent advances have seen chiral EFT successfully applied in *ab initio* calculations of nuclear structure properties including binding energies, excited states, and estimations of the neutron drip line. My recent work utilizes the same chiral interactions in the context of nuclear reaction theory and is an initial step at tying together nuclear structure and nuclear reactions in a consistent framework for nuclei across the chart. The future development of nuclear reaction theory to incorporate theoretical uncertainty estimates is vital in the description of rare isotopes in regions of the nuclear chart where no experimental benchmarks exist.

1.2 Chiral Effective Field Theory

Quantum chromodynamics (QCD) is the theory of the strong nuclear force at the fundamental level of interactions with quarks and gluons. At the level of the nuclear many-body problem, the appropriate degrees of freedom are nucleons and pions. Chiral effective field theory (EFT) establishes a link between these two pictures by constructing a framework of nuclear forces that is consistent with the symmetries of QCD. This is done by determining the most general Lagrangian from these degrees of freedom that obeys the underlying symmetries

$$\mathcal{L}_{\text{EFT}} = \mathcal{L}_{\pi\pi} + \mathcal{L}_{\pi\mathcal{N}} + \mathcal{L}_{\mathcal{N}\mathcal{N}} + \ \ldots\ , \tag{1.1}$$

where the ellipsis refers to contributions with larger numbers of pions and nucleons.

In chiral EFT, the nuclear force is expressed as a perturbation expansion in powers of the nucleon momenta over the chiral symmetry breaking scale $(Q/\Lambda_\chi)^\nu$ in which diagrammatic contributions from the above Lagrangian are organized using a power counting scheme. This power counting scheme determines the order of a specific contribution according to the following expressions

$$\nu = -2 + 2N + 2(L - C) + \sum_i \Delta_i, \tag{1.2}$$

and

$$\Delta_i = d_i + \frac{n_i}{2} - 2, \tag{1.3}$$

where L is the number of loops, C is the number of connected pieces. In the sum, i goes over the vertices and d_i is the number of derivatives and n_i is the number of nucleon fields.

Diagrams from the first four orders of the chiral perturbation expansion are shown in Fig. 1.1. The most important contributions are at leading-order (LO) and next most important contributions are at next-to-leading-order (NLO) and so forth. This organizational scheme allows one to calculate

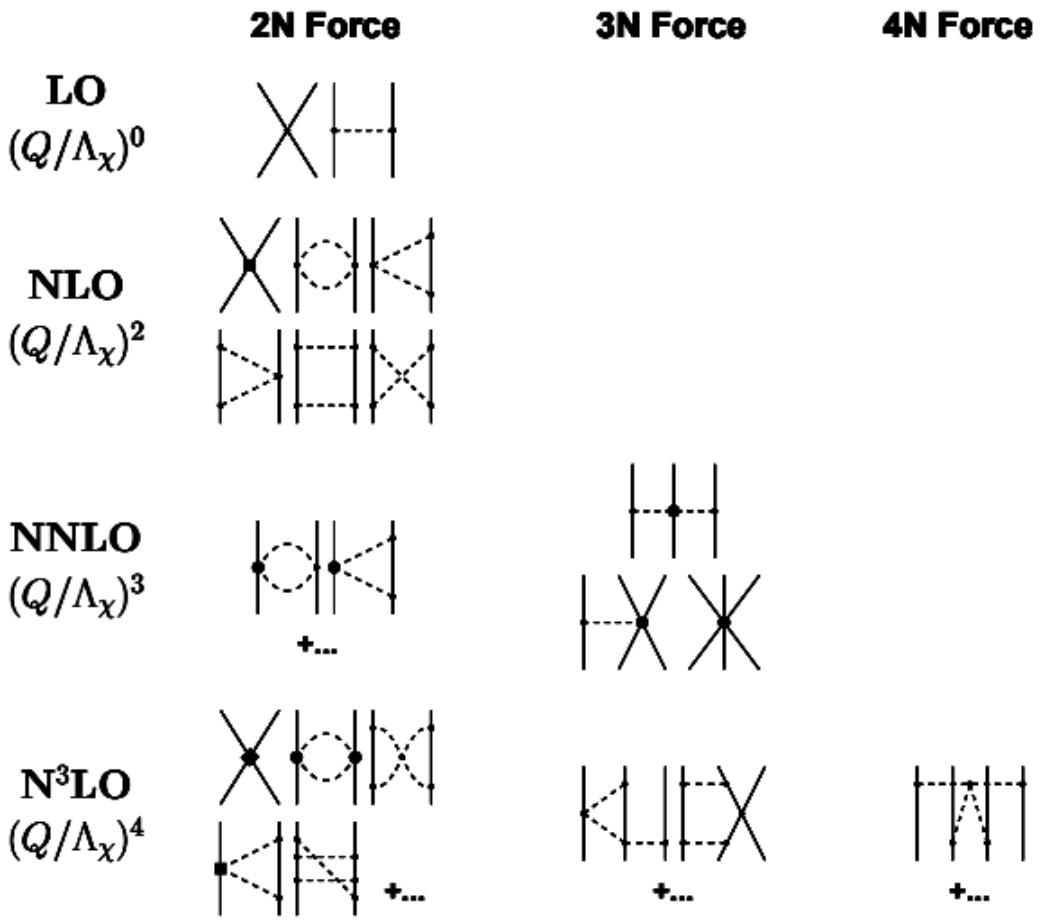

Figure 1.1: Contributions to nuclear forces in the chiral perturbation theory expansion. Solid lines are nucleons, dashed lines are pions, and symbols represent contact interactions.

nuclear forces to a desired accuracy by neglecting less significant high-order contributions. It turns out that no diagrams at the (Q/Λ_χ) order are consistent with the symmetries of the nuclear force and therefore do not contribute. It also clearly shows the empirically established fact that four-nucleon forces are smaller than three-nucleon forces (4NF < 3NF) and three-nucleon forces are smaller than two-nucleon forces (3NF < 2NF). The contact interactions represent non-perturbative nuclear dynamics that take place beyond the cutoff scale of the theory; each one introduces a so-called low energy constant (LEC) that is not predicted by chiral EFT. These LECs give scale to the theory and must be either derived from the underlying physics (QCD) or empirically measured. Currently they are determined from measurements of nucleon-nucleon scattering and in the case

of three-body interactions, the triton binding energy and lifetime. In the future these LECs may be calculated in lattice QCD, but currently major challenges stand in the way of these calculations. Since nuclear forces from chiral effective field theory used in the current text are fit only to two- and three-body empirical measurements, calculations made at the nuclear many-body level are predictions. In addition to the uncertainty due to the LECs, uncertainties also arise in chiral EFT from the chosen cutoff scale and order at which the chiral expansion is truncated. By varying the cutoff scale and truncation order of the potential, one may estimate the theoretical uncertainty in the prediction of a given measurable quantity. Obtaining theoretical uncertainty estimates of scattering observables calculated from chiral EFT is a promising way of addressing the current lack of uncertainty quantification in nuclear reaction theory. For more details on chiral EFT see Ref. [2].

1.3 Many Body Perturbation Theory

Many body perturbation theory is utilized in nuclear matter to study bulk properties. Nuclear matter is an infinite system of interacting nucleons at a given density and isospin asymmetry (relative composition of neutrons and protons). The energy per nucleon as a function of density is called the nuclear equation of state (EOS) and is the fundamental quantity of nuclear matter. Many properties of nuclear matter can be extracted from the EOS such as binding energy, saturation density, slope of the symmetry energy, and incompressibility. Much work has recently gone into the improvement of EOS calculations and specifically quantifying their uncertainties. Starting from the energy of nuclear matter, additional many-body quantities may be derived. These include the self-energy and the quasiparticle interaction. At second order in many-body perturbation theory all three of these quantities have single-particle energies in their denominators. Since the single-particle energy depends on the self-energy

$$\epsilon(q) = \frac{q^2}{2M} + \mathrm{Re}\Sigma(q, \epsilon(q)), \tag{1.4}$$

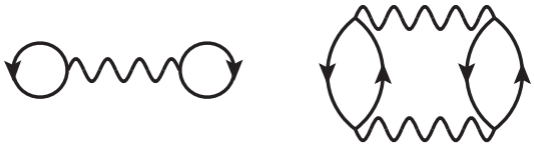

Figure 1.2: Diagrammatic representations of the first and second order contributions to the energy per nucleon. The solid lines represent nucleon propagators and the wavy lines represent the in-medium two-nucleon interaction.

the equation of state and the quasiparticle both depend on the self-energy, while the self-energy requires a self-consistent calculation at second order. Therefore the development in calculations of the nucleon self-energy may have broad impacts on the field of nuclear physics through these related many-body quantities.

1.3.1 Equation of State

The first and second order contributions of the equation of state calculated in many-body perturbation theory are given by

$$E^{(1)} = \frac{1}{2}\sum_{12}\langle 12|\overline{V}|12\rangle n_1 n_2, \tag{1.5}$$

and

$$E^{(2)} = -\frac{1}{4}\sum_{1234}|\langle 12|\overline{V}|34\rangle|^2 \frac{n_1 n_2 \overline{n}_3 \overline{n}_4}{\epsilon_3 + \epsilon_4 - \epsilon_1 - \epsilon_2}, \tag{1.6}$$

with the single-particle energies ϵ given by Eq. 1.4. The occupation probability is given by $n_i = \theta(k_f - k_i)$ for states below the Fermi surface and $\bar{n}_i = \theta(k_i - k_f)$ for states above the Fermi surface.

The diagrammatic representations of the first and second order contributions to the energy per particle are shown in Fig. 1.2. The equation of state calculated to first, second, and third order shown in Fig. 1.3 indicates that second order in many-body perturbation theory is well converged.

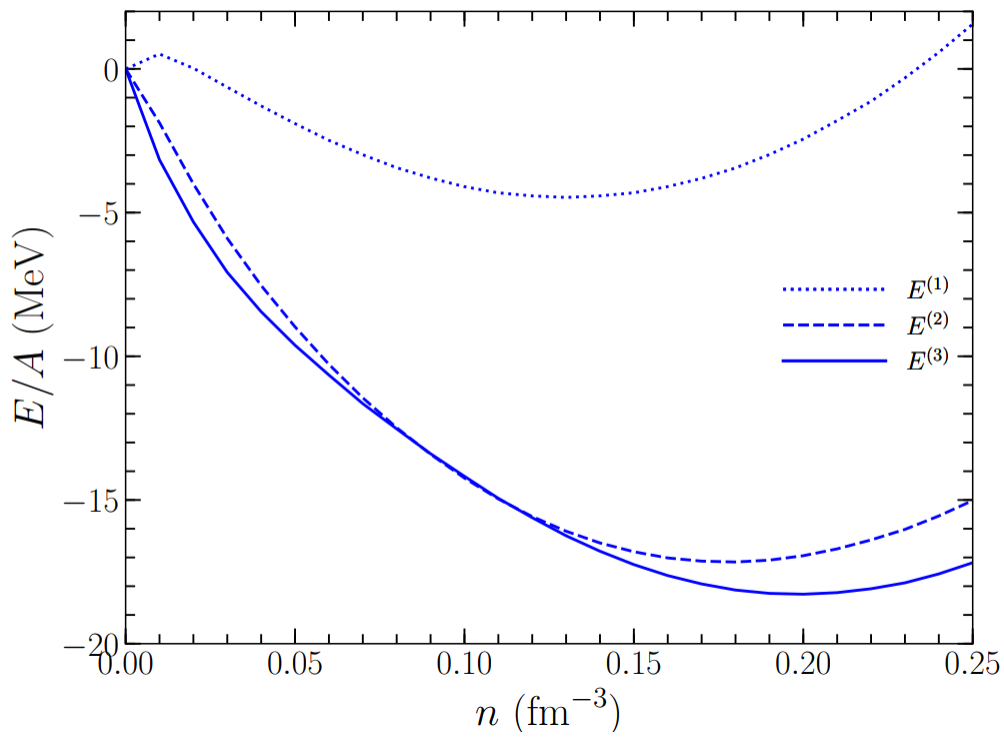

Figure 1.3: The equation of state at first, second and third order calculated in symmetric nuclear matter from many-body perturbation theory with nuclear forces from chiral effective field theory.

The nuclear equation of state has far reaching applicability and is a key quantity in the study of neutron star properties, supernova evolution, and heavy ion collisions.

1.3.2 Self-Energy

The nucleon single-particle energy may be related to the self-energy Σ by the on-shell energy relation $\epsilon_p = \frac{p^2}{2M} + \Sigma(p, \epsilon_p; k_f)$. The first and second order contributions of the self-energy calculated in many-body perturbation theory are given by

$$\Sigma^{(1)}_{2N} = \sum_1 \langle \vec{q}\vec{h}_1 s s_1 t t_1 | \overline{V}_{2N} | \vec{q}\vec{h}_1 s s_1 t t_1 \rangle n_1, \tag{1.7}$$

and

$$\Sigma^{(2)}_{2N} = \frac{1}{2} \sum_{123} \frac{|\langle \vec{p}_1\vec{p}_3 s_1 s_3 t_1 t_3 | \overline{V}_{2N} | \vec{q}\vec{h}_2 s s_2 t t_2 \rangle|^2}{\omega + \epsilon_2 - \epsilon_1 - \epsilon_3 + i\eta} \bar{n}_1 n_2 \bar{n}_3. \tag{1.8}$$

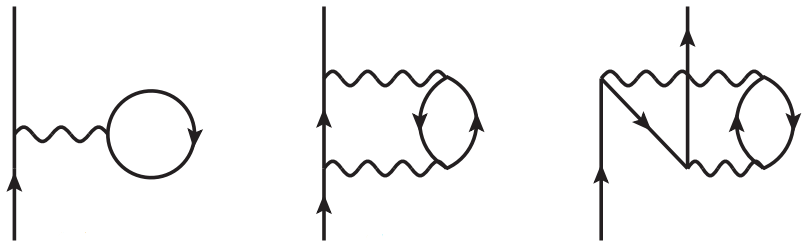

Figure 1.4: Diagrammatic representations of the first and second order contributions to the self-energy. The solid lines represent nucleon propagators and the wavy lines represent the in-medium two-nucleon interaction.

The diagrammatic representations of the first and second order contributions to the self-energy are shown in Fig. 1.4. For positive energies, the self-energy is equivalent to the optical potential. The nuclear matter optical potential may then be used in the local density approximation to derive optical potentials for finite nuclei, this will be the focus of this dissertation.

1.3.3 Quasiparticle Interaction

The quasiparticle interaction is the key quantity in Fermi liquid theory which describes low lying excited states of systems of strongly interacting particles. The first and second order contributions of the quasiparticle interaction calculated in many-body perturbation theory are given by

$$\mathcal{F}_{2N}^{(1)} = \langle 12|\overline{V}_{2N}|12\rangle, \tag{1.9}$$

and

$$\mathcal{F}_{2N}^{(2pp)} = \frac{1}{2}\sum_{mn}\frac{|\langle 12|\overline{V}_{2N}|mn\rangle|^2\bar{n}_m\bar{n}_n}{\epsilon_1+\epsilon_2-\epsilon_m-\epsilon_n}. \tag{1.10}$$

The diagrammatic representations of the first and second order contributions to the quasiparticle interaction are shown in Fig. 1.5. Through Fermi liquid theory the quasiparticle interaction may be utilized to calculate many properties of nuclear systems including the effective mass, symmetry

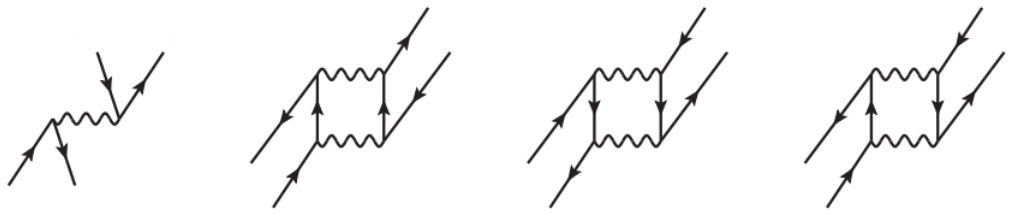

Figure 1.5: Diagrammatic representations of the first and second order contributions to the quasi-particle interaction. The solid lines represent nucleon propagators and the wavy lines represent the in-medium two-nucleon interaction.

energy, and incompressibility.

2. PROTON ELASTIC SCATTERING ON CALCIUM ISOTOPES FROM CHIRAL NUCLEAR OPTICAL POTENTIALS*

We formulate microscopic optical potentials for nucleon-nucleus scattering from chiral two- and three-nucleon forces. The real and imaginary central terms of the optical potentials are obtained from the nucleon self-energy in infinite nuclear matter at a given density and isospin asymmetry, calculated self-consistently to second order in many-body perturbation theory. The real spin-orbit term is extracted from the same chiral potential using an improved density matrix expansion. The density-dependent optical potential is then folded with the nuclear density distributions of ^{40,42,44,48}Ca from which we study proton-nucleus elastic scattering and total reaction cross sections using the reaction code TALYS. We compare the results of the microscopic calculations to those of phenomenological models and experimental data up to projectile energies of $E = 180$ MeV. While overall satisfactory agreement with the available experimental data is obtained, we find that the elastic scattering and total reaction cross sections can be significantly improved with a weaker imaginary optical potential, particularly for larger projectile energies since the density of available states in nuclear matter is larger than in a nucleus. This leads to an imaginary term that is overestimated when utilizing nuclear matter calculations.

2.1 Introduction

Nucleon-nucleus optical potentials are a valuable tool for predicting a wide range of scattering and reaction processes by replacing the complicated many-body dynamics of nucleons interacting through two- and three-body forces with an average complex, energy-dependent single-particle potential. Global phenomenological optical potentials [3, 4] have been constructed by fitting to experimental data spanning a large range of projectile energies across many nuclei. Although phenomenological optical potentials are very successful at describing scattering processes involving

*Reprinted with permission from "Proton elastic scattering on calcium isotopes from chiral nuclear optical potentials" by T.R. Whitehead, Y. Lim, J.W. Holt, 2019. Phys.Rev.C, 100, 014601 , Copyright [2019] American Physical Society.

nuclei near stability, microscopic optical potentials are not tuned to experimental data and therefore may have greater predictive power for reactions involving exotic isotopes.

Semi-microscopic global optical potentials [5, 6] derived in the 1970's from high-precision one-boson-exchange nucleon-nucleon interactions are still widely used today [7, 8, 9]. Whereas the density and isospin-asymmetry dependence is computed microscopically, the overall strengths of the real and imaginary volume terms are often adjusted with energy-dependent empirical strength factors. The effects of three-body forces were generally neglected in these early works, and within the original nuclear matter approach no spin-orbit optical potential could be derived. More recently, three-body forces have been implemented [10, 11, 12] in calculations of the real and imaginary central terms, while phenomenological spin-orbit optical potentials have been added [13, 9, 14] in order to better describe analyzing powers and differential cross sections at large scattering angles. The spin-orbit term makes up a larger contribution at higher scattering angles since they are associated with higher values of angular momentum. An alternative approach [15, 16, 17, 18, 19, 20, 21, 22] to constructing microscopic optical potentials is based on multiple scattering theory involving the nucleon-nucleon T-matrix. Such an approach naturally generates a spin-orbit contribution, but the implementation of medium effects [23, 24] and three-body forces remains challenging, which in practice often limits the theory to large scattering energies $E > 200\,\mathrm{MeV}$. Other current approaches to deriving predictive optical potentials include the self-consistent Green's function method [25] and the dispersive optical model [26].

Recently there has been much interest in the development of microscopic optical potentials [10, 27, 12, 28, 29, 22, 30, 31] based on chiral effective field theory (EFT) [32, 33, 2]. The main motivation is to implement more realistic microphysics involving multi-pion exchange contributions to the nuclear force, three-body interactions, and theoretical uncertainty estimates. Chiral optical potentials are well suited to describe low-energy scattering processes but are expected to break down for energies approaching the relevant momentum-space cutoff employed. In practice, the presence of the cutoff constrains nucleon projectile energies to lie below $E < 200\,\mathrm{MeV}$.

In the present study, we aim to lay the groundwork for a revised nuclear matter description of

the global nucleon-nucleus optical potential based on chiral EFT. Ultimately the goal will be to develop a theory for nucleon-nucleus scattering across a large range of isotopes, including those off stability, at energies up to 200 MeV. As a starting point we consider differential elastic and total reaction cross sections for proton-nucleus scattering along a chain of calcium isotopes, ^{40,42,44,48}Ca, at energies ranging from 2-160 MeV where experimental data are available. We also compare to the global phenomenological optical potential of Koning and Delaroche [4] and investigate to what extent modern phenomenological parametrizations of the optical potential are consistent with microscopic analyses. Our calculations are performed within the TALYS [34] reaction code for which we have developed an implementation of our microscopic optical potential.

We take as a starting point for the calculation a particular high-precision 2N + 3N chiral nuclear potential with momentum-space cutoff $\Lambda = 450\,\mathrm{MeV}$. The low-energy constants of the potential are fitted to nucleon-nucleon scattering phase shifts, deuteron properties, and in the case of three-body contact terms also the triton binding energy and lifetime. The nucleon-nucleon interaction is taken at next-to-next-to-next-to-leading order (N3LO), while only the N2LO three-nucleon force is included. The inconsistent treatment of two- and three-body forces at the level of the chiral expansion is undesirable, but work toward fully consistent two- and many-body forces is in progress [35, 36, 37]. We note that the chiral nuclear potential employed in the present work exhibits good nuclear matter properties (saturation energy and density [38], thermodynamics [39, 40], and Fermi liquid parameters [41]) when calculated at least to second order in many-body perturbation theory.

In quantum many-body theory, the optical potential for scattering states is identified with the energy- and momentum-dependent single-particle self-energy [42]. We first compute the nucleon self-energy in homogeneous nuclear matter at arbitrary density and composition (proton fraction) from chiral two- and three-body forces to second order in many-body perturbation theory. We next compute nuclear density distributions for selected calcium isotopes (^{40}Ca, ^{42}Ca, ^{44}Ca, ^{48}Ca) from mean field theory employing recently derived [43] Skyrme effective interactions constrained by chiral effective field theory. In the local density approximation (LDA) the nucleon-nucleus optical potential is computed [44] by folding the nucleon self-energy in homogeneous matter with the

derived density distributions. Since the LDA is known [44] to underestimate the surface diffuseness of the optical potential in finite nuclei, we employ the improved local density approximation (ILDA) described in Refs. [44, 9] to account for the non-zero range of the nuclear force.

The method outlined thus far is versatile since it can be used to produce optical potentials for a very wide range of nuclei. However, the LDA nuclear matter approach cannot capture the physics of collective surface modes, shell effects [45], and surface-peaked spin-orbit optical potentials. The latter are particularly important for spin observables and elastic scattering cross sections at large angles. In the present work we therefore construct a spin-orbit optical potential from the improved density matrix expansion [46, 47, 48], which improves the description of the spin-dependent part of the energy density functional compared to the standard density matrix expansion of Negele and Vautherin [49]. We then benchmark our approach to experimental data for proton elastic scattering and total reaction cross sections on the calcium isotopes ^{40}Ca, ^{42}Ca, ^{44}Ca, ^{48}Ca.

2.2 Optical potential from chiral effective field theory

2.2.1 Real and imaginary central terms

In recent work [10, 12] the nucleon self-energy in homogeneous nuclear matter has been computed employing a set of nuclear potentials derived from chiral effective field theory. The first- and second-order perturbative contributions to the nucleon self-energy are shown graphically in Fig. 1.4 and given quantitatively by

$$\Sigma^{(1)}_{2N}(q;k_f) = \sum_1 \langle \vec{q}\,\vec{h}_1 s s_1 t t_1 | \bar{V}^{\rm eff}_{2N} | \vec{q}\,\vec{h}_1 s s_1 t t_1 \rangle n_1, \tag{2.1}$$

$$\begin{aligned}&\Sigma^{(2a)}_{2N}(q,\omega;k_f) \\ &= \frac{1}{2}\sum_{123} \frac{|\langle \vec{p}_1\vec{p}_3 s_1 s_3 t_1 t_3 | \bar{V}^{\rm eff}_{2N} | \vec{q}\vec{h}_2 s s_2 t t_2 \rangle|^2}{\omega + \epsilon_2 - \epsilon_1 - \epsilon_3 + i\eta} \bar{n}_1 n_2 \bar{n}_3,\end{aligned} \tag{2.2}$$

$$\Sigma_{2N}^{(2b)}(q,\omega;k_f) \tag{2.3}$$
$$= \frac{1}{2}\sum_{123} \frac{|\langle \vec{h}_1\vec{h}_3 s_1 s_3 t_1 t_3|\bar{V}_{2N}^{\rm eff}|\vec{q}\vec{p}_2 s s_2 t t_2\rangle|^2}{\omega+\epsilon_2-\epsilon_1-\epsilon_3-i\eta} n_1\bar{n}_2 n_3,$$

where n_i is the occupation probability $\theta(k_f - k_i)$ for a filled state with momentum $\vec{k}_i$ below the Fermi surface, the occupation probability for particle states is $\bar{n}_i = \theta(k_i - k_f)$, the summation is over intermediate-state momenta for particles $\vec{p}_i$ and holes $\vec{h}_i$, their spins s_i, and isospins t_i. The nuclear potential $\bar{V}_{2N}^{\rm eff}$ represents the antisymmetrized two-body interaction consisting of the bare nucleon-nucleon (NN) potential V_{NN} together with an effective, medium-dependent NN interaction $V_{NN}^{\rm med}$ derived from the N2LO chiral three-nucleon force by averaging one particle over the filled Fermi sea of noninteracting nucleons [50, 51, 52]. In the first-order Hartree-Fock contribution, Eq. (2.1), the effective interaction is given by $\bar{V}_{2N}^{\rm eff} = V_{NN} + \frac{1}{2}V_{NN}^{\rm med}$, while for the higher-order contributions, Eqs. (2.2) and (2.3), the effective interaction is given by $\bar{V}_{2N}^{\rm eff} = V_{NN} + V_{NN}^{\rm med}$. The factor of $1/2$ at first order prevents double counting of contributions to $V_{NN}^{\rm med}$. The Hartree-Fock contribution is nonlocal, energy-independent, and purely real, while the second-order contributions are in general nonlocal, energy-dependent, and complex. The single-particle energies in the denominators of Eqs. (2.2) and (2.3) are computed self-consistently according to $\epsilon(q) = \frac{q^2}{2M} + {\rm Re}\Sigma(q,\epsilon(q))$where M is the free-space nucleon mass.

In the present work the self-energy is computed for arbitrary isospin-asymmetry, $\delta_{np} = (\rho_n - \rho_p)/(\rho_n + \rho_p)$, which is essential for an accurate description of nuclei for which $N \neq Z$. The resulting optical potentials for nucleons propagating in homogeneous matter characterized by its proton and neutron Fermi momenta k_f^p and k_f^n are given by

$$\begin{aligned} U_p(E;k_f^p,k_f^n) &= V_p(E;k_f^p,k_f^n) + iW_p(E;k_f^p,k_f^n), \\ U_n(E;k_f^p,k_f^n) &= V_n(E;k_f^p,k_f^n) + iW_n(E;k_f^p,k_f^n) \end{aligned} \tag{2.4}$$

with

$$V_i(E;k_f^p,k_f^n) = {\rm Re}\Sigma_i(q,E(q);k_f^p,k_f^n), \tag{2.5}$$

$$W_i(E;k_f^p,k_f^n) = \frac{M_i^{k*}}{M}\mathrm{Im}\Sigma_i(q,E(q);k_f^p,k_f^n), \tag{2.6}$$

where the subscript i denotes a propagating proton or neutron. In relating the physical imaginary part of the optical potential to the imaginary part of the nucleon self-energy we have multiplied [53, 54] by the effective k-mass M_i^{k*} defined by

$$\frac{M_i^{k*}}{M} = \left(1 + \frac{M}{k}\frac{\partial}{\partial k}V_i(k,E(k))\right)^{-1}, \tag{2.7}$$

in order to account for the non-locality of the optical potential.

2.2.2 Spin-orbit optical potential

The effective one-body spin-orbit interaction vanishes in homogeneous nuclear matter and therefore cannot be computed within the framework described above. Instead we employ an improved density matrix expansion [47, 55, 48] to construct the one-body spin-orbit interaction from chiral two- and three-body forces. The improved density matrix expansion takes advantage of phase space averaging to derive a more accurate spin-dependent energy density functional compared to the standard density matrix expansion of Negele-Vautherin [49].

From the definition of the density matrix

$$\rho(\vec{r}_1\sigma_1\tau_1;\vec{r}_2\sigma_2\tau_2) = \sum_\alpha \Psi_\alpha^*(\vec{r}_2\sigma_2\tau_2)\Psi_\alpha(\vec{r}_1\sigma_1\tau_1), \tag{2.8}$$

where Ψ_α are energy eigenfunctions associated with occupied orbitals of the non-relativistic many-body system, the energy density functional for $N = Z$ even-even nuclei in the Hartree-Fock approximation can be expanded up to second order in spatial gradients as

$$\begin{aligned}\mathcal{E}[\rho,\tau,\vec{J}] &= \rho\,\bar{E}(\rho) + \left[\tau - \frac{3}{5}\rho k_f^2\right]\left[\frac{1}{2M_N} + F_\tau(\rho)\right] \\ &\quad + (\vec{\nabla}\rho)^2\,F_\nabla(\rho) + \vec{\nabla}\rho\cdot\vec{J}\,F_{SO}(\rho) + \vec{J}^{\,2}\,F_J(\rho)\,,\end{aligned} \tag{2.9}$$

where $\rho(\vec{r}) = 2k_f^3(\vec{r})/3\pi^2 = \sum_\alpha \Psi_\alpha^\dagger(\vec{r})\Psi_\alpha(\vec{r})$ defines the local density with $k_f(\vec{r})$ the local

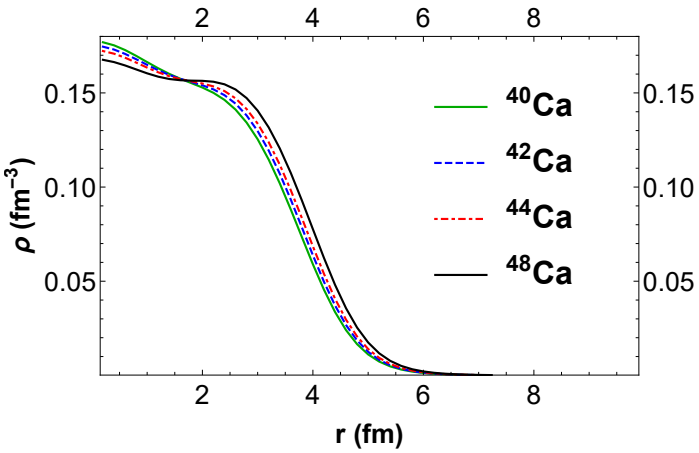

Figure 2.1: The nucleon density distributions for ^{40,42,44,48}Ca calculated in mean field theory from the Skyrme Skχ450 effective interaction constrained by chiral effective field theory. Reprinted from [77].

Fermi momentum, $\tau(\vec{r}) = \sum_\alpha \vec{\nabla}\Psi^\dagger_\alpha(\vec{r}) \cdot \vec{\nabla}\Psi_\alpha(\vec{r})$ is the kinetic energy density, and $\vec{J}(\vec{r}) = i\sum_\alpha \vec{\Psi}^\dagger_\alpha(\vec{r})\vec{\sigma} \times \vec{\nabla}\Psi_\alpha(\vec{r})$ is the spin-orbit density. These terms are multiplied by the density-dependent strength functions $\bar{E}(\rho), F_\tau(\rho), F_\nabla(\rho), F_{SO}(\rho), F_J(\rho)$, of which we are presently only interested in the spin-orbit term $F_{SO}(\rho)$. In effect, the spin-orbit optical potential is therefore calculated for $N = Z$ nuclei to first order in many-body perturbation theory. In the future, higher-order perturbative contributions [56] to the microscopic nuclear energy density functional may be investigated. We note that we do not include the isovector part [57] of the spin-orbit interaction for $N \neq Z$ nuclei in this study since it is known to be small compared to the isoscalar part [48].

2.2.3 Improved local density approximation

We employ the improved local density approximation (ILDA) to construct the nucleon-nucleus optical potential for finite nuclei. The density dependent optical potential (both central and spin-orbit parts) is folded with the radial density distribution of a target nucleus. The nuclear density distributions are calculated within mean field theory from the Skχ450 Skyrme interaction [43], which fits both finite nuclei properties as well as theoretical calculations of the asymmetric nuclear matter equation of state from the N3LO $\Lambda = 450$ MeV chiral potential used in the calculation of the self-energy. In Fig. 2.1 we show the resulting nucleon density distributions for each of the

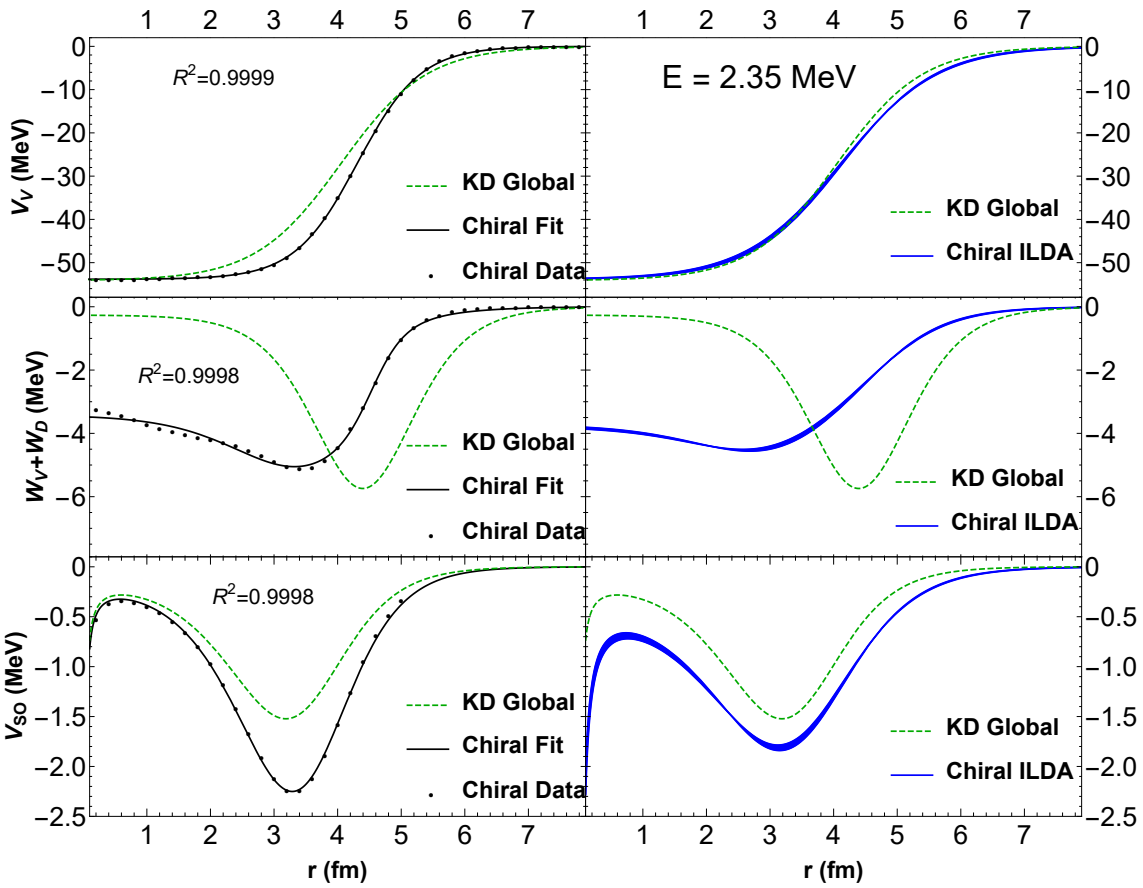

Figure 2.2: Left (right): The real, imaginary, and spin-orbit terms of the microscopic optical potential for proton-^{40}Ca scattering at $E = 2.35$ MeV before (after) applying the improved local density approximation. In the left panel the dots represent raw results from chiral EFT, while the solid black lines represent fits to the Koning-Delaroche (KD) form. We also compare to the global KD phenomenological optical potential, shown as the dashed green line, at the same energy. Reprinted from [77].

calcium isotopes ^{40}Ca, ^{42}Ca, ^{44}Ca, ^{48}Ca.

In the standard local density approximation, the strength of the nucleon-nucleus optical potential at a given radial distance r is evaluated as

$$V(E;r) + iW(E;r) = V(E;k_f^p(r), k_f^n(r)) \\ +iW(E;k_f^p(r), k_f^n(r)), \tag{2.10}$$

where $k_f^p(r)$ and $k_f^n(r)$ are the local proton and neutron Fermi momenta. This approximation

is strictly valid only for zero-range nuclear forces, and when applied to nucleon-nucleus optical potentials it is known to underestimate the surface diffuseness [58, 44]. Consequently, such an approach is inadequate for an accurate description of nuclear elastic scattering and reaction processes. The improved local density approximation applies a Gaussian smearing

$$V(E;r)_{ILDA} = \frac{1}{(t\sqrt{\pi})^3}\int V(E;r')e^{\frac{-|\vec{r}-\vec{r}'|^2}{t^2}}d^3r' \tag{2.11}$$

characterized by an adjustable length scale t associated with the non-zero range of the nuclear force. In the limiting case of $t \to 0$, a factor of $\delta(|\vec{r}-\vec{r'}|)$ replaces the Gaussian, giving $V_{ILDA}(E;r) \to V(E;r)$. In Ref. [9] it is found that for the central part of the interaction $t_C = 1.2\,\mathrm{fm}$ gives the best fit to experimental reaction cross sections for $10\,\mathrm{MeV} < E < 200\,\mathrm{MeV}$ and targets ranging from ^{40}Ca to ^{208}Pb. In the present work we vary the range parameter $1.15\,\mathrm{fm} < t_C < 1.25\,\mathrm{fm}$. This variation is used to estimate the theoretical uncertainty associated with our choice of the length scale t_C. For the spin-orbit part of the optical potential, we estimate the range parameter t_{SO} from the root mean square radius of the Argonne v_{18} spin-orbit nucleon-nucleon potential [59]. We found $t_{SO} = 1.07$ fm and took two values, $t_{SO} = 1.0, 1.1$ fm to estimate the uncertainty.

In Figs. 2.2 and 2.3 we show the comparison between the central and spin-orbit optical potentials in the LDA (left panels) and ILDA (right panels) for the proton-^{40}Ca optical potential at projectile energies $E = 2.35\,\mathrm{MeV}$ and $E = 35\,\mathrm{MeV}$ respectively. In the left panels, the dots indicate the results from chiral effective field theory, and for comparison we show as the green dashed lines the phenomenological optical potentials from Koning and Delaroche [4]. In particular, the real central part of the microscopic optical potential has a much smaller surface diffuseness compared to phenomenology. When the improved local density approximation is employed in the right panels (solid blue bands), the comparison to phenomenology is much improved. In addition, the overall strength of the real central part of the optical potential is in very good agreement with the Koning-Delaroche phenomenological optical potential. Varying the ILDA range parameter t_C between $1.15\,\mathrm{fm}$ and $1.25\,\mathrm{fm}$ yields only a small change in the overall shape of the real central

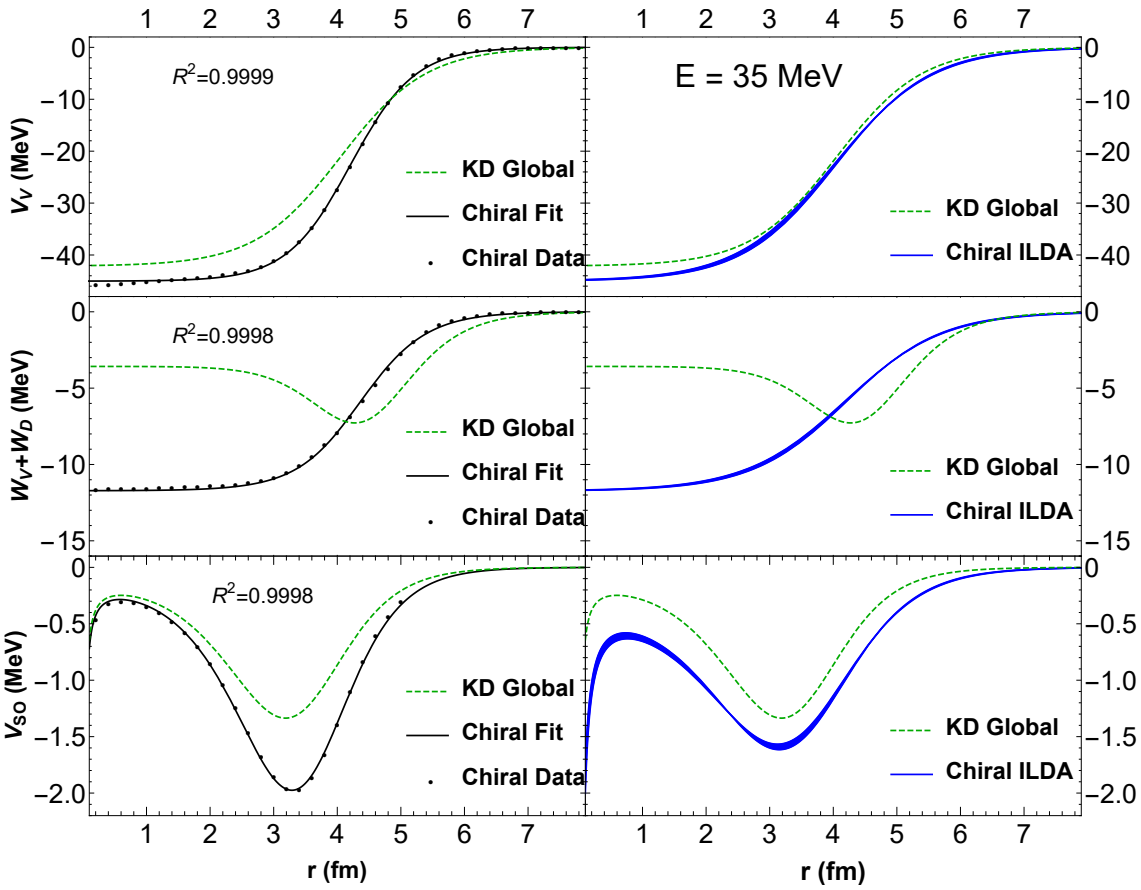

Figure 2.3: Same as Fig. 2.2, except that the projectile energy is $E = 35\,\text{MeV}$. Reprinted from [77].

part, which suggests that the theoretical predictions for scattering cross sections computed in the next section will not be especially sensitive to the precise choice of t_C.

In the middle panels of Figs. 2.2 and 2.3 we plot the imaginary part of the microscopic optical potential for proton-^{40}Ca scattering at $E = 2.35\,\text{MeV}$ and $E = 35\,\text{MeV}$. This is again compared to the phenomenological optical potential of Koning and Delaroche, which is written as the sum of a volume imaginary part W_V and a surface imaginary part W_D. In the microscopic description of the imaginary part, there is no distinction between these two components. We observe that in contrast to the real central part of the optical potential, the microscopic imaginary part exhibits large qualitative differences compared to phenomenology. The most striking difference is a much smaller surface peak, which only appears at low projectile energies in the microscopic calculation

but persists to much higher energies ($E \simeq 100\,\text{MeV}$) in the phenomenological optical potential. For instance, at the scattering energy $E = 35\,\text{MeV}$, the surface peak has essentially vanished in the microscopic calculation, and the remaining "volume" imaginary part is large compared to phenomenology. In fact, this is a common feature [6, 60, 61, 8] in microscopic optical potentials computed in the nuclear matter approach. Modern semi-microscopic optical potentials therefore include empirical energy-dependent strength factors multiplying the real and imaginary central parts [9, 62].

In the bottom panels of Figs. 2.2 and 2.3 we show the real spin-orbit part of the microscopic optical potential compared to the Koning-Delaroche phenomenological optical potential for proton-^{40}Ca scattering at $E = 2.35\,\text{MeV}$ and $E = 35\,\text{MeV}$. The radial shape of the microscopic spin-orbit optical potential is found to be very similar to that of the Koning-Delaroche optical potential, however, the strength of the microscopic potential is larger. Indeed, the density matrix expansion carried out at the Hartree-Fock level is known [48, 63] to produce a stronger spin-orbit interaction, by about 20-50%, than is required from traditional mean field theory studies of finite nuclei. Higher-order perturbative contributions are expected to remedy this feature. In particular, multi-pion-exchange processes have been shown [64] to reduce the strength of the one-body spin-orbit interaction in finite nuclei. This provides additional motivation for including G-matrix correlations in the density matrix expansion as outlined in [56]. As in the case of the central components of the optical potential, we find relatively small differences between spin-orbit potentials produced with two choices of the ILDA length scale $t_{SO} = 1.0, 1.1\,\text{fm}$.

2.2.4 Parameterization of the chiral optical potential

In order to facilitate the implementation of our microscopic optical potential into standard nuclear reaction codes, such as TALYS, we fit our optical potential to the phenomenological form of Koning and Delaroche. Eventually our aim is to construct a global microscopic optical potential and make it available in a convenient form for nuclear reaction practitioners. This exercise may also help to reveal any deficiencies in the assumed form of phenomenological optical potentials.

Table 2.1: Shape parameters for the proton-^{40}Ca microscopic optical potential at the three energies $E = 2.35, 35, 100$ MeV. Also shown are the corresponding shape parameters for the Koning-Delaroche (KD) optical potential that are independent of energy. Reprinted from [77].

$E = 2.35$ MeV	V_V	W_V	V_{SO}
r (fm)	1.213	1.344	1.015
a (fm)	0.723	0.583	0.706
$E = 35$ MeV	V_V	W_V	V_{SO}
r (fm)	1.183	1.204	1.015
a (fm)	0.730	0.751	0.706
$E = 100$ MeV	V_V	W_V	V_{SO}
r (fm)	1.173	0.846	1.015
a (fm)	0.713	0.702	0.706
KD	V_V	W_V	V_{SO}
r (fm)	1.185	1.185	0.996
a (fm)	0.672	0.672	0.590

We recall that in the phenomenological description, the optical potential takes the form

$$U(r,E) = V_V(r,E) + iW_V(r,E) + iW_D(r,E) \\ +V_{SO}(r,E)\vec{\ell}\cdot\vec{s} + iW_{SO}(r,E)\vec{\ell}\cdot\vec{s} + V_C(r), \tag{2.12}$$

consisting of a real volume term, an imaginary volume and surface term, a real and imaginary spin-orbit term, and finally the central Coulomb interaction. In Eq. (2.12), $\vec{\ell}$ and $\vec{s}$ are the single-particle orbital angular momentum and spin angular momentum operators, respectively. Since the phenomenological imaginary spin-orbit term is very small and cannot be extracted within the present microscopic approach, we neglect it in the rest of the discussion. The energy and radial dependence of the different terms in the phenomenological optical potential are assumed to factorize according to

$$V_V(r,E) = \mathcal{V}_V(E) f(r; r_V, a_V), \tag{2.13}$$

$$W_V(r,E) = \mathcal{W}_V(E) f(r; r_W, a_W), \tag{2.14}$$

$$W_D(r,E) = -4a_D \mathcal{W}_D(E) \frac{d}{dr} f(r; r_D, a_D), \tag{2.15}$$

$$V_{SO}(r,E) = \mathcal{V}_{SO}(E) \frac{1}{m_\pi^2} \frac{1}{r} \frac{d}{dr} f(r; r_{SO}, a_{SO}), \tag{2.16}$$

where

$$f(r; r_i, a_i) = \frac{1}{1 + e^{(r - A^{1/3} r_i)/a_i}} \tag{2.17}$$

is of the Woods-Saxon form with A the mass number and $\{r_i$,$a_i\}$ the energy-independent geometry parameters that encode the size and diffuseness of a given target nucleus, respectively. In phenomenological optical potentials, these shape parameters vary weakly with the target nucleus. The energy-dependent strength functions in the KD parametrization have the form

$$\mathcal{V}_V(E) = v_1(1 - v_2\tilde{E} + v_3\tilde{E}^2 - v_4\tilde{E}^3), \tag{2.18}$$

$$\mathcal{W}_V(E) = w_1 \frac{\tilde{E}^2}{\tilde{E}^2 + w_2^2}, \tag{2.19}$$

$$\mathcal{W}_D(E) = d_1 \frac{\tilde{E}^2 \, e^{-d_2\tilde{E}}}{\tilde{E}^2 + d_3^2}, \tag{2.20}$$

$$\mathcal{V}_{SO}(E) = v_{SO1} e^{-v_{SO2}\tilde{E}}, \tag{2.21}$$

where $\tilde{E} = E - E_F$ is the projectile energy relative to the Fermi energy E_F.

In the left panels of Figs. 2.2 and 2.3 we show as the solid black lines the best fit functions of the form Eqs. (2.13)-(2.21) to the microscopic calculations. We see that overall the phenomenological form can reproduce well the radial dependence of the microscopic optical potential. In the present study we have isolated the optical potential at low energy, where there is a defined surface imaginary peak, and fitted to the phenomenological form separately. At larger energies $E > 50$ MeV, we have also fitted to the phenomenological form separately. To show that no crucial features of the chiral potential are lost in this parameterization, we also display the accompanying coefficient of determination R^2 for the fits in Figs. 2.2, 2.3. Where $R^2 = 1 - \frac{SS_{res}}{SS_T}$, with $SS_{res} = \sum_i (y_i - f(x_i))^2$ and $SS_T = \sum_i (y_i - \bar{y})^2$. In the right panels of Figs. 2.2, 2.3, the ILDA results are obtained from

the parametrized form of the corresponding parts of the optical potentials.

For the global KD phenomenological optical potentials we note that the real and imaginary volume terms have identical Woods-Saxon shape functions. From the microscopic perspective there is little justification for this assumption. In fact, we find that the shape parameters of the real and imaginary central optical potentials have to be fitted separately in order to achieve a good fit to the microscopic results. In Table 2.1 we show the values of all shape parameters for the three energy windows over which we fit to the phenomenological form together with those of the phenomenological Koning-Delaroche optical potential, whose shape parameters are independent of energy. For these results we have chosen the values $t_C = 1.15\,\text{fm}$ and $t_{SO} = 1.0\,\text{fm}$ in the ILDA. We see that there is not a very large energy dependence in the shape parameters of the real volume part of the microscopic optical potential, but there is a significant difference among the real volume, imaginary volume, and real spin-orbit terms. This suggests that there is no microscopic justification for assumptions made in phenomenological studies that equate geometry parameters of different terms in the optical potential.

Finally, we note that the microscopic real spin-orbit optical potential calculated from the density matrix expansion has no energy dependence. The phenomenological energy dependence used in TALYS ($v_{SO2} = 0.004$) is constant across all nuclei, and in fact since v_{SO2} is small, the real spin-orbit term does not strongly depend on the energy. We have therefore incorporated this phenomenological energy dependence into our parametrization of the spin-orbit optical potential. As mentioned above, the imaginary spin-orbit part of the optical potential is neglected since its magnitude for the relevant energy range is ~ 0.1 MeV and has been shown to have a negligible effect on elastic scattering cross sections at relatively low energies [65].

2.2.5 Volume integrals of the real and imaginary parts of the optical potential

We end this section by comparing the volume integrals of the various components of the microscopic optical potential to those from phenomenology. It has been demonstrated [5] that physical scattering observables can remain unchanged even if the various parameters of an optical potential

Table 2.2: Volume integrals for the real central V_C, imaginary central W_C, and real spin-orbit V_{SO} parts of the proton-^{40}Ca optical potential. Results are shown for the microscopic chiral optical potential and for the phenomenological Koning-Delaroche (KD) optical potential. Reprinted from [77].

$E = 2.35$ MeV	Chiral (MeV fm^3)	KD (MeV fm^3)
V_C	524	480
W_C	64	80
V_{SO}	19	13
$E = 35$ MeV	Chiral (MeV fm^3)	KD (MeV fm^3)
V_C	413	374
W_C	120	113
V_{SO}	17	11
$E = 100$ MeV	Chiral (MeV fm^3)	KD (MeV fm^3)
V_C	236	220
W_C	163	109
V_{SO}	13	9

are allowed to vary, provided that the volume integrals, defined by

$$\frac{J}{A} = \frac{1}{A}\int U(r) d^3r, \tag{2.22}$$

remain roughly constant. In Table 2.2 we show the volume integrals for each term of the microscopic and phenomenological optical potentials for the proton-^{40}Ca system at the three energies $E = 2.35, 35, 100$ MeV. We see that the microscopic real volume and spin-orbit terms are both slightly larger than their phenomenological counterparts for all three energies considered. The central imaginary term features a volume part that grows with energy and a surface peak that diminishes with energy. The imaginary term of the chiral optical potential overestimates the volume component and underestimates the surface component. For $E = 35$ MeV these competing effects nearly cancel out and the chiral volume integral is close to the phenomenological volume integral. At $E = 2.35$ MeV, the volume integral for the chiral imaginary term is smaller than the KD model since its surface peak is at a smaller r value. For higher energies, the microscopic imaginary term

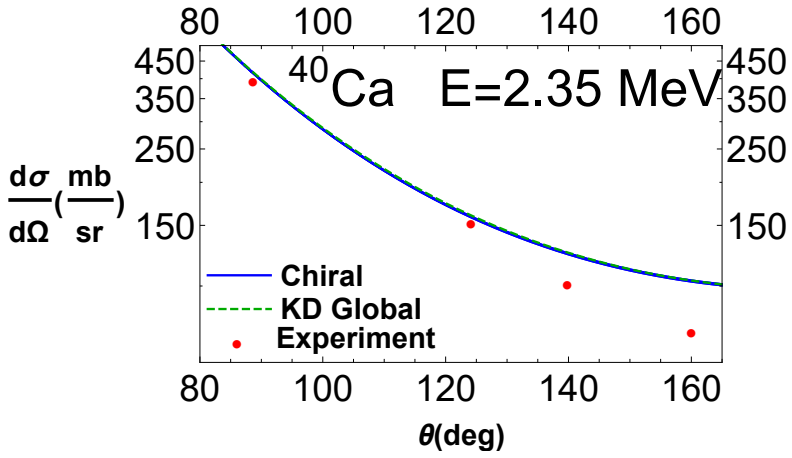

Figure 2.4: Differential elastic scattering cross sections for proton-^{40}Ca at projectile energy $E = 2.35$ MeV. The microscopic cross section is given by the blue band. The KD phenomenological cross section is given by the green dashed curve, and experimental data are represented by red circles. Reprinted from [77].

becomes larger than the phenomenological imaginary term.

2.3 Results

As a first test of the microscopic optical potentials constructed in the present work, we consider proton scattering on calcium isotopes. Both the differential elastic scattering cross sections and total reaction cross sections are calculated for selected calcium isotopes at energies for which there are available experimental data. In particular, we compute differential elastic scattering cross sections for ^{40,42,44,48}Ca targets at $E = 25, 35, 45$ MeV projectile energies. For ^{40}Ca, differential elastic scattering cross sections are also calculated at $E = 2.35, 55, 65, 80, 135, 160$ MeV. Experimental data are taken from Refs. [66, 67, 68, 69, 70]. The total reaction cross sections for proton scattering on ^{40,42,44,48}Ca are calculated and compared to experimental data [71, 72, 73, 74]. Ener-

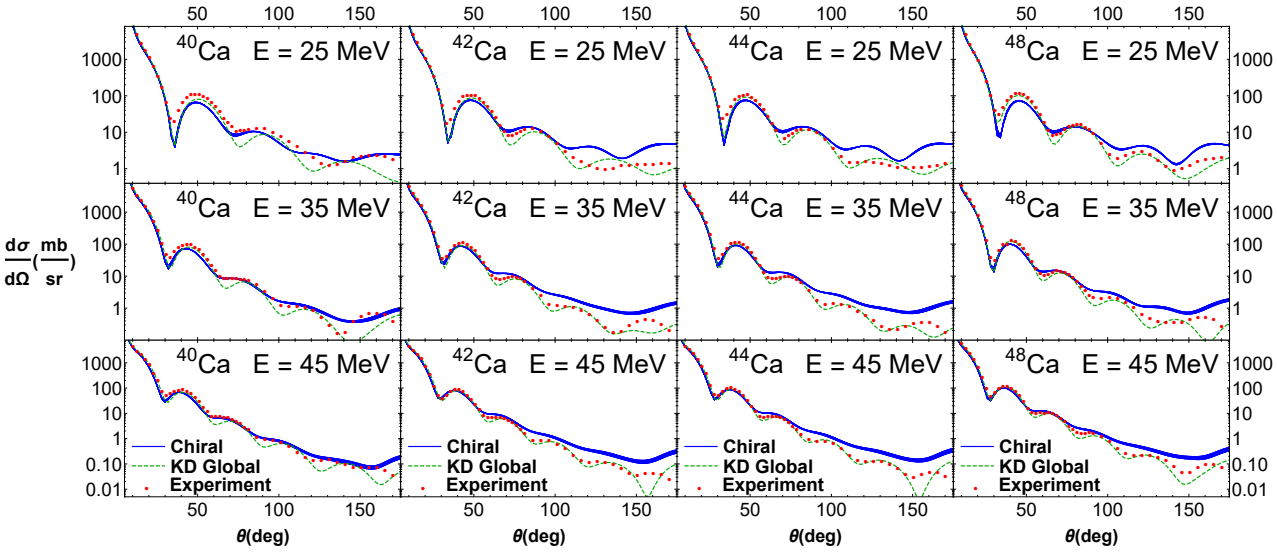

Figure 2.5: Differential elastic scattering cross sections for proton projectiles on calcium targets at the energies $E = 25, 35, 45$ MeV. The microscopic cross sections are shown as the blue band. The KD phenomenological cross sections are given by the green dashed curves and experimental data are represented by red circles. Reprinted from [77].

gies exceeding 200 MeV are not considered, since the chiral expansion is expected to breakdown around that energy scale.

The TALYS reaction code is used to calculate the cross sections in the different reaction channels. In all cases we employ the microscopic optical potential parametrized to the KD form implemented in the ILDA. In the present work, the only theoretical uncertainties considered are those for the ILDA length scales t_C and t_{SO}. We also benchmark against results from the KD global phenomenological optical potential [4].

2.3.1 Microscopic optical potential at low energy

Low-energy nuclear reactions are important for a wide range of astrophysical applications. One of the primary motivations for the construction of new global microscopic optical potentials is to reduce the uncertainty in calculated radiative neutron capture reaction rates on exotic, neutron-rich isotopes. These reactions play an important role in r-process nucleosynthesis [75, 76], especially in cold r-process environments such as neutron star mergers where freeze-out is achieved rapidly and neutron capture plays an enhanced role. Neutron-capture rates are included in most modern

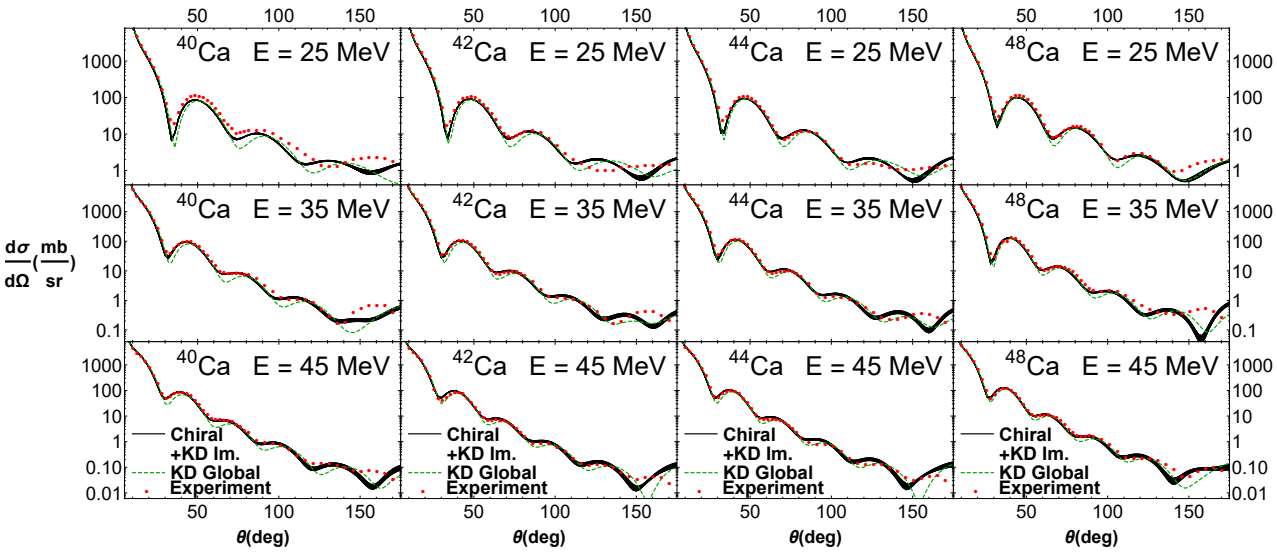

Figure 2.6: Differential elastic scattering cross sections for proton projectiles on calcium targets at the energies $E = 25, 35, 45$ MeV. In comparison to Fig. 2.5, the black bands show the cross sections that result from replacing the microscopic imaginary part in the chiral optical potential by the Koning-Delaroche phenomenological imaginary part. Reprinted from [77].

r-process reaction network codes, and the neutron-nucleus optical potential (together with level densities and γ transition strength functions) is one of the key ingredients for the theoretical calculations. Most relevant is the imaginary part of the optical potential at low energies [62].

In Fig. 2.4 we show the differential elastic scattering cross sections for proton projectiles on a ^{40}Ca target at $E = 2.35$ MeV. The red circles indicate experimental data [66, 67, 68, 69, 70], the green dashed curve is the result of the global phenomenological optical potential from Koning and Delaroche, while the blue band is the prediction from the microscopic optical potential constructed in the present work. Interestingly, there is very little difference between the phenomenological optical potential predictions and those from chiral effective field theory. Both calculations agree well with experimental data at scattering angles up to $\theta \simeq 120°$, but overpredict the cross section at large angles.

2.3.2 Microscopic optical potential at medium energy

In Fig. 2.5 we plot the differential elastic scattering cross sections for protons on ^{40,42,44,48}Ca targets at $E = 24, 35, 45$ MeV. For scattering angles in the range $0° < \theta < 80°$, the microscopic

optical potential yields cross sections that are consistent with experiment and often more accurate than predictions based on the phenomenological KD optical potential. However, at larger scattering angles the microscopic calculations of the cross sections exhibit a weaker interference pattern, which persists as the energy increases. Overall, the microscopic elastic scattering cross sections are larger than experiment at high scattering angles.

From Fig. 2.3, we suspect that the underlying cause of these discrepancies may be due to the imaginary part of the microscopic optical potential. At these intermediate projectile energies, the imaginary volume integral is close to phenomenology according to Table 2.2. However, the microscopic surface imaginary peak is too small, as can be seen in Fig. 2.3, which leads to larger elastic scattering cross sections. In contrast the imaginary volume part, probed at higher projectile energies, is much larger than phenomenology.

In order to investigate this conjecture, we substitute the phenomenological imaginary term into the microscopic optical potential. This replacement is meant to be a simple way of showing the possible improvements in the chiral optical potential and should not be interpreted as a substitute for proper microscopic modeling. In Fig. 2.6 we show the differential elastic scattering cross sections for protons on ^{40,42,44,48}Ca targets at $E = 24, 35, 45$ MeV with this phenomenological replacement. Indeed we find that the calculated cross sections are much improved at large angles across all isotopes. The enhanced surface imaginary part leads to stronger interferences and an overall decrease in the elastic scattering cross section. Hence, there is a strong motivation for future work aimed at improving the microscopic description of the imaginary part of the optical potential.

2.3.3 Microscopic optical potential at high energy

To test the chiral optical potential at higher energies, we calculate proton-^{40}Ca differential elastic scattering cross sections at $E = 55, 65, 80, 135, 160$ MeV. In Fig. 2.7 we plot the results from the chiral optical potential and the KD phenomenological optical potential together with experimental data from Refs. [66, 67, 68, 69, 70]. The cross sections from the chiral optical potential stay close to phenomenological and experimental results for $E = 55, 65$ MeV but begin to

deviate strongly for $E > 80$ MeV. The microscopic imaginary term becomes much more absorptive for $E > 80$ MeV, as the large volume contribution from the chiral optical potential becomes more relevant. The effect of this can be seen especially in the lower three plots of Fig. 2.7, where the cross sections exhibit large interference oscillations. Since there are more open inelastic channels at higher energy, a stronger imaginary part in general corresponds to a lower elastic scattering cross section.

In order to assess the quality of the microscopic imaginary part of the optical potential, we again substitute the KD phenomenological imaginary part into the chiral optical potential. The results for proton-^{40}Ca elastic scattering cross sections at $E = 55, 65, 80, 135, 160$ MeV are shown in Fig. 2.7. Again, we find that the replacement of the large microscopic imaginary optical potential by the KD phenomenological imaginary part leads to significant improvements in the elastic scattering cross sections across all energies. For $E = 135$ and 160 MeV, the purely phenomenological cross sections are still more accurate, but the microscopic optical potential with phenomenological imaginary part gives a high quality description of the data.

2.3.4 Total reaction cross section

In Figs. 2.8 and 2.9 we plot the total reaction cross sections, which is the sum of elastic and non-elastic cross sections $\sigma_{tot} = \sigma_{el} + \sigma_{non-el}$, for proton scattering on ^{40,42,44,48}Ca from our microscopic optical potential and the KD phenomenological optical potential. The chiral EFT results are shown as the blue band, while the KD predictions are shown as dashed green lines. Experimental data [71, 72, 73, 74] are shown with red circles. We see that for all energies the purely microscopic optical potential predicts a total reaction cross section that is too large, while the phenomenological potential gives an overall good description for most isotopes and energies. However, for proton-^{48}Ca, the KD phenomenological potential also gives a larger total reaction cross section compared to experiment. This suggests that there might be room for improvement in the phenomenological description of the global isovector optical potential probed in this neutron-rich nucleus.

We also show in Figs. 2.8 and 2.9 the results for the total reaction cross sections (black solid

bands) when the microscopic imaginary part is replaced by the KD phenomenological imaginary potential. For intermediate energies ($20\,\mathrm{MeV} < E < 50\,\mathrm{MeV}$), there is not a substantial improvement in the comparison to experimental data. However, beyond energies of $E = 50\,\mathrm{MeV}$ that are shown in Fig. 2.8, the replacement of the phenomenological imaginary part again leads to a significant improvement in the description of the total reaction cross section. Nevertheless, the modified microscopic optical potential still overestimates the total reaction cross section for all energies due to the real volume and real spin-orbit terms having slightly larger depths than their phenomenological counterparts.

2.4 Conclusions

We have calculated a microscopic optical potential from chiral two- and three-body forces for proton scattering on calcium isotopes. We started from a self-consistent second-order calculation of the proton and neutron self energies in isospin-asymmetric nuclear matter from which we derived the central real and imaginary parts of the optical potential in finite nuclei within the framework of the improved local density approximation. The real spin-orbit potential was constructed from the improved density matrix expansion using the same chiral two- and three-body forces.

We found that chiral nucleon-nucleus optical potentials describe low-energy ($E < 5\,\mathrm{MeV}$) scattering processes rather well, due in part to a well-defined surface peak in the imaginary part of the optical potential. At all energies, the real central term is consistent with phenomenological modeling, while the microscopic spin-orbit strength is larger by $\sim 20\%$. At moderate energies ($E > 35\,\mathrm{MeV}$), the imaginary part of the chiral optical potential develops a large volume term without a significant surface peak. This leads to discrepancies between our theoretical calculations and experimental data, especially at large scattering angles. At the highest energies ($E \simeq 100 - 160\,\mathrm{MeV}$) considered in the present work, the large imaginary term leads to over suppression of the elastic scattering cross section. We have shown that substituting the microscopic imaginary part with the KD phenomenological optical potential leads to excellent agreement with elastic scattering and total reaction cross sections for nearly all isotopes and projectile energies investigated.

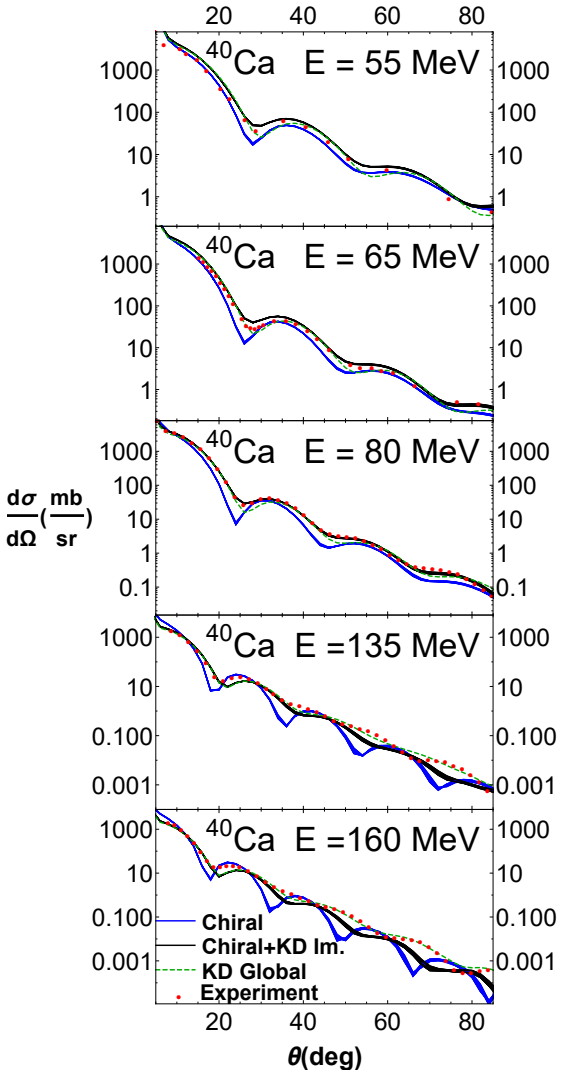

Figure 2.7: Differential elastic scattering cross sections for proton projectiles on a ^{40}Ca target at the energies $E = 55, 65, 80, 135, 160$ MeV. Full microscopic cross sections are shown as the blue bands, microscopic real optical potential plus phenomenological imaginary optical potential are shown by the black bands, the KD phenomenological cross sections are given by the green dashed curves, and experimental data are represented by red circles. Reprinted from [77].

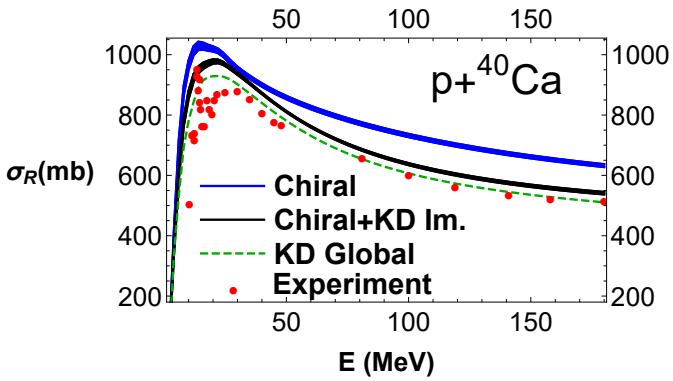

Figure 2.8: The proton-^{40}Ca total reaction cross section as a function of energy calculated from the microscopic optical potential (blue band), the phenomenological KD optical potential (dashed green curve), and the microscopic optical potential with the phenomenological KD imaginary part (black band). Experimental data are shown as red circles. Reprinted from [77].

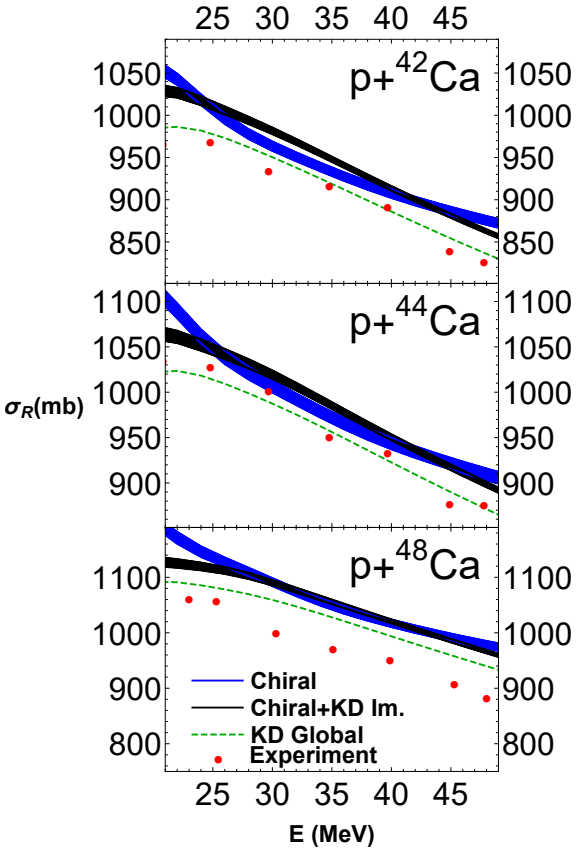

Figure 2.9: The proton-^{42,44,48}Ca total reaction cross sections from $20\,\mathrm{MeV} < E < 50\,\mathrm{MeV}$ calculated from the microscopic optical potential (blue bands), the phenomenological KD optical potential (dashed green curves), and the microscopic optical potential with the phenomenological KD imaginary part (black bands). Experimental data are shown as red circles. Reprinted from [77].

3. NEUTRON ELASTIC SCATTERING ON CALCIUM ISOTOPES FROM CHIRAL NUCLEAR OPTICAL POTENTIALS*

We formulate microscopic neutron-nucleus optical potentials from many-body perturbation theory based on chiral two- and three-body forces. The neutron self-energy is first calculated in homogeneous matter to second order in perturbation theory, which gives the central real and imaginary terms of the optical potential. The real spin-orbit term is calculated separately from the density matrix expansion using the same chiral interaction as in the self-energy. Finally, the full neutron-nucleus optical potential is derived within the improved local density approximation utilizing mean field models consistent with the chiral nuclear force employed. We compare the results of the microscopic calculations to phenomenological models and experimental data up to projectile energies of $E = 200$ MeV. Experimental elastic differential scattering cross sections and vector analyzing powers are generally well reproduced by the chiral optical potential, but we find that total cross sections are overestimated at high energies.

3.1 Introduction

Nucleon-nucleus optical potentials describe the interaction of a projectile nucleon with a target nucleus by reducing the complicated many-body interactions to an average single particle potential that is complex and energy-dependent. Global phenomenological optical potentials [3, 4] are able to describe scattering processes for a large range of nuclei and projectile energies. These global potentials are developed by optimizing their parameters to best reproduce experimental data. Phenomenological potentials yield remarkably good results when interpolating within these ranges, but may not reliably extrapolate to regions where there are no experimental data. Since microscopic optical potentials are built up from fundamental nuclear interactions without tuning to data, they may have greater predictive power in regions of the nuclear chart that are unexplored

*Reprinted with permission from "Neutron elastic scattering on calcium isotopes from chiral nuclear optical potentials" by T.R. Whitehead, Y. Lim, J.W. Holt, 2020. Phys.Rev.C, 101, 064613 , Copyright [2020] American Physical Society.

experimentally.

There has been much interest recently in the development of microscopic optical potentials [10, 12, 27, 28, 29, 22, 30, 31, 77] based on chiral effective field theory (EFT) [32, 33, 2], which implements realistic microphysics including multi-pion exchange processes and three-body interactions all within a framework that allows for the assessment of theoretical uncertainties. Optical potentials based on chiral forces are well suited to describe low-energy nuclear reactions but are expected to break down for energies approaching the cutoff scale of the theory. In practice, the presence of the cutoff constrains nucleon projectile energies to $E < 200\,\mathrm{MeV}$.

In the present study, we compute neutron-nucleus optical potentials along the lines of our previous work in [77] that focused exclusively on the description of proton elastic and total reaction cross sections. Since proton elastic scattering at forward angles approaches the well-known Rutherford cross section, the microscopic description of neutron scattering presents a novel challenge that has not yet been addressed in our work. Ultimately our goal is to develop a new microscopic global optical potential for nucleon-nucleus scattering across a large range of isotopes, including those off stability, up to projectile energies of 200 MeV in support of current and future experiments at radioactive ion beam facilities. Presently we consider differential elastic and total cross sections for n-^{40,48}Ca scattering at energies ranging from 3-200 MeV. Additionally, in the first direct test of our microscopic spin-orbit term, the vector analyzing power is calculated at selected energies for n-^{40}Ca scattering. The choice of isotopes and energies is limited by the availability of experimental data for comparison. We also compare the microscopically calculated scattering observables to the results of the global phenomenological optical potential of Koning and Delaroche [4]. Scattering observables are calculated using the TALYS [34] reaction code. While the vector analyzing power is not output directly by TALYS, it can be extracted from the output files of ECIS-06, a program that runs in the background of TALYS.

We take as the foundation of our calculations a high-precision 2N + 3N chiral nuclear interaction with a momentum-space cutoff of $\Lambda = 450\,\mathrm{MeV}$. The low-energy constants of the potential are fitted to empirical data. For two-body interactions, the empirical inputs include nucleon-nucleon

scattering phase shifts and deuteron properties. Three-body contact terms are fit to the triton binding energy and lifetime [38]. The nucleon-nucleon interaction is calculated to next-to-next-to-next-to-leading order (N3LO), while the three-nucleon force is only calculated at N2LO. Work towards the inclusion of three-nucleon N3LO interactions is in progress [35, 36, 37, 78, 79, 80] and we plan to implement them in future works. The chiral nuclear potential employed in the present work reproduces known values for nuclear matter properties, such as saturation energy and density [38], thermodynamics [39, 40], and Fermi liquid parameters [41] when calculated to at least second order in many-body perturbation theory.

In quantum many-body theory, the energy- and momentum-dependent single-particle self-energy is equivalent to the optical potential for scattering states [42]. We first compute the nucleon self-energy in homogeneous nuclear matter of arbitrary density and proton fraction to second order in many-body perturbation theory including chiral two- and three-body forces. We next compute nuclear density distributions for ^{40,48}Ca from mean field theory employing the Sk$_\chi$450 Skyrme effective interaction [43] constrained by chiral EFT. In the local density approximation (LDA) the nucleon-nucleus optical potential is computed [44] by folding the nuclear matter optical potential with a nuclear density distribution. The LDA is known to underestimate the surface diffuseness of the optical potential in finite nuclei and requires a modification known as the improved local density approximation (ILDA) [44, 9] that accounts for the nonzero range of the nuclear interaction.

The main advantage of the nuclear matter approach to deriving optical potentials is its adaptability to many nuclei. Once the nuclear matter optical potential is calculated, only the nuclear density distribution is needed to produce a nucleon-nucleus optical potential, making the nuclear matter approach well suited to constructing a *microscopic global* optical potential. However, the drawback is that some physical processes present in scattering with finite nuclei are not captured by nuclear matter calculations. Among these are collective surface modes, shell structure effects, and the fact that the spin-orbit term is not present in homogeneous nuclear matter. We therefore include a microscopic spin-orbit term from the improved density matrix expansion [46, 47, 48] based on chiral interactions. Compared to the standard density matrix expansion of Negele and Vautherin

[49], the improved density matrix expansion provides a better description of the spin-dependent part of the energy density functional.

In Section 3.2 we calculate the microscopic optical potential in nuclear matter with nucleon interactions from chiral EFT. We then calculate nuclear density distributions from mean field theory with a Skyrme interaction fit to the chiral EFT potential used in the self-energy. The ILDA is then employed to construct nucleon-nucleus optical potentials for ^{40,48}Ca. Finally, the microscopic optical potentials are parameterized to the Koning-Delaroche (KD) phenomenological form in order to implement them in the reaction code TALYS. In Section 3.3 we compute neutron-nucleus elastic differential scattering cross sections up to a projectile energy $E = 185\,\text{MeV}$ and total cross sections up to $E = 200\,\text{MeV}$. We also calculate the vector analyzing power for elastic n-^{40}Ca scattering as a test of our spin-orbit term. These results are compared to experiment and predictions of the KD phenomenological model.

3.2 Optical potential from chiral effective field theory

3.2.1 Real and imaginary central terms

The nucleon self-energy is calculated as a function of density and momentum in homogeneous nuclear matter of arbitrary isospin asymmetry using a nuclear potential derived from chiral EFT. The expressions for the first- and second-order perturbative contributions to the nucleon self-energy are given by Eq. (2.1) and Eqs. (2.2) , (2.3) and shown diagrammatically in Fig. 1.4. In the above expressions $n_i = \theta(k_f - k_i)$ is the occupation probability for a filled state with momentum $k_i < k_f$ below the Fermi momentum, and particle state occupation probabilities are given by $\bar{n}_i = \theta(k_i - k_f)$, with the summation going over intermediate-state momenta for particles $\vec{p}_i$ and holes $\vec{h}_i$, their spins s_i, and isospins t_i. The overbar on the potential indicates that it is properly antisymmetrized. The in-medium effective nuclear potential V_{2N}^{eff} is the two-body interaction which consists of the bare nucleon-nucleon (NN) potential V_{NN} plus an effective, density-dependent (and isospin-asymmetry-dependent) NN interaction V_{NN}^{med} derived from the N2LO chiral three-nucleon force by averaging one particle over the filled Fermi sea of noninteracting nucleons [50,

51, 52, 80]. In the first-order Hartree-Fock contribution, Eq. (2.1), the effective interaction is given by $V_{2N}^{\rm eff} = V_{NN} + \frac{1}{2}V_{NN}^{\rm med}$, while for the higher-order contributions, Eqs. (2.2) and (2.3), the effective interaction is given by $V_{2N}^{\rm eff} = V_{NN} + V_{NN}^{\rm med}$. The Hartree-Fock contribution is nonlocal, energy independent, and real, while the second-order contributions are in general nonlocal, energy dependent, and complex. The single-particle energies in the denominators of Eqs. (2.2) and (2.3) are computed self-consistently according to $\epsilon(q) = \frac{q^2}{2M} + {\rm Re}\Sigma(q, \epsilon(q))$ where M is the free-space nucleon mass.

To derive optical potentials of neutron- or proton-rich nuclei, it is necessary to calculate the self-energy for arbitrary isospin-asymmetry, $\delta_{np} = (\rho_n - \rho_p)/(\rho_n + \rho_p)$. The resulting optical potentials for nucleons propagating in homogeneous matter with proton and neutron Fermi momenta k_f^p and k_f^n are given by

$$\begin{aligned} U_p(E; k_f^p, k_f^n) &= V_p(E; k_f^p, k_f^n) + iW_p(E; k_f^p, k_f^n), \\ U_n(E; k_f^p, k_f^n) &= V_n(E; k_f^p, k_f^n) + iW_n(E; k_f^p, k_f^n) \end{aligned} \tag{3.1}$$

with

$$V_i(E; k_f^p, k_f^n) = {\rm Re}\Sigma_i(q, E(q); k_f^p, k_f^n), \tag{3.2}$$

$$W_i(E; k_f^p, k_f^n) = \frac{M_i^{k*}}{M}{\rm Im}\Sigma_i(q, E(q); k_f^p, k_f^n), \tag{3.3}$$

where the subscript i denotes a propagating proton or neutron. To relate the microscopically derived imaginary part of the nucleon self-energy to the imaginary term of the optical potential used in phenomenology, the non-locality must be accounted for [53, 54]. This is achieved by multiplying the imaginary term of the self-energy by the effective k-mass M_i^{k*} defined by

$$\frac{M_i^{k*}}{M} = \left(1 + \frac{M}{k}\frac{\partial}{\partial k}V_i(k, E(k)\right)^{-1}. \tag{3.4}$$

3.2.2 Spin-orbit optical potential

The effective one-body spin-orbit interaction vanishes in homogeneous nuclear matter due to translational invariance and thus cannot be computed within the framework described above. Alternatively, we employ an improved density matrix expansion [47, 55, 48] to construct the one-body spin-orbit interaction from chiral two- and three-body forces. By utilizing the improved density matrix expansion that takes advantage of phase space averaging, a more accurate spin-dependent energy density functional can be derived compared to the standard density matrix expansion of Negele-Vautherin [49].

The density matrix is defined by

$$\rho(\vec{r}_1\sigma_1\tau_1;\vec{r}_2\sigma_2\tau_2) = \sum_\alpha \Psi^*_\alpha(\vec{r}_2\sigma_2\tau_2)\Psi_\alpha(\vec{r}_1\sigma_1\tau_1), \tag{3.5}$$

where Ψ_α are the energy eigenfunctions of the occupied orbitals in the non-relativistic many-body system. The energy density functional for a $N = Z$ even-even nucleus in the Hartree-Fock approximation expanded to second order in spatial gradients is given by

$$\begin{aligned} \mathcal{E}[\rho,\tau,\vec{J}] &= \rho\,\bar{E}(\rho) + \left[\tau - \frac{3}{5}\rho k_f^2\right]\left[\frac{1}{2M_N} + F_\tau(\rho)\right] \\ &\quad + (\vec{\nabla}\rho)^2\,F_\nabla(\rho) + \vec{\nabla}\rho\cdot\vec{J}\,F_{SO}(\rho) + \vec{J}^{\,2}\,F_J(\rho)\,, \end{aligned} \tag{3.6}$$

where $\rho(\vec{r}) = 2k_f^3(\vec{r})/3\pi^2 = \sum_\alpha \Psi^\dagger_\alpha(\vec{r})\Psi_\alpha(\vec{r})$ is the local density and $k_f(\vec{r})$ is the local Fermi momentum. The kinetic energy density is given by $\tau(\vec{r}) = \sum_\alpha \vec{\nabla}\Psi^\dagger_\alpha(\vec{r})\cdot\vec{\nabla}\Psi_\alpha(\vec{r})$ and the spin-orbit density is given by $\vec{J}(\vec{r}) = i\sum_\alpha \vec{\Psi}^\dagger_\alpha(\vec{r})\vec{\sigma}\times\vec{\nabla}\Psi_\alpha(\vec{r})$. This calculation yields the spin-orbit term $F_{SO}(\rho)$ of the optical potential for $N = Z$ nuclei to first order in many-body perturbation theory. The isovector part [57] of the spin-orbit interaction for ^{48}Ca is not included in this study since it is small compared to the isoscalar part [48]. In the context of nucleon-nucleus scattering, the spin-orbit term of the optical potential determines the polarization of scattered nucleons. One such polarization observable is the vector analyzing power, which we will calculate microscopically and

compare to experimental data and phenomenological results.

3.2.3 Improved local density approximation

The improved local density approximation (ILDA) is used to construct the nucleon-nucleus optical potential from the nucleon self-energy in nuclear matter. The nucleon-nucleus optical potential is derived by folding the density-dependent self-energy with the radial density distribution of a target nucleus and then smeared by integrating over the radial dimension with a Gaussian factor to account for the nonzero range of the nuclear force. We calculate the nuclear density distributions within mean field theory from the Skχ450 Skyrme interaction [43]. The Skχ450 interaction is fit to properties of finite nuclei in addition to theoretical calculations of the asymmetric nuclear matter equation of state from the N3LO chiral potential with cutoff scale $\Lambda = 450\,\mathrm{MeV}$ used to calculate the self-energy. In Fig. 3.1 we show the calculated nucleon density distributions for ^{40,48}Ca. In order to benchmark these density distributions with experiment we also show the charge density distribution for ^{48}Ca calculated from mean field theory compared to an empirical charge density [81] obtained from electron scattering data. The theoretical charge density for ^{48}Ca slightly underestimates experimental results from $1\,\mathrm{fm} < r < 3\,\mathrm{fm}$ and slightly overestimates in the surface region. We have verified as well that the charge density of ^{40}Ca from mean field theory has a qualitatively similar comparison to experiment.

In the local density approximation, the nucleon-nucleus optical potential is evaluated as

$$\begin{aligned} V(E;r) + iW(E;r) = V(E;k_f^p(r),k_f^n(r)) \\ +iW(E;k_f^p(r),k_f^n(r)), \end{aligned} \tag{3.7}$$

where $k_f^p(r)$ and $k_f^n(r)$ are the local proton and neutron Fermi momenta. This approximation does not account for the nonzero range of nuclear forces, and is known to underestimate the surface diffuseness of nucleon-nucleus optical potentials [58, 44]. For this reason, the standard LDA provides an inadequate description of nuclear scattering processes. To account for the range of the nuclear force and obtain a more realistic nuclear optical potential, the improved local density

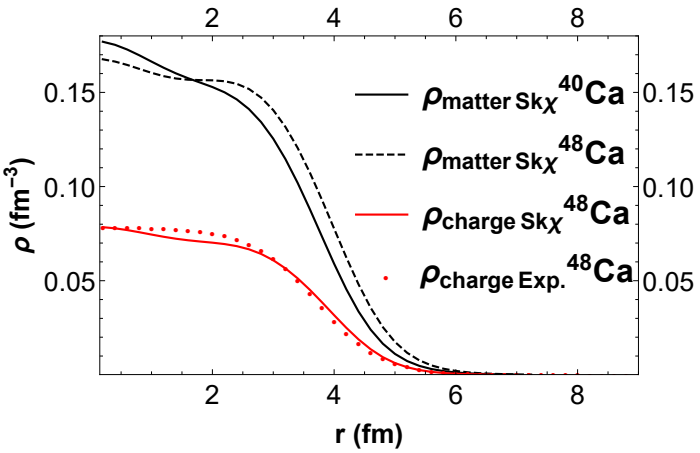

Figure 3.1: The matter density distributions for ^{40,48}Ca, represented by a black curve and a dashed black curve respectively, are calculated in mean field theory from the Skyrme Skχ450 effective interaction constrained by chiral effective field theory. The empirical charge density distribution for ^{48}Ca along with the mean field calculation are represented by red dots and a red curve respectively. Reprinted from [103].

approximation is employed. The ILDA applies a Gaussian smearing

$$V(E;r)_{ILDA} = \frac{1}{(t\sqrt{\pi})^3}\int V(E;r')e^{\frac{-|\vec{r}-\vec{r}'|^2}{t^2}}d^3r' \tag{3.8}$$

that is characterized by a variable length scale t associated with the range of the nuclear force. In Ref. [9] it is found that for the central part of the optical potential $t_C = 1.3\,\mathrm{fm}$ gives the best fit to experimental neutron total cross sections for $10\,\mathrm{MeV} < E < 200\,\mathrm{MeV}$ and targets ranging from ^{40}Ca to ^{208}Pb. Presently we vary the range parameter over $1.25\,\mathrm{fm} < t_C < 1.35\,\mathrm{fm}$ to estimate the theoretical uncertainty associated with the choice of length scale t_C. As in [77], we find the spin-orbit range parameter to be $t_{SO} = 1.07$ fm and vary it across the range $1.0\,\mathrm{fm} < t_{SO} < 1.1\,\mathrm{fm}$ to estimate the uncertainty.

In Fig. 3.2 we show the real central, imaginary central, and real spin-orbit terms of the ILDA chiral optical potential compared to the analogous terms of the KD phenomenological optical potential for n-^{40}Ca at projectile energies $E = 3.2, 30, 85$ MeV. The width of the blue band representing the chiral terms shows the relatively small effect of varying the distance parameter in the ILDA.

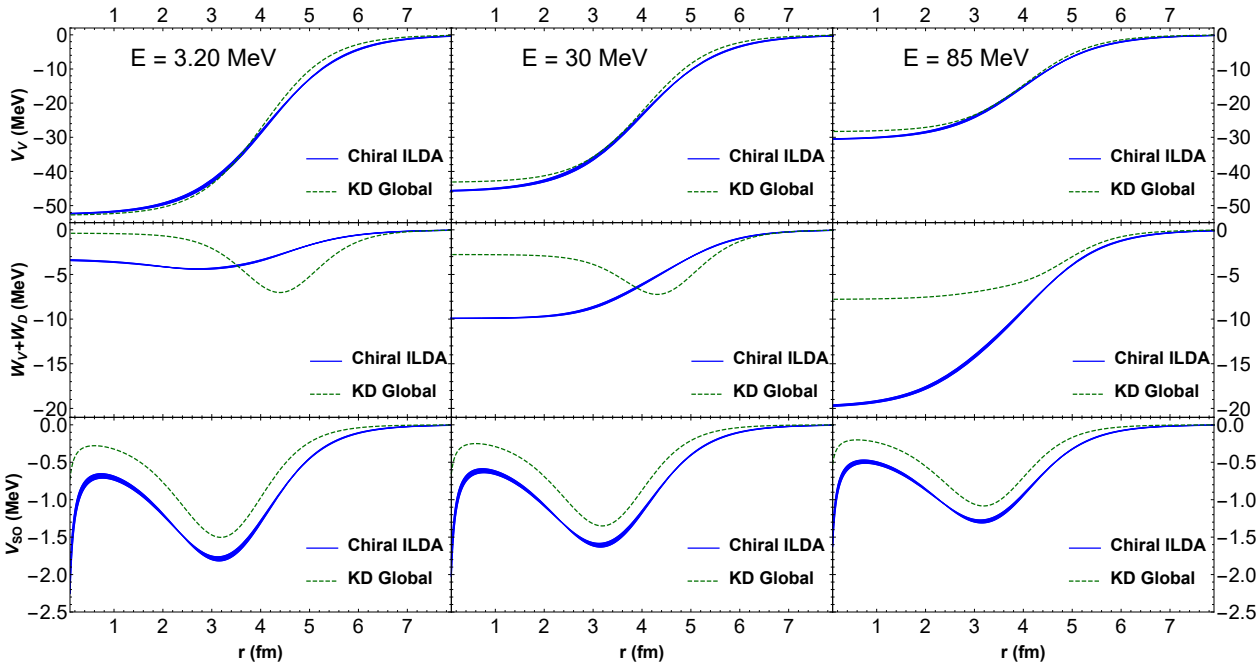

Figure 3.2: The real, imaginary, and spin-orbit terms of the n-^{40}Ca optical potential at projectile energies $E = 3.20, 30, 85$ MeV. The blue bands represent the microscopic chiral optical potential after applying the improved local density approximation with a varied length scale. The green dashed lines represent the analogous terms of the Koning-Delaroche global optical potential. Reprinted from [103].

In the left column of plots, the optical potential terms are shown at $E = 3.2$ MeV. The microscopic real volume term has a very similar depth and a slightly larger diffuseness compared to the KD term. At this low energy, the microscopic imaginary term has a surface peak and a nonzero central depth, whereas the KD imaginary term has virtually no central depth and a relatively large surface peak. The microscopic spin-orbit term has a very similar radial profile compared to KD, but with a larger depth across all energies.

At $E = 30$ MeV the middle column of plots in Fig. 3.2 shows a microscopic real volume term that has a slightly larger central depth and similar diffuseness compared to phenomenology. The microscopic imaginary term has a large central depth with almost no surface peak, while its phenomenological counterpart has a small central depth and moderate surface peak. This feature has been observed in other microscopic optical potentials calculated from nuclear matter [6, 60,

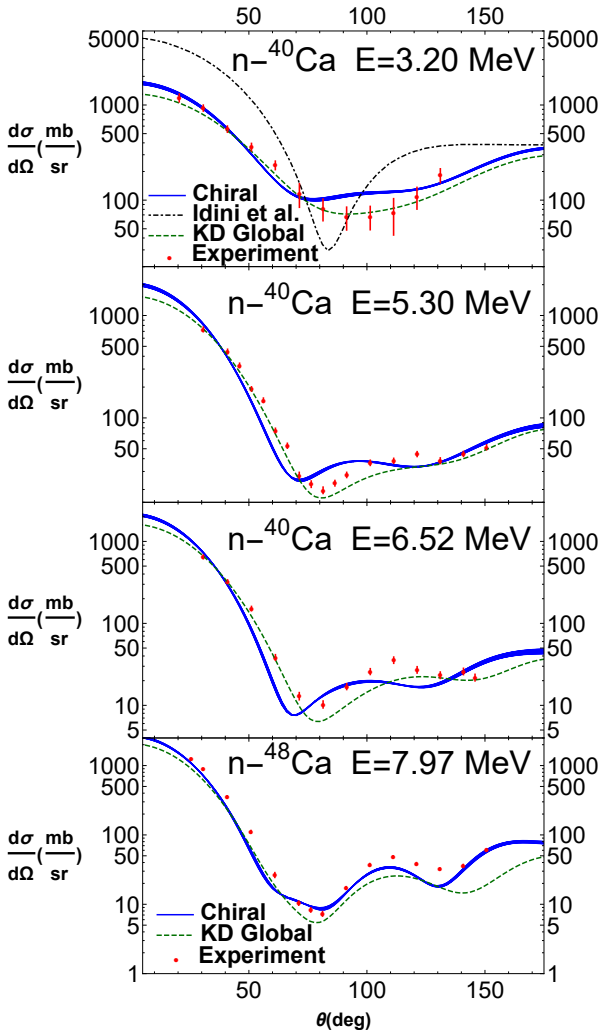

Figure 3.3: Differential elastic scattering cross sections for n-^{40}Ca at projectile energies $E = 3.2, 5.3, 6.52$ MeV and n-^{48}Ca at $E = 7.97$ MeV. The cross sections calculated from the chiral optical potential are given by the blue bands. The dot dashed black curve represents ab initio calculations found in Ref. [1]. The cross sections calculated from the Koning-Delaroche phenomenological optical potential are given by the green dashed curves, and experimental data are represented by red circles with error bars. Reprinted from [103].

61, 8]. To mitigate this discrepancy, some semi-microscopic optical potentials apply an energy-dependent scaling factor to the imaginary term [9, 62], but in the present work we employ no such factors. As the energy increases to $E = 85$ MeV, the real volume term becomes more shallow for both the microscopic and phenomenological potentials while qualitatively remaining the same relative to each other. At such high energy, the imaginary surface peak is no longer present in

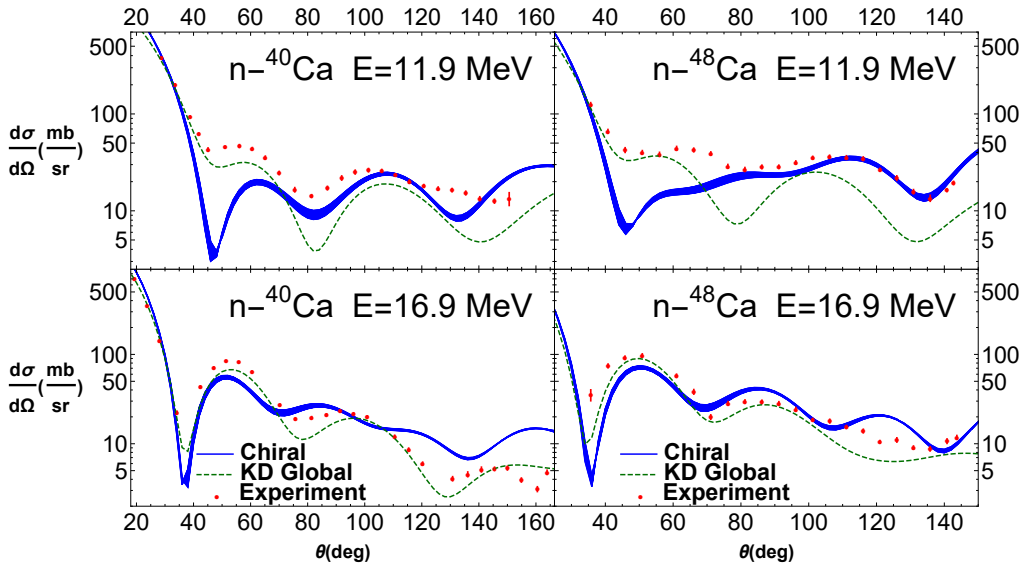

Figure 3.4: Differential elastic scattering cross sections for n-^{40,48}Ca at projectile energies $E = 11.9, 16.9$ MeV. The cross sections calculated from the chiral optical potential are given by the blue bands. The cross section calculated from the Koning-Delaroche phenomenological optical potential is given by the green dashed curve, and experimental data are represented by red circles with error bars. Reprinted from [103].

either the microscopic or phenomenological potentials. However, at this energy the central depth of the microscopic imaginary term is very large compared to phenomenology. This results in a chiral optical potential that is overly absorptive at high energy.

3.3 Results

In a continuation of Ref. [77], we calculate cross sections and vector analyzing powers of neutrons scattering on calcium isotopes from a microscopic optical potential based on chiral forces and compare to experiment and phenomenology. Both the differential elastic scattering cross sections and total cross sections are calculated for n-^{40,48}Ca at energies where experimental data are available. Specifically, we compute differential elastic scattering cross sections for n+^{40}Ca at projectile energies E = 3.2, 5.3, 6.52, 11.9, 16.9, 21.7, 25.5, 30, 40, 65, 85, 107.5, 155, 185 MeV. In order to test the spin-orbit term, vector analyzing powers are also calculated at $E = 11.9, 16.9$ MeV for n-^{40}Ca. Differential elastic scattering cross sections are calculated for n-^{48}Ca at $E = 7.97, 11.9, 16.9$ MeV. The total cross sections for n-^{40,48}Ca scattering are also

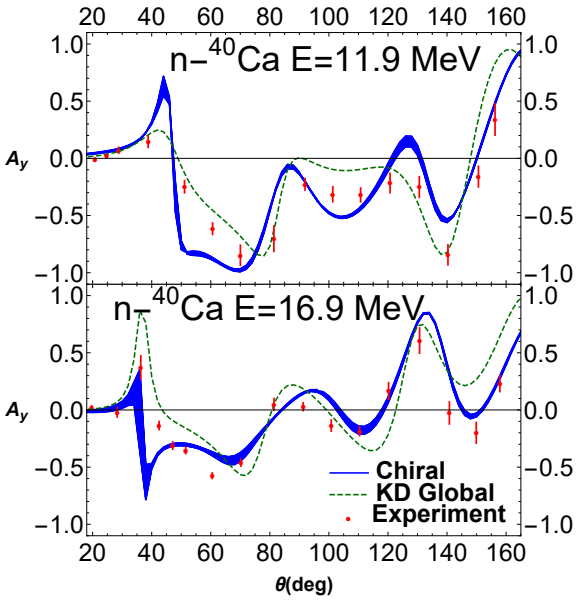

Figure 3.5: The vector analyzing powers for elastic n-^{40}Ca scattering at projectile energies $E = 11.9, 16.9$ MeV. The vector analyzing powers calculated from the chiral optical potential are given by the blue bands. The vector analyzing powers calculated from the Koning-Delaroche phenomenological optical potential are given by the green dashed curves, and experimental data are represented by red circles with error bars. Reprinted from [103].

calculated. Energies greater than 200 MeV are not considered since the chiral expansion is expected to break down near that energy scale [80]. Experimental data are taken from Refs. [82, 83, 84, 85, 86, 87, 88, 89, 90, 91, 92].

The TALYS reaction code is used to calculate all scattering observables. In all cases we employ the microscopic optical potential calculated using the ILDA and parameterized to the Koning-Delaroche phenomenological form at a specific energy. Presently the only theoretical uncertainties considered are the variations in the ILDA length scales t_C and t_{SO}. We also include results from the KD global phenomenological optical potential [4].

3.3.1 Microscopic optical potential at low energy

Low-energy nuclear reactions are important for describing a wide range of astrophysical processes. These reactions play an essential role in cold r-process environments [75, 93] such as neutron star mergers where freeze-out is achieved rapidly and neutron capture plays an enhanced

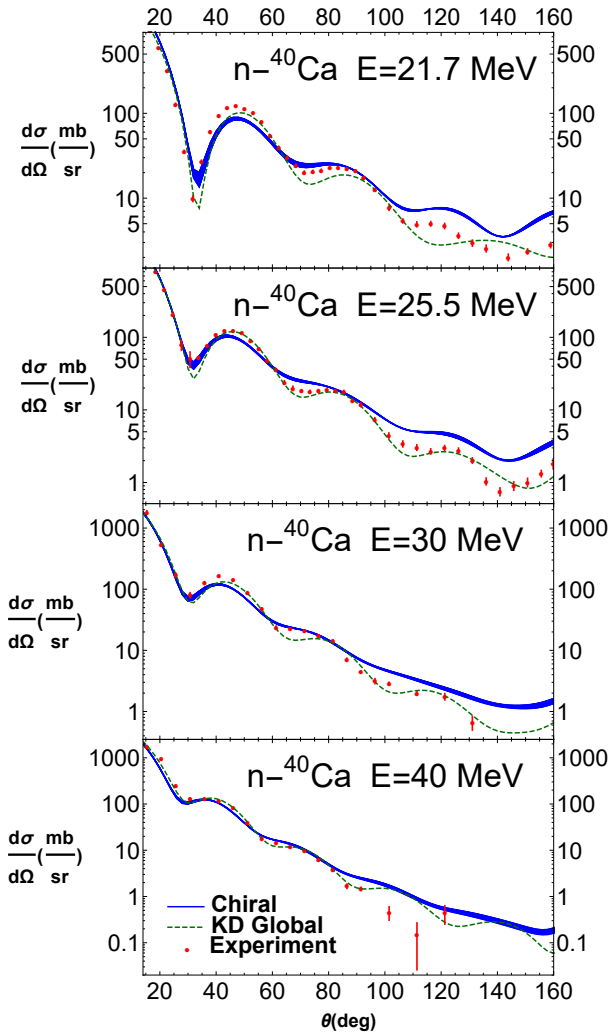

Figure 3.6: Differential elastic scattering cross sections for n-^{40}Ca at projectile energies $E = 21.7, 25.5, 30, 40$ MeV. The cross sections calculated from the chiral optical potential are given by the blue bands. The cross sections calculated from the Koning-Delaroche phenomenological optical potential are given by the green dashed curves, and experimental data are represented by red circles with error bars. Reprinted from [103].

role. Neutron capture rates on exotic, neutron-rich isotopes have large theoretical uncertainties [75]. These neutron-capture rates are included as inputs for most modern r-process reaction network codes. The neutron-nucleus optical potential, and especially the imaginary part of the optical potential at low energies [62], is a key ingredient in calculating neutron capture rates. One of the primary motivations for the construction of a new global microscopic optical potential is to better understand (and potentially reduce) these theoretical uncertainties.

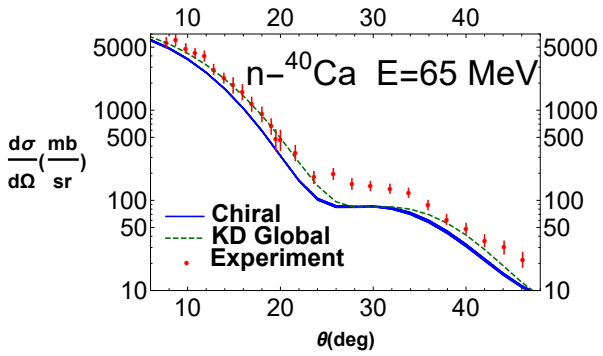

Figure 3.7: Differential elastic scattering cross sections for n-^{40}Ca at projectile energies $E = 65\,\text{MeV}$. The cross section calculated from the chiral optical potential is given by the blue band. The cross section calculated from the Koning-Delaroche phenomenological optical potential is given by the green dashed curve, and experimental data are represented by red circles with error bars. Reprinted from [103].

In Fig. 3.3 we show microscopic and phenomenological elastic scattering cross sections for neutron projectiles on a ^{40}Ca target at energies of $E = 3.2, 5.3, 6.52\,\text{MeV}$ as well as ^{48}Ca at $E = 7.97\,\text{MeV}$ and compare to experimental data [82, 87, 91]. Interestingly, there is very little difference between the chiral optical potential predictions and those of phenomenology. We find that the Koning-Delaroche global optical potential is in very good agreement with experimental data in this energy regime when the direct and compound contributions to the elastic scattering cross section are accounted for (cf. Ref. [28]). The compound contribution to the elastic scattering cross section is experimentally indistinguishable to the shape elastic contribution and must be included when comparing to experimental data. In the top plot of Fig. 3.3, we provide a comparison to the results found in Ref. [1] for elastic n-^{40}Ca scattering at $E = 3.2\,\text{MeV}$. The results by Idini et al. are obtained through an ab initio calculation of the optical potential using a self consistent Green function approach. We see that the nuclear matter approach in the improved local density approximation gives better agreement with data than the fully ab initio approach of Idini et al., which might be due to different theoretical nuclear density distributions or the density of states in the two approaches.

3.3.2 Microscopic optical potential at medium-low energy

In Fig. 3.4 we plot microscopic and phenomenological differential elastic scattering cross sections for neutrons on ^{40,48}Ca targets at $E = 11.9, 16.9\,\text{MeV}$ and compare to experimental data [83, 90, 89]. At the neutron projectile energy of $11.9\,\text{MeV}$, we find a significant discrepancy between the microscopic results and experimental data at certain scattering angles. In particular, for $E = 11.9\,\text{MeV}$ the n-^{40,48}Ca cross sections from the chiral optical potential have a sharp dip around $\theta = 45^\circ$ which is not present in the experimental data. For larger scattering angles, the chiral optical potential results have better agreement with experiment than the KD potential, whose predictions are uncharacteristically departed from experimental data. At $E = 16.9\,\text{MeV}$ the phenomenological and microscopic optical potentials both predict a dip just below $\theta = 40^\circ$ that is partly confirmed by experiment. At larger scattering angles, results from the chiral optical potential tend to overestimate the elastic scattering cross sections, while phenomenological optical potentials moderately underestimate them. The large disagreement between microscopic calculations and experimental results in this narrow energy range may be due to resonances and surface effects that are not accounted for in the nuclear matter approach. One such resonance present in the relevant energy range is the giant dipole resonance (GDR). The cross section for ^{40}Ca(n,γ)^{41}Ca is shown in Ref. [94] to be enhanced around $E = 12-20\,\text{MeV}$ due to the GDR. This resonance could be in part responsible for the large discrepancies between experimental data and our microscopic nuclear matter calculations.

We also plot the vector analyzing power for ^{40}Ca at $E = 11.9, 16.9\,\text{MeV}$ in Fig. 3.5. The vector analyzing power is a spin observable defined by

$$A_y(\theta) = \frac{1}{p_y}\frac{\sigma(\theta) - \sigma_0(\theta)}{\sigma_0(\theta)}, \tag{3.9}$$

where σ and σ_0 correspond to the scattering cross sections for a polarized and unpolarized beam respectively and p_y is the beam polarization in the direction normal to the scattering plane. This quantity is largely determined by the spin-orbit term of the optical potential. In this first direct

test of our chiral spin-orbit potential we find that overall it reproduces experimental data well. In particular, the angles at which the polarized cross section σ is equal to the unpolarized cross section σ_0 are reproduced very well.

3.3.3 Microscopic optical potential at medium-high energy

In Fig. 3.6 we plot microscopic and phenomenological differential elastic scattering cross sections for neutrons on ^{40}Ca targets at $E = 21.7, 25.5, 30, 40$ MeV and compare to experimental data [85, 86]. For relatively low scattering angles in the range of $0^\circ < \theta < 80^\circ$, the microscopic optical potential produces cross sections that are consistent with experiment and the phenomenological KD optical potential. For larger scattering angles the microscopic calculations of the cross sections overestimate experimental data and exhibit a weaker interference pattern that persists as the energy increases.

From Fig. 3.2, we expect the cause of these discrepancies is the imaginary part of the microscopic optical potential. The microscopic surface imaginary peak is very small in this energy range, as can be seen in Fig. 3.2. This leads to larger elastic scattering cross sections. In contrast the imaginary volume part is much larger than phenomenology at higher projectile energies. We have verified that replacing only the microscopic imaginary part with the Koning-Delaroche phenomenological imaginary part leads to significantly improved angular distributions for $\theta > 80^\circ$.

3.3.4 Microscopic optical potential at high energy

In Figs. 3.7, 3.8 we plot microscopic and phenomenological differential elastic scattering cross sections for neutrons on ^{40}Ca targets at $E = 65, 85, 107.5, 155, 185$ MeV and compare to experimental data [84, 88]. In Fig. 3.7, we see that the cross section from chiral effective field theory exhibits the same angular dependence as the experimental data, but microscopic many-body theory systematically underestimates the cross section across all scattering angles. In contrast, the KD phenomenological optical potential reproduces the experimental cross section up to $\theta = 25^\circ$ well. For larger scattering angles, however, the phenomenological cross section is smaller than experiment but very similar to the cross section from chiral effective field theory.

In Fig. 3.8 we compare experimental, phenomenological, and microscopic differential elastic scattering cross sections for n-^{40}Ca at $85\,\mathrm{MeV} < E < 185\,\mathrm{MeV}$. For these projectile energies, the experimental data span only a small range of scattering angles $\theta \leq 25^{\circ}$. The data also have large uncertainties which are as large as a factor of $2-5$ in the cross section. The results from chiral effective field theory are consistent with data up to experimental error bars in most cases, but the tendency is again for the microscopic optical potential to underestimate the cross sections. In all cases the KD results are within or very close to experimental data.

3.3.5 Total cross section

The total cross section is written as the sum of the elastic scattering and reaction cross section:

$$\sigma_T = \sigma_{\mathrm{el}} + \sigma_{\mathrm{re}}. \tag{3.10}$$

The reaction cross section in particular is expected to be very sensitive to the strength of the imaginary part of the optical potential. Consequently, we expect chiral optical potentials, with their large imaginary volume parts, to produce a large reaction cross section and hence a large total cross section at high energies. At low and moderate energies, the picture is more complicated as demonstrated in Ref. [77]. At low energies the microscopic surface imaginary part is small and the imaginary volume part is large compared to phenomenological optical potentials. Depending on the energy, the volume integral of the microscopic imaginary part is therefore either larger or smaller than phenomenology and the reaction cross section behaves analogously.

In Fig. 3.9 we show the total cross sections for neutron scattering on ^{40,48}Ca from the chiral optical potential and the KD phenomenological optical potential. In both plots of Fig. 3.9 the microscopic optical potential overestimates the total cross section for low energy then underestimates the cross section for medium energy. Past $E = 100\,\mathrm{MeV}$ the total cross section from chiral nuclear optical potentials is systematically too large. As mentioned above, this can be traced to the overly absorptive imaginary term. Overall, the phenomenological optical potential of Koning and Delaroche gives a good description for both isotopes at most energies. The only exception is

the n-^{40}Ca total cross section for projectile energies in the range $10\,\mathrm{MeV} < E < 50\,\mathrm{MeV}$, where the KD total cross sections are small compared to experiment. The experimental data in Ref. [92] were not included in the parameterization of the KD potential since the experiment was performed more recently. Additionally, for the previously mentioned energy range, these experimental data are in slight disagreement with previous experimental results [95] that the KD potential is fit to. We choose to plot only the more recent data set since total cross section measurements of both ^{40,48}Ca are made in the same work. In Fig. 3.9 the solid black curve is obtained by substituting the KD imaginary part into the chiral microscopic optical potential. We see that indeed there is a significant improvement in the description of the total cross section, which motivates the need to improve the imaginary part of the microscopic optical potential.

3.4 Conclusions

This work represents a continuation of an effort to construct a microscopic global optical potential based on nucleon interactions from chiral effective field theory. By calculating the nucleon optical potential in nuclear matter for arbitrary density and isospin-asymmetry, one can derive an optical potential for many isotopes across the nuclear chart by utilizing the improved local density approximation. In previous works the optical potential was calculated in nuclear matter [10, 12] and more recently proton optical potentials were calculated for a chain of calcium isotopes [77]. New to this work are calculations of the neutron optical potential for ^{40,48}Ca and a direct test of the microscopic spin-orbit term by calculating spin observables.

Overall, we find good agreement with experimental differential elastic scattering data, except in energy regions where unresolved resonances are expected to be important. At the highest energies ($E \simeq 80 - 200\,\mathrm{MeV}$) we also find that the large imaginary volume contribution from microscopic optical potentials tends to suppress elastic scattering compared to experimental data. This feature is enhanced in microscopic calculations of the total cross section, which are too large at high energies due to the large reaction cross section induced by the strongly absorptive imaginary part. We have also computed for the first time in our improved local density approximation the vector analyzing power. We find that the analyzing power for n-^{40}Ca at medium energies is well described by our

microscopic optical potentials, validating in particular its spin-orbit part.

We emphasize that no parameters in the model were tuned to experimental reaction data, and therefore the present work demonstrates the viability of using microscopic optical potentials in regions of the nuclear chart that are unexplored experimentally.

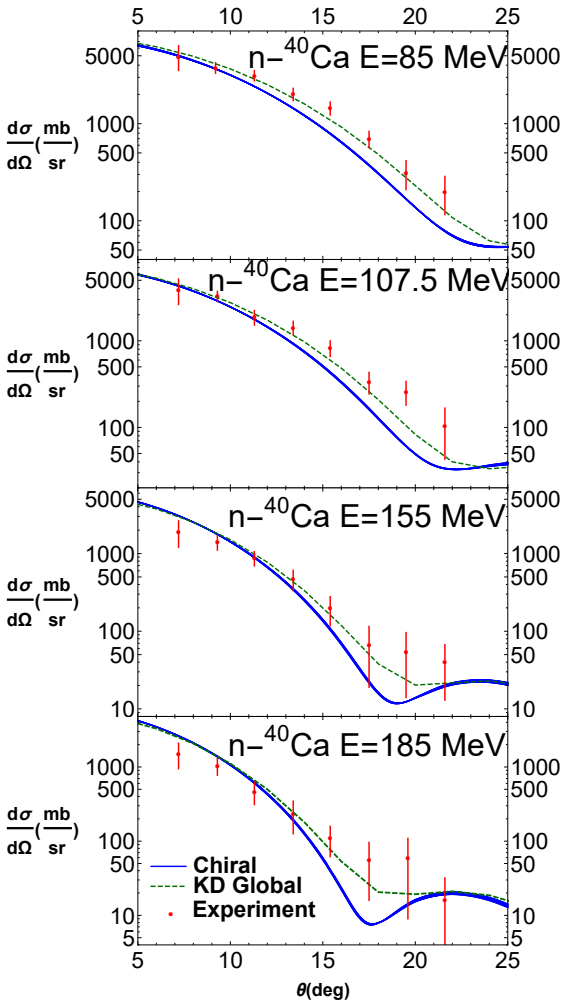

Figure 3.8: Differential elastic scattering cross sections for n-^{40}Ca at projectile energies $E = 85, 107.5, 155, 185$ MeV. The cross sections calculated from the chiral optical potential are given by the blue band. The cross sections calculated from the Koning-Delaroche phenomenological optical potential are given by the green dashed curve, and experimental data are represented by red circles with error bars. Reprinted from [103].

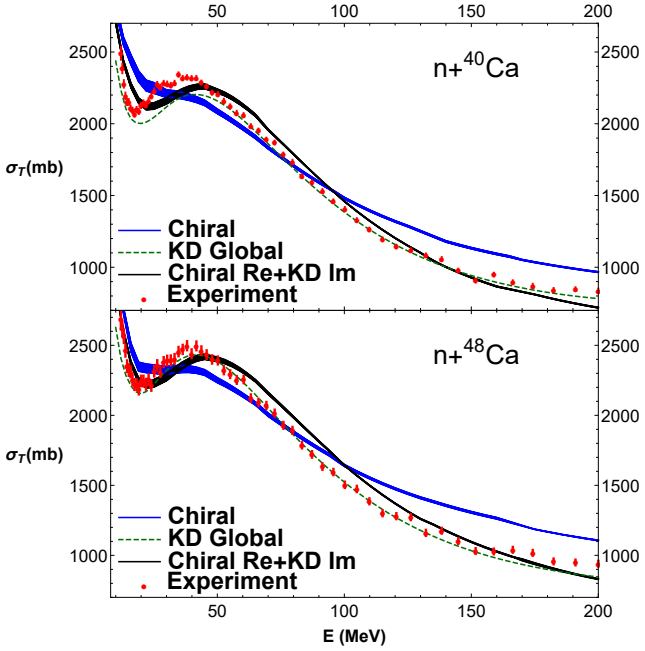

Figure 3.9: The n-^{40,48}Ca total cross sections calculated from the chiral optical potential are shown in blue, and the results of the real chiral optical potential plus a phenomenological imaginary term are given by the black curve. Phenomenological results are represented by dashed green curves. Experimental data are shown as red circles with error bars. Reprinted from [103].

4. MICROSCOPIC GLOBAL OPTICAL POTENTIALS FOR RARE ISOTOPE REACTIONS

We construct from chiral effective field theory two- and three-body forces a microscopic global nucleon-nucleus optical potential suitable for reactions involving radioactive isotopes. Within the improved local density approximation and without any adjustable parameters, we begin by computing local proton and neutron optical potentials for 1800 target nuclei in the mass range $12 < A < 242$ and for energies between $0\,\mathrm{MeV} < E < 200\,\mathrm{MeV}$. We then construct a global optical potential parametrization that depends smoothly on the projectile energy as well as the target nucleus mass number and isospin asymmetry. Elastic scattering observables calculated from the global optical potential are found to be in good agreement with available experimental data for a wide range of projectile energies and target nuclei. Compared to traditional phenomenological optical potentials, we find a strong energy dependence and shell structure features in the Woods-Saxon geometry parameters. For target nuclei with small proton-neutron asymmetry, we find that the real and imaginary optical potential depths exhibit a clear linear dependence on the isospin-asymmetry and preserve the well-known Lane form up to high projectile energies. For nuclei with larger isospin asymmetries, we find evidence for a novel isoscalar term in the low-energy optical potential proportional to the square of the isospin asymmetry. These insights from microscopic many-body theory may be used to inform next-generation phenomenological optical potentials for proton- and neutron-rich isotopes.

4.1 Introduction

Nuclear physics is approaching an exciting new era in which rare isotope beam facilities, such as FRIB, RIBF, FAIR, and Spiral2, will explore previously inaccessible regions of the nuclear chart that are important for understanding the origin of the elements [96, 93, 97, 98] and the properties of neutron stars [76, 99]. Rare isotope beam experiments will produce a flood of new data whose interpretation and connection to nuclear structure will be guided by theoretical modeling. Of particular importance in the context of nuclear reaction studies is the nuclear optical model [42, 100, 44, 5],

where the complicated (and in most cases intractable) problem of solving the N-body Schroedinger equation for nucleon-nucleus scattering in terms of fundamental two- and three-body forces is simplified by assuming the projectile nucleon interacts with an average single-particle potential generated by the target nucleus. Global phenomenological optical potentials [4, 14, 3] are the workhorse for theoretical modeling of nuclear reactions but are currently tuned to limited experimental data near nuclear stability. The worldwide radioactive ion beam program requires next-generation global optical potentials that can reach into unexplored regions of the nuclear chart, provide quantified uncertainty estimates for reaction observables [101, 102], and that are informed by microscopic nuclear theory based on high-precision nuclear forces [33, 2, 103, 1, 28, 22].

In the late 1960s the first phenomenological nucleon-nucleus optical potentials were limited to heavy isotopes with mass numbers $A > 40$ and low scattering energies of $E < 50\,\text{MeV}$. Phenomenological and semi-microscopic optical potentials [3, 4, 104, 105, 106, 107, 108, 109, 110, 111, 5, 9, 14] have improved dramatically since then, and today the most widely used optical potential of Koning and Delaroche [4] is suitable to describe scattering phenomena for stable nuclei with $24 < A < 209$ up to projectile energies of $E \simeq 200\,\text{MeV}$. However, it remains an open question how reliable such phenomenological optical potentials behave for reactions involving exotic isotopes. This is particularly crucial for simulating the late-time freeze-out phase of r-process nucleosynthesis, where photodissociation and radiative capture processes are out of equilibrium and neutron-capture rates play an enhanced role in determining the final abundance pattern of r-process elements [112]. Neutron capture cross sections on neutron-rich isotopes cannot be directly measured with today's experimental techniques, but considerable efforts [113, 114] are being made toward measuring gamma strength functions and nuclear level densities that enter into the Hauser-Feshbach theory for radiative neutron capture in stellar plasmas [115]. Such calculations also require as input the neutron-nucleus optical potential, and especially its imaginary part at low scattering energies [116].

In the present work we construct the first microscopic global nucleon-nucleus optical potential based on an analysis of 1800 isotopes in the framework of many-body perturbation theory

with state-of-the-art nuclear interactions from chiral effective field theory. Compared to phenomenological [3, 4, 106, 108] or semi-microscopic optical potentials [14, 110, 111] that are directly fitted to nuclear reaction data, purely microscopic calculations may have greater predictive power for reactions involving exotic isotopes. Constructing optical potentials via the nucleon self-energy in finite nuclei or nuclear matter from chiral effective field theory (EFT) [10, 12, 27, 28, 29, 22, 30, 31, 1, 77, 103] is a promising route of inquiry since chiral EFT features realistic nuclear interactions based on the symmetries of QCD and a systematic expansion of the nuclear force [32, 33, 2, 117] that provides a method of quantifying theoretical uncertainties. In the present work we use a specific chiral nuclear interaction [38] with momentum-space cutoff $\Lambda = 450\,\text{MeV}$ in the calculation of the nucleon self-energy that is known to reproduce well the saturation energy and density of symmetric nuclear matter [38]. The low-energy constants of the potential are fitted to nucleon-nucleon scattering phase shifts, deuteron properties, and the triton binding energy and lifetime [38].

4.2 Formalism

We begin by calculating up to second order in many-body perturbation theory the nucleon self-energy $\Sigma(k, E(k))$ for $E > 0$, which is equivalent [42] to the optical potential for scattering states. The background medium is taken to be homogeneous nuclear matter with fixed density and isospin asymmetry in the thermodynamic limit. The calculation of the second-order diagrams involves intermediate-state propagators whose energies $E(k) = k^2/(2M) + \Sigma(k, E(k))$ are computed self consistently with the on-shell self-energy. In general the resulting self-energy is complex and energy dependent. In order to construct a nucleon-nucleus optical potential, we compute the nucleon self-energy over the range of densities and isospin asymmetries found in finite nuclei. Since the spin-orbit interaction vanishes in homogeneous nuclear matter, we employ the improved density matrix expansion [46, 47, 55, 48] at the Hartree-Fock level to calculate the spin-orbit contribution to the nuclear energy density functional. In this formulation the spin-orbit interaction is calculated at the Fermi energy and consequently does not have an explicit energy dependence. Density distributions for the target nuclei are calculated in mean field theory with the Skχ450 Skyrme effective

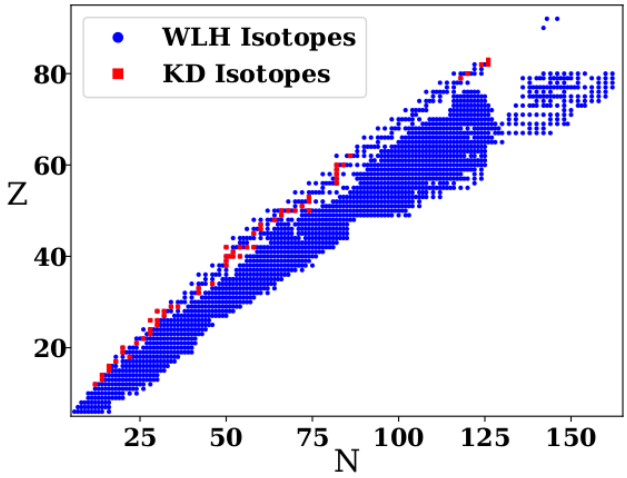

Figure 4.1: Isotopes used in constructing the Whitehead-Lim-Holt (WLH) global microscopic optical potential are shown in blue, and those used for parameterizing the Koning-Delaroche phenomenological optical potential are shown in red.

interaction [43] constrained by the chiral interaction used to calculate the optical potential.

The improved local density approximation (ILDA) is utilized to transition from a nuclear matter optical potential to that of a finite nucleus by folding the density- and isospin-asymmetry-dependent self-energy with the target nucleus density distribution

$$U_{LDA}(E;r) = U_{NM}(E;\rho(r),\delta(r)), \tag{4.1}$$

where $\rho = \rho_n + \rho_p$ and $\delta = (\rho_n - \rho_p)/\rho$. The ILDA is applied by integrating over the radial direction with a Gaussian form factor to account for the nonzero range of the nuclear force [44, 9]:

$$U_{ILDA}(E;r) = \frac{1}{(t\sqrt{\pi})^3}\int U_{LDA}(E;r')e^{\frac{-|\vec{r}-\vec{r}'|^2}{t^2}}d^3r', \tag{4.2}$$

where the range parameter t represents the characteristic length scale of the interaction. The range parameter is derived in this work by calculating the root mean square radii of the local chiral NN interactions presented in Ref. [118]. We use the average value of $t_C = 1.22\,\mathrm{fm}$ for the central terms

of the optical potential and $t_{SO} = 0.98\,\mathrm{fm}$ for the spin-orbit term. In Refs. [77, 103] the effect of varying these range parameters was shown to be small. Within the framework just outlined, we have developed in previous works [10, 12, 77, 103] proton and neutron optical potentials for stable calcium isotopes. In the present work we develop the first microscopic global optical potential, referred to as Whitehead-Lim-Holt (WLH), that is built upon local optical potentials for 1800 target nuclei with mass numbers $12 < A < 242$ and projectile energies $0\,\mathrm{MeV} < E < 200\,\mathrm{MeV}$. This set includes all stable and long lived isotopes, light and medium-mass bound isotopes out to the predicted neutron drip line of iron [119], and heavier neutron-rich isotopes relevant to the r-process [75]. The isotopes for which we have constructed local optical potentials are shown as blue dots in Fig. 4.1 in comparison with the stable isotopes that were used in calibrating the Koning-Delaroche phenomenological optical potential (shown as red squares).

We then fit the position- and energy-dependent optical potentials

$$\begin{aligned} U(r,E) &= U_V(r,E) + iU_W(r,E) + iU_S(r,E) \\ &+U_{SO}(r,E)\vec{\ell}\cdot\vec{\sigma}, \end{aligned} \tag{4.3}$$

to the commonly used Woods-Saxon form $f(r;r_i,a_i) = \frac{1}{1+e^{(r-A^{1/3}r_i)/a_i}}$ (for U_V and U_W) and its derivative (for U_S and U_{SO}). Functional forms for the A, E, and δ dependence of the Woods-Saxon geometry parameters and overall strengths were chosen in order to minimize the least squares fit while using as few parameters as possible. We used the following functional forms to define the global optical potential parametrization:

$$\begin{aligned} \mathcal{U}_V &= u_{V0} + u_{V1}E + u_{V2}E^2 + u_{V3}E^3 + u_{V4}E^4 \\ &+(u_{V5} + u_{V6}E + u_{V7}E^2 + u_{V8}E^3)\delta + u_{V9}e^{u_{V10}E}\delta^2 \\ r_V &= r_{V0} + r_{V1}E + r_{V2}E^2 + r_{V3}A^{-1/3} \\ a_V &= a_{V0} + a_{V1}E + a_{V2}E^2 + a_{V3}E^3 + a_{V4}E^4 \\ &+(a_{V5} + a_{V6}\delta)\delta \end{aligned} \tag{4.4}$$

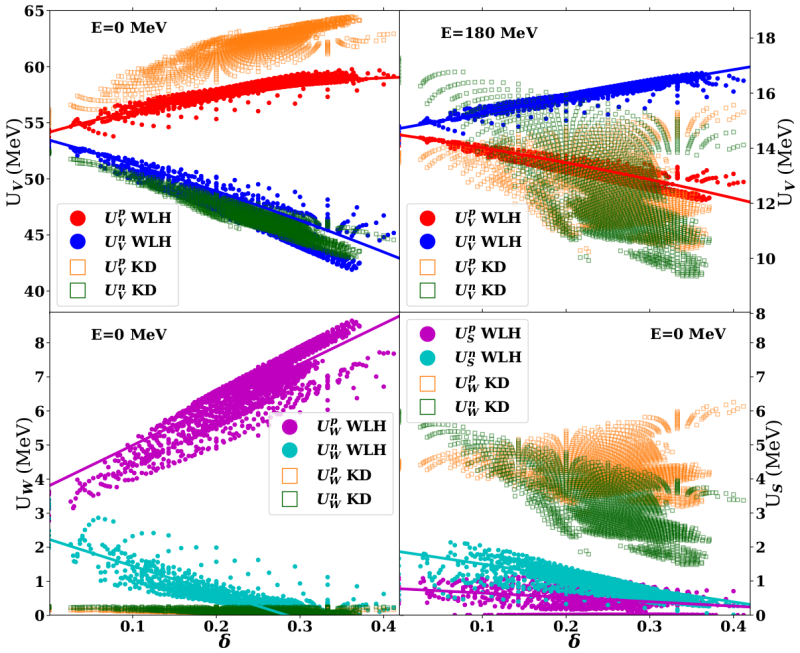

Figure 4.2: The left and right top plots show the depth of the real volume term at $E = 0\,\text{MeV}$ and $E = 180\,\text{MeV}$, respectively, for neutron and proton potentials in red and blue as functions of the isospin asymmetry. The left and right bottom plots show the imaginary volume and surface depths respectively at $E = 0\,\text{MeV}$ for neutron and proton potentials in magenta and cyan as functions of the isospin asymmetry. The points represent values for local potentials and the solid lines are values for the WLH global potential, analogous Koning-Delaroche (KD) values are given by orange and green squares.

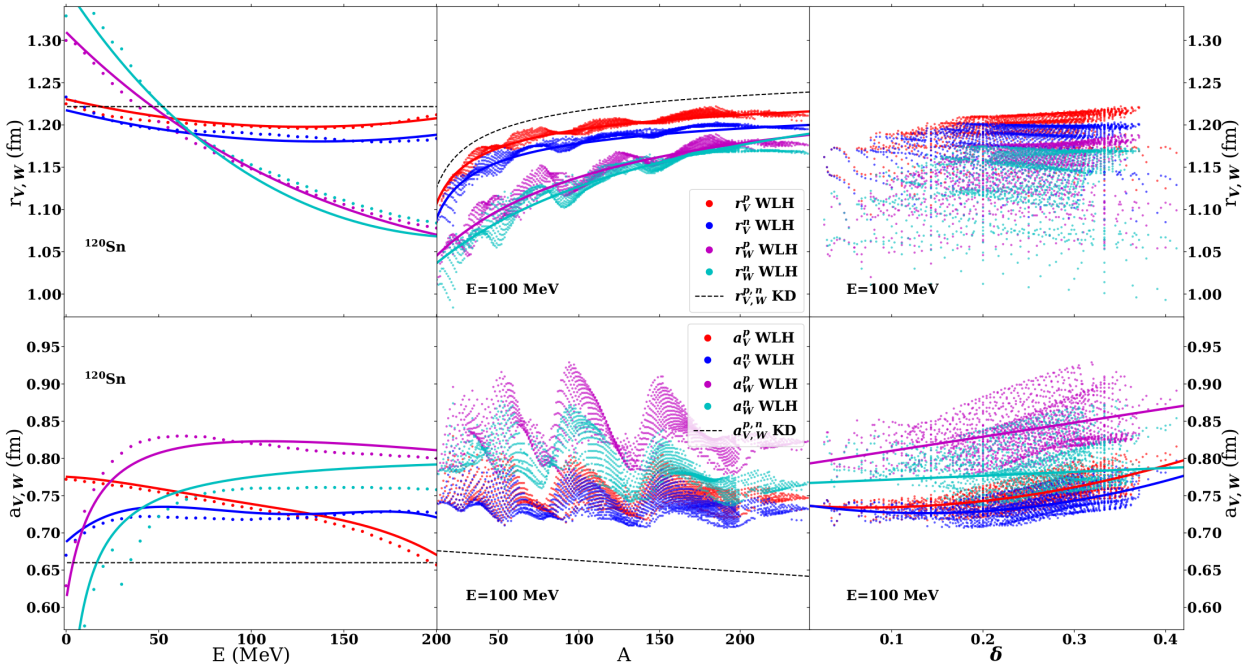

Figure 4.3: The top (bottom) plots show the microscopic real and imaginary radius (diffuseness) parameters for proton and neutron projectiles. The points represent values for local optical potentials and the solid lines are values for the WLH global potential, Koning-Delaroche (KD) values are given by a dashed line. The left panels are for a ^{120}Sn target plotted as a function of energy. The middle and right panels, at $E = 100$ MeV, are plotted as a function of mass number and isospin-asymmetry respectively.

$$
\begin{aligned}
\mathcal{U}_W = \quad & u_{W0} + u_{W1}E + u_{W2}E^2 + (u_{W3} + u_{W4}E)\delta \\
r_W = \quad & r_{W0} + \frac{r_{W1} + r_{W2}A}{r_{W3} + A + r_{W4}E} + r_{W5}E^2 \\
a_W^p = \quad & a_{W0}^p + \frac{a_{W1}^p E}{a_{W2}^p - E} + (a_{W3}^p + a_{W4}^p E)\delta \\
a_W^n = \quad & a_{W0}^n + \frac{a_{W1}^n E}{a_{W2}^n - E} + \left(a_{W3}^n + \frac{a_{W4}^n}{1+E}\right)\delta
\end{aligned}
\tag{4.5}
$$

$$
\begin{aligned}
\mathcal{U}_S^p = \quad & u_{S0}^p + u_{S1}^p E + (u_{S2}^p + u_{S3}^p E)\delta \\
\mathcal{U}_S^n = \quad & u_{S0}^n + u_{S1}^n E + u_{S2}^n E^2 + (u_{S3}^n + u_{S4}^n E \\
& + u_{S5}^n E^2)\delta \\
r_S = \quad & r_{S0} + r_{S1}E + r_{S2}E^2 + r_{S3}A^{-1/3} \\
a_S = \quad & a_{S0} + a_{S1}E + a_{S2}E^2 + a_{S3}A + a_{S4}A^2
\end{aligned}
\tag{4.6}
$$

$$
\begin{aligned}
& \mathcal{U}_{SO} = u_{SO0} + u_{SO1}A + u_{SO2}A^2 + u_{SO3}A^3 \\
& r_{SO} = r_{SO0} + r_{SO1}A^{-1/3} \\
& a_{SO} = a_{SO0} + a_{SO1}A + a_{SO2}A^2 + a_{SO3}A^3.
\end{aligned}
\tag{4.7}
$$

Values for the ~ 70 fit parameters in Eqs. 4.5 - 4.8 can be found in Table 4.1 of Sec. 4.5.

4.3 Results

The microscopic global optical potential constructed in this work is found to have several different features compared to widely used phenomenological optical potentials [3, 4]. The most prominent difference is found in the isovector terms, which are crucial for an accurate description of neutron-rich isotopes. In Fig. 4.2 we show the isospin asymmetry dependence of the real volume U_V, imaginary volume U_W, and imaginary surface U_S depths at $E = 0\,\mathrm{MeV}$. In the top left panel we show the isospin asymmetry dependence of the WLH real volume term which is similar to the results of the KD optical potential for low energy. However, as seen in the top right panel of Fig.

4.2 the two models differ at higher energies as the WLH real volume term preserves the isovector Lane form, $U = U_0 + \tau_z U_I \delta$, even after undergoing an isospin inversion at $E = 115\,\mathrm{MeV}$ where the strength of the isovector term changes sign. As seen in the upper left plot of Fig. 4.2 the WLH real depth exhibits an isoscalar δ^2 dependence for low energies that is consistent with the nuclear matter calculations in Ref. [12]. This extension of the standard Lane form is not accounted for in current phenomenological optical potentials, and is important for accurately modeling reactions with neutron-rich isotopes. In further contrast to the KD optical potential, the WLH potential has a clear isospin asymmetry dependence in both the imaginary volume and surface terms shown in the bottom left panel of Fig. 4.2. The imaginary term must vanish at the Fermi energy, which is $E_F = 0$ for nucleons at their respective drip line. As shown in the bottom right panel, the microscopic WLH imaginary surface term vanishes as δ increases toward values corresponding to the drip line, while the KD model does not. The isovector terms of the optical potential are crucial for describing isotopes off stability and in particular the imaginary isovector term is of significant importance to the neutron capture rates on exotic isotopes involved in the astrophysical r-process [116].

An additional distinction of the WLH optical potential is energy dependent geometry parameters. In the left two panels of Fig. 4.3 we show the energy dependence of the real and imaginary radius and diffuseness parameters for ^{120}Sn, which are indicative of all isotopes considered in this work. By comparison, the assumed form of the Koning-Delaroche optical potential geometry parameters is not only energy independent but also identical for the real and imaginary volume contributions. In general the energy dependence of geometry parameters is as significant as the mass number dependence and more easily described in a closed form. One point of similarity, shown in the top middle panel, is that the WLH radius parameters exhibit the well-known [4, 107, 3] $r \propto A^{-1/3}$ dependence. In the bottom middle panel we find that the mass number dependence of the diffuseness parameters have complicated shell structure effects that would require too many parameters to accurately describe. Instead we include an explicit dependence on the isospin asymmetry, shown in the bottom right plot to have a positive correlation and roughly quadratic behavior.

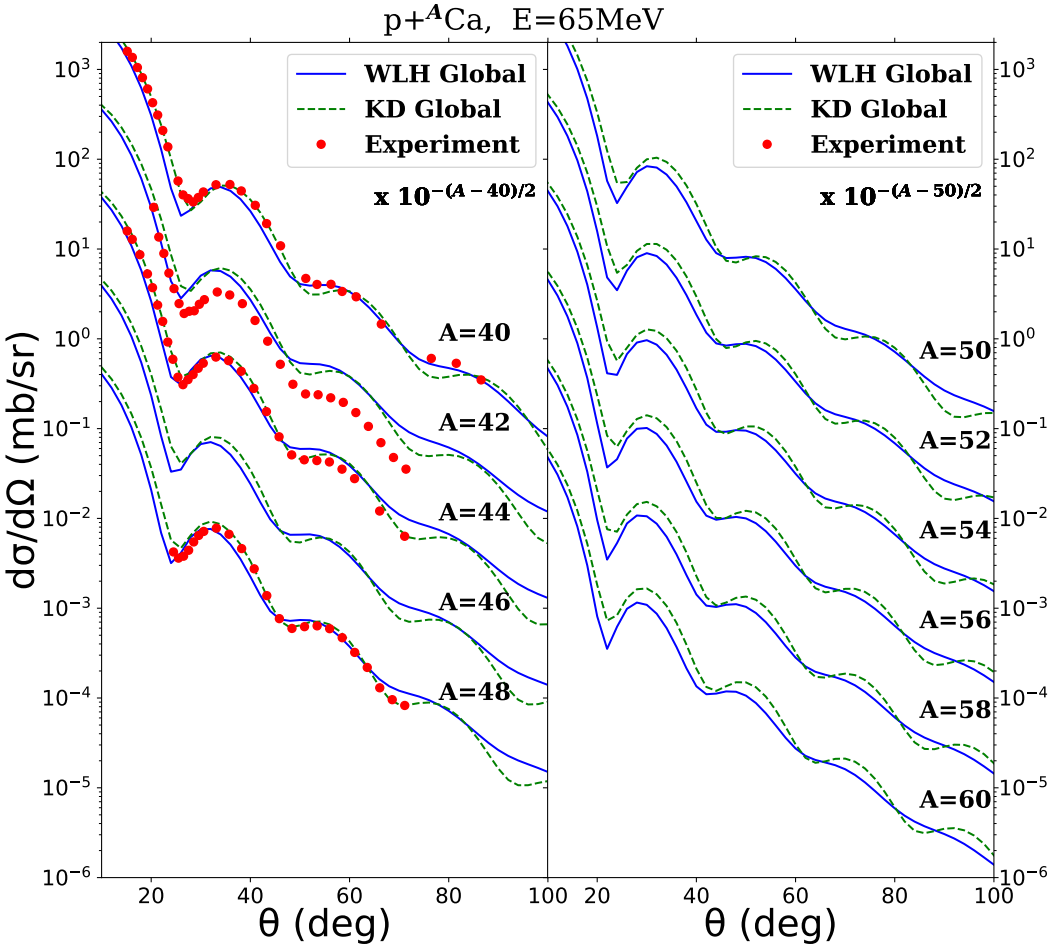

Figure 4.4: Proton elastic scattering cross sections at $E = 65\,\mathrm{MeV}$ for ^{40}Ca -^{60}Ca. Results of the microscopic global optical potential constructed in this work are shown in blue and labeled by WLH Global. Results of the Koning-Delaroche phenomenological global optical potential are given by the green dashed line and labeled as KD Global, experimental data are shown as red dots.

Finally, in the top right plot we show the isospin asymmetry dependence of the radius parameters to be very diffuse with bands at constant values of r_i that result from an interplay of shell effects with the increasing $r \propto A^{-1/3}$ dependence.

In anticipation of future experiments involving radioactive nuclei, we show in Fig. 4.4 the proton differential elastic scattering cross sections on calcium isotopes from $A = 40$ to $A = 60$. The results of the WLH global optical potential (blue lines) are close to those of the KD global optical potential (dashed green lines) and in good agreement with experimental data (red dots), except for the ^{42}Ca data that are also in disagreement with other optical potentials [110]. The microscopic predictions of the WLH potential become systematically smaller than the results of Koning-Delaroche as mass number increases. This is due to the different behavior of the isovector terms in the two optical potentials. In Sec. 4.5 we show plots of neutron and proton elastic scattering cross sections and analyzing powers for a selection of target nuclei to give a more comprehensive demonstration of the effectiveness of the WLH global optical potential. Experimental scattering cross sections are generally well reproduced while analyzing powers stand to benefit from the inclusion of higher-order calculations of the spin-orbit term.

4.4 Summary

We have constructed a microscopic global optical potential based on the many-body perturbation theory calculation of the nucleon self-energy in nuclear matter from chiral two- and three-nucleon interactions. The global optical potential is expressed as a function composed of Woods-Saxon terms with parameters that vary smoothly in E, A, and δ, which can be easily implemented into modern reaction theory codes. A Python script for generating input files needed to run TALYS with the WLH global optical potential may be found at [120]. These dependences are represented by functional forms parametrized to local proton and neutron optical potentials that span projectile energies $0 < E < 200$ MeV and 1800 isotopes with mass numbers $12 < A < 242$. No parameters of the global optical potential are tuned to experimental data. We show that the WLH microscopic optical potential provides a satisfactory description of elastic scattering across the nuclear chart for a wide range of energies. The WLH global optical potential may provide a realistic guide to further

refine next-generation phenomenological optical potentials suitable for nuclear reactions involving radioactive ions.

4.5 Supplementary Material

The WLH global optical potential is expressed in the following form

$$U(r,E) = U_V(r,E) + iU_W(r,E) + iU_S(r,E) \tag{4.8}$$
$$+U_{SO}(r,E)\vec{\ell}\cdot\vec{\sigma},$$

where

$$\begin{aligned} U_V(r,E) &= -\mathcal{U}_V f(r;r_V,a_V) \\ U_W(r,E) &= -\mathcal{U}_W f(r;r_W,a_W) \\ U_S(r,E) &= 4a_S\mathcal{U}_S\frac{d}{dr}f(r;r_S,a_S) \\ U_{SO}(r,E) &= \mathcal{U}_{SO}\frac{1}{m_\pi^2}\frac{1}{r}\frac{d}{dr}f(r;r_{SO},a_{SO}), \end{aligned} \tag{4.9}$$

and

$$f(r;r_i,a_i) = \frac{1}{1+e^{(r-A^{1/3}r_i)/a_i}}. \tag{4.10}$$

The depth, radial size and diffuseness of each term are given by $\mathcal{U}_i$, r_i,a_i and A is the mass number.

The fit parameters in the above equations are listed in Table 4.1 for neutron and proton projectiles. The parametrization of the imaginary surface term is only valid for neutron projectile energies of $E < 40\,\mathrm{MeV}$ and proton projectile energies of $E < 30\,\mathrm{MeV}$. We find no microscopic evidence of an imaginary surface peak beyond these energies.

We calculate scattering observables from the WLH microscopic global optical potential and compare to results of the Koning-Delaroche phenomenological optical potential and experiment. In Figs. 4.5 and 4.6 we show neutron and proton elastic scattering for a wide range of isotopes and

$\mathcal{U}_V$	$u^p_{V0} = 54.154$ $u^n_{V0} = 53.459$	$u^p_{V1} = -0.252$ $u^n_{V1} = -0.2356$	$u^p_{V2} = -0.0011$ $u^n_{V2} = -0.00133$	$u^p_{V3} = 1.19 \cdot 10^{-5}$ $u^n_{V3} = 1.317 \cdot 10^{-5}$	$u^p_{V4} = -2.6 \cdot 10^{-8}$ $u^n_{V4} = -2.88 \cdot 10^{-8}$	$u^p_{V5} = 20.87$ $u^n_{V5} = -20.58$	$u^p_{V6} = -0.306$ $u^n_{V6} = 0.317$
	$u^p_{V7} = 0.00172$ $u^n_{V7} = -0.00158$	$u^p_{V8} = -4.46 \cdot 10^{-6}$ $u^n_{V8} = 3.49 \cdot 10^{-6}$	$u^p_{V9} = -21.92$ $u^n_{V9} = -10.96$	$u^p_{V10} = -0.01035$ $u^n_{V10} = -0.0155$			
r_V	$r^p_{V0} = 1.310$ $r^n_{V0} = 1.298$	$r^p_{V1} = -5.09 \cdot 10^{-4}$ $r^n_{V1} = -5.41 \cdot 10^{-4}$	$r^p_{V2} = 1.98 \cdot 10^{-6}$ $r^n_{V2} = 1.98 \cdot 10^{-6}$	$r^p_{V3} = -0.391$ $r^n_{V3} = -0.397$			
a_V	$a^p_{V0} = 0.773$ $a^n_{V0} = 0.699$	$a^p_{V1} = -1.28 \cdot 10^{-4}$ $a^n_{V1} = 0.0023$	$a^p_{V2} = -6.1 \cdot 10^{-6}$ $a^n_{V2} = -3.77 \cdot 10^{-5}$	$a^p_{V3} = 5.39 \cdot 10^{-8}$ $a^n_{V3} = 2.38 \cdot 10^{-7}$	$a^p_{V4} = -1.67 \cdot 10^{-10}$ $a^n_{V4} = -5.14 \cdot 10^{-10}$	$a^p_{V5} = -0.746$ $a^n_{V5} = -0.171$	$a^p_{V6} = 0.522$ $a^n_{V6} = 0.625$
$\mathcal{U}_W$	$u^p_{W0} = 3.80$ $u^n_{W0} = 2.23$	$u^p_{W1} = 0.237$ $u^n_{W1} = 0.262$	$u^p_{W2} = -4.67 \cdot 10^{-4}$ $u^n_{W2} = -5.85 \cdot 10^{-4}$	$u^p_{W3} = 11.9$ $u^n_{W3} = -7.84$	$u^p_{W4} = -0.077$ $u^n_{W4} = -0.046$		
r_W	$r^p_{W0} = 0.543$ $r^n_{W0} = 0.450$	$r^p_{W1} = 48.78$ $r^n_{W1} = 86.82$	$r^p_{W2} = 0.708$ $r^n_{W2} = 0.830$	$r^p_{W3} = 54.23$ $r^n_{W3} = 84.17$	$r^p_{W4} = 0.499$ $r^n_{W4} = 0.755$	$r^p_{W5} = 9.93 \cdot 10^{-7}$ $r^n_{W5} = 2.34 \cdot 10^{-6}$	
a_W	$a^p_{W0} = 0.546$ $a^n_{W0} = 0.407$	$a^p_{W1} = -0.287$ $a^n_{W1} = -0.394$	$a^p_{W2} = -17.1$ $a^n_{W2} = -9.39$	$a^p_{W3} = 0.376$ $a^n_{W3} = 0.0599$	$a^p_{W4} = -0.00187$ $a^n_{W4} = -0.853$		
$\mathcal{U}_S$	$u^p_{S0} = 0.774$ $u^n_{S0} = 1.866$	$u^p_{S1} = -0.0216$ $u^n_{S1} = -0.0546$	$u^p_{S2} = -1.281$ $u^n_{S2} = 1.41 \cdot 10^{-4}$	$u^p_{S3} = 0.0316$ $u^n_{S3} = -3.70$	$u^n_{S4} = 0.4218$	$u^n_{S5} = -0.00842$	
r_S	$r^p_{S0} = 1.134$ $r^n_{S0} = 1.238$	$r^p_{S1} = -0.0120$ $r^n_{S1} = 0.00275$	$r^p_{S2} = -3.25 \cdot 10^{-8}$ $r^n_{S2} = -2.14 \cdot 10^{-4}$	$r^p_{S3} = -0.836$ $r^n_{S3} = -1.266$			
a_S	$a^p_{S0} = 0.146$ $a^n_{S0} = 0.578$	$a^p_{S1} = 0.00362$ $a^p_{S1} = 0.0169$	$a^p_{S2} = -3.47 \cdot 10^{-4}$ $a^n_{S2} = -3.82 \cdot 10^{-4}$	$a^p_{S3} = 0.019$ $a^n_{S3} = 5.47 \cdot 10^{-4}$	$a^p_{S4} = -1.32 \cdot 10^{-4}$ $a^n_{S4} = 3.91 \cdot 10^{-6}$		
$\mathcal{U}_{SO}$	$u_{SO0} = 8.852$	$u_{SO1} = 0.0127$	$u_{SO2} = -2.02 \cdot 10^{-4}$	$u_{SO3} = 5.57 \cdot 10^{-7}$			
r_{SO}	$r_{SO0} = 1.260$	$r_{SO1} = -0.827$					
a_{SO}	$a_{SO0} = 0.663$	$a_{SO1} = 0.0032$	$a_{SO2} = -2.83 \cdot 10^{-5}$	$a_{SO3} = 6.58 \cdot 10^{-8}$			

Table 4.1: WLH global optical potential fit parameters.

a variety of scattering energies to demonstrate the performance of the WLH optical potential compared to phenomenology and experiment. Additionally we plot the analyzing power for neutron and proton projectiles and a variety of target nuclei in Fig. 4.7. Neutron elastic scattering cross sections are on par with phenomenology for energies $E < 20\,\mathrm{MeV}$ past which the WLH results slightly overestimate for larger scattering angles. The top left panel of Fig. 4.5 shows neutron scattering with ^{14}N which is outside the mass range for the Koning-Delaroche potential and may indicate the extrapolative power of phenomenological models. In Fig. 4.6 proton elastic scattering data are also well reproduced by the WLH calculations with tendency to slightly underestimate cross sections. In Fig. 4.7 analyzing powers calculated by the WLH potential generally reproduce the angular pattern of experimental data, while often overestimating or underestimating the magnitude of peaks and troughs. This may be improved by inclusion of higher order perturbative terms and isovector contributions to the spin-orbit interaction.

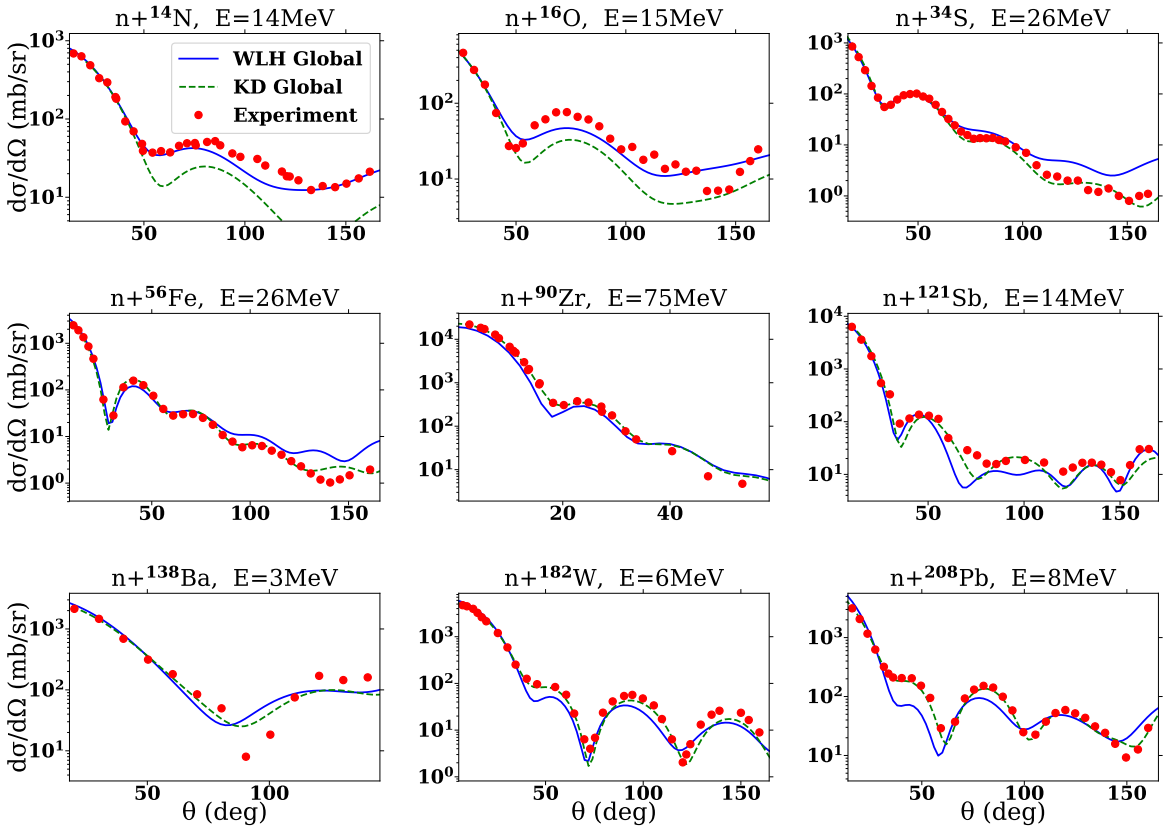

Figure 4.5: Neutron elastic scattering cross sections for a selection of target isotopes at varied energies. Results of the microscopic global optical potential constructed in this work are shown in blue and labeled by WLH Global. Results of the Koning-Delaroche phenomenological global optical potential are given by the green dashed line and labeled as KD global, experimental data are shown as red dots.

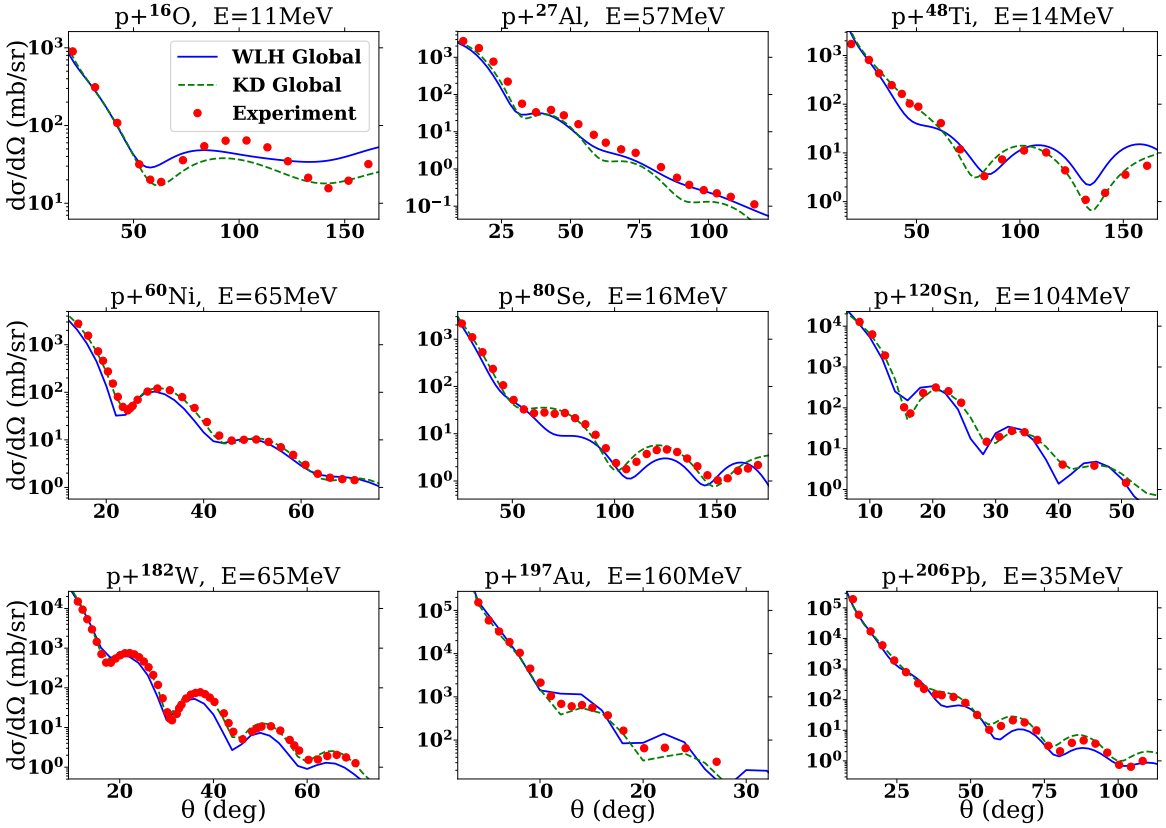

Figure 4.6: Proton elastic scattering cross sections for a selection of target isotopes at varied energies. Results of the microscopic global optical potential constructed in this work are shown in blue and labeled by WLH Global. Results of the Koning-Delaroche phenomenological global optical potential are given by the green dashed line and labeled as KD global, experimental data are shown as red dots.

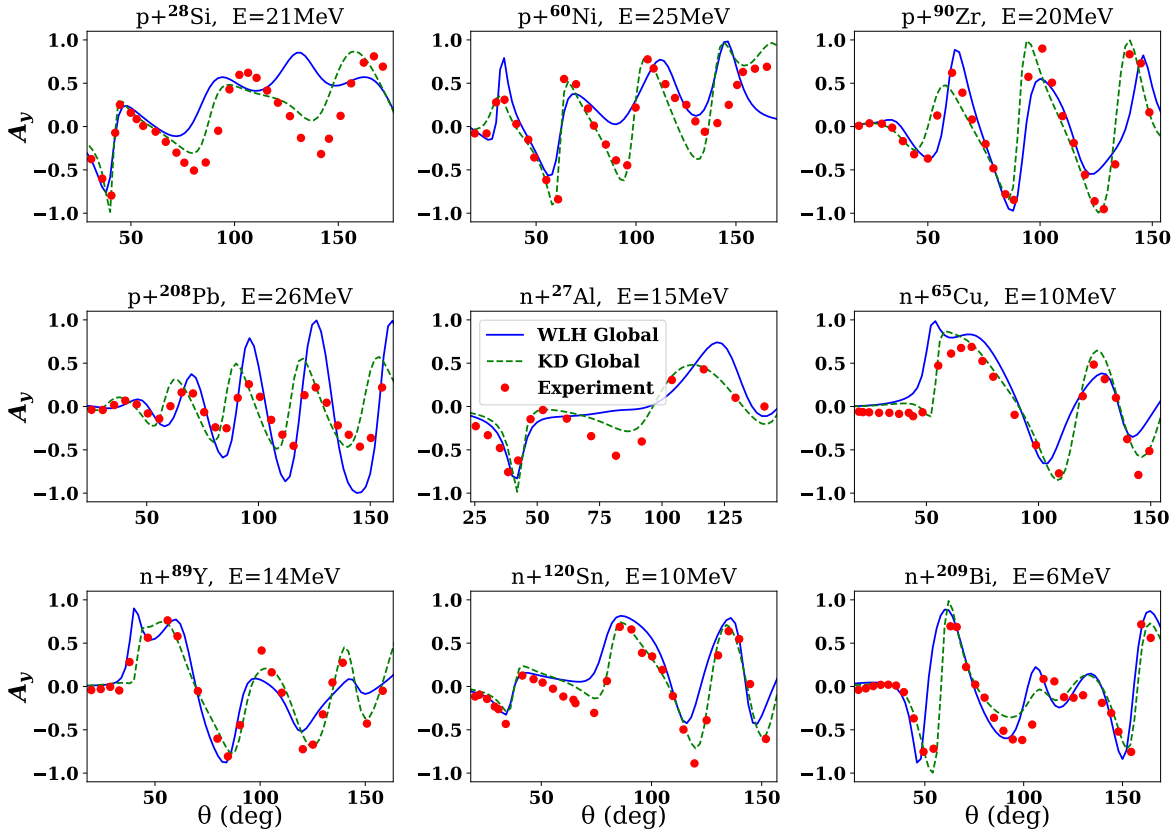

Figure 4.7: Proton and neutron analyzing powers for a selection of target isotopes at varied energies. Results of the microscopic global optical potential constructed in this work are shown in blue and labeled by WLH Global. Results of the Koning-Delaroche phenomenological global optical potential are given by the green dashed line and labeled as KD Global, experimental data are shown as red dots.

5. FERMI LIQUID THEORY*

Fermi liquid theory [121, 122, 123, 124] is widely used to describe the transport, response and dynamical properties of nuclear many-body systems [125, 126, 127, 128, 129, 130, 131, 132, 133]. The key quantity in this theory is the quasiparticle interaction, defined as the second functional derivative of the energy with respect to the quasiparticle distribution function. For many years the primary focus of investigation has been the central part of the quasiparticle interaction and its associated Fermi liquid parameters, which are directly related to static properties of the interacting ground state such as the incompressibility, isospin-asymmetry energy and magnetic susceptibility. The central terms include scalar operators in spin and isospin space, but more recently noncentral contributions [134, 135] that couple spin and momenta have been studied together with their impact on the density and spin-density response functions of neutron matter [136, 137, 138, 139]. Extending these results to nuclear matter with equal numbers of protons and neutrons and to systems with arbitrary isospin asymmetry will be needed to better understand neutrino transport and emissivity in neutron stars, proto-neutron star cooling [140], electron transport in neutron stars [141], the evolution of shell structure and single-particle states in nuclei far from stability [142, 143], and nuclear collective excitations (spin and spin-isospin modes together with rotational modes of deformed nuclei) [144, 145, 146]. An important motivation of the present work is to provide microscopic guidance for the tensor forces employed in modern mean field effective interactions and nuclear energy density functionals. Including as well new estimates and uncertainties on the central Fermi liquid parameters, which are more directly related to nuclear observables, the present study will complement other recent efforts [147, 148, 149, 150, 151, 56] to constrain energy density functionals from microscopic many-body theory. The importance of tensor forces in mean field modeling is a question of ongoing debate. While there is skepticism [152, 153] that tensor forces can lead to a meaningful improvement in fits to nuclear ground state energies, there is

*Reprinted with permission from "Tensor Fermi liquid parameters in nuclear matter from chiral effective field theory" by J. W. Holt, N. Kaiser, and T. R. Whitehead, 2018. Phys.Rev.C, 97, 054325 , Copyright [2018] American Physical Society.

strong evidence that the description of single-particle energies [142, 143, 154, 155], beta-decay half-lives [156], and spin-dependent collective excitations [145, 146] are systematically improved with the inclusion of tensor forces (for a recent review, see Ref. [157]). One of the main driving questions is the extent to which the effective medium-dependent tensor force in mean field models resembles the fundamental tensor component of the free-space nucleon-nucleon interaction arising from π + ρ meson exchange. A main conclusion of the present work is that the proton-neutron effective tensor force is enhanced over the free-space tensor interaction due to three-body forces and second-order perturbative contributions. On the other hand, the proton-proton and neutron-neutron tensor forces are considerably smaller in magnitude. In addition, we find evidence for a large isovector cross-vector interaction that to our knowledge has not been previously studied in phenomenological mean field modeling of nuclei.

The quasiparticle interaction can be computed microscopically from realistic two- and three-body forces starting from the perturbative expansion of the energy density and taking appropriate functional derivatives with respect to the Fermi distribution functions. For nuclear or astrophysical systems with densities near or above that of saturated nuclear matter, it is essential to consider the effects of three-body forces. To date three-nucleon forces have been included in calculations of the central and exchange-tensor quasiparticle interaction in nuclear matter [158, 159, 160, 161, 162] and the full quasiparticle interaction in neutron matter [163]. In the present work our aim is to extend the calculations in Ref. [163] to the case of symmetric nuclear matter. This is a natural step before considering the more general case of isospin-asymmetric nuclear matter.

We take as a starting point a class [164, 165, 166, 167, 38, 168] of realistic two and three-body nuclear forces derived within the framework of chiral effective field theory [32, 169, 2]. The two-body force is treated at both next-to-next-to-leading order (N2LO) and N3LO in the chiral power counting, while the three-body force is only considered at N2LO. Although the inclusion of consistent three-body forces at N3LO [170, 171] in the chiral power counting will be needed for improved theoretical uncertainty estimates [35, 36, 172], the present set of nuclear force models has been shown to give a good description of nuclear matter saturation [38, 173], the nuclear

liquid-gas phase transition [39], and the volume components of nucleon-nucleus optical potentials [174, 175] when used at second order in many-body perturbation theory. In addition to the order in the chiral expansion, the resolution scale (related to the momentum-space cutoff in the nuclear potential) is varied in order to assess the theoretical uncertainties.

5.1 Quasiparticle interaction in symmetric nuclear matter

The quasiparticle interaction in symmetric nuclear matter has the general form [135]

$$\mathcal{F}(\vec{p}_1,\vec{p}_2\,) = \mathcal{A}(\vec{p}_1,\vec{p}_2\,) + \mathcal{A}'(\vec{p}_1,\vec{p}_2\,)\vec{\tau}_1\cdot\vec{\tau}_2, \tag{5.1}$$

where

$$\begin{aligned}\mathcal{A}(\vec{p}_1,\vec{p}_2\,) \;&=\; f(\vec{p}_1,\vec{p}_2\,) + g(\vec{p}_1,\vec{p}_2\,)\vec{\sigma}_1\cdot\vec{\sigma}_2 \\ &\quad + h(\vec{p}_1,\vec{p}_2\,)S_{12}(\hat{q}) + k(\vec{p}_1,\vec{p}_2\,)S_{12}(\hat{P}) \\ &\quad + \ell(\vec{p}_1,\vec{p}_2\,)(\vec{\sigma}_1\times\vec{\sigma}_2)\cdot(\hat{q}\times\hat{P}),\end{aligned} \tag{5.2}$$

and analogously for $\mathcal{A}'$ except with the replacement $\{f,g,h,k,\ell\} \longrightarrow \{f',g',h',k',\ell'\}$. The relative momentum is defined by $\vec{q} = \vec{p}_1 - \vec{p}_2$ and the center of mass momentum is given by $\vec{P} = \vec{p}_1 + \vec{p}_2$. The tensor operator has the usual form $S_{12}(\hat{v}) = 3\vec{\sigma}_1\cdot\hat{v}\,\vec{\sigma}_2\cdot\hat{v} - \vec{\sigma}_1\cdot\vec{\sigma}_2$. The interaction in Eq. (5.2) is invariant under rotations, time-reversal, parity, and the exchange of particle labels. The presence of the medium breaks Galilean invariance, and two new structures (the "center-of-mass tensor" $S_{12}(\hat{P})$ and "cross-vector" $(\vec{\sigma}_1\times\vec{\sigma}_2)\cdot(\hat{q}\times\hat{P})$ operators) arise [135] that depend explicitly on the center-of-mass momentum $\vec{P}$. Neither of these terms are found in the free-space nucleon-nucleon potential.

By assumption the two quasiparticle momenta $\vec{p}_1$ and $\vec{p}_2$ lie on the Fermi surface ($|\vec{p}_1| = |\vec{p}_2| = k_f$) and therefore the scalar functions $\{f,g,h,k,\ell,f',g',h',k',\ell'\}$ admit a decomposition in Leg-

endre polynomials:

$$\begin{aligned} f(\vec{p}_1, \vec{p}_2) &= \sum_{L=0}^{\infty} f_L(k_f) P_L(\cos\theta), \\ f'(\vec{p}_1, \vec{p}_2) &= \sum_{L=0}^{\infty} f'_L(k_f) P_L(\cos\theta), \ldots \end{aligned} \tag{5.3}$$

where $\cos\theta = \hat{p}_1 \cdot \hat{p}_2$. The expansion coefficients $f_L, f'_L, \ldots$ are referred to as the Fermi liquid parameters. In relating the Fermi liquid parameters to nuclear observables, it is often convenient to multiply by the density of states

$$N_0 = 2M^* k_f / \pi^2 \tag{5.4}$$

with M^* the effective nucleon mass, to obtain dimensionless parameters $F_L = N_0 f_L, \ldots$.

The ten scalar functions in Eq. (5.2) can be extracted from linear combinations of the spin-space and isospin-space matrix elements, but the decomposition will depend on the orientation of the orthogonal vectors $\vec{q}$ and $\vec{P}$. For instance, if $\vec{P} = P\hat{z}$ and $\vec{q} = q\hat{x}$, then

$$
\begin{aligned}
f &= (6\mathcal{F}^1_{1,1;1,1} + 3\mathcal{F}^1_{1,0;1,0} + 3\mathcal{F}^1_{0,0;0,0} \\
&\quad +2\mathcal{F}^0_{1,1;1,1} + \mathcal{F}^0_{1,0;1,0} + \mathcal{F}^0_{0,0;0,0})/16\,, \\
f' &= (2\mathcal{F}^1_{1,1;1,1} + \mathcal{F}^1_{1,0;1,0} + \mathcal{F}^1_{0,0;0,0} \\
&\quad -2\mathcal{F}^0_{1,1;1,1} - \mathcal{F}^0_{1,0;1,0} - \mathcal{F}^0_{0,0;0,0})/16\,, \\
g &= (6\mathcal{F}^1_{1,1;1,1} + 3\mathcal{F}^1_{1,0;1,0} - 9\mathcal{F}^1_{0,0;0,0} \\
&\quad +2\mathcal{F}^0_{1,1;1,1} + \mathcal{F}^0_{1,0;1,0} - 3\mathcal{F}^0_{0,0;0,0})/48\,, \\
g' &= (2\mathcal{F}^1_{1,1;1,1} + \mathcal{F}^1_{1,0;1,0} - 3\mathcal{F}^1_{0,0;0,0} \\
&\quad -2\mathcal{F}^0_{1,1;1,1} - \mathcal{F}^0_{1,0;1,0} + 3\mathcal{F}^0_{0,0;0,0})/48\,, \\
h &= (3\mathcal{F}^1_{1,1;1,-1} + \mathcal{F}^0_{1,1;1,-1})/12\,, \\
h' &= (\mathcal{F}^1_{1,1;1,-1} - \mathcal{F}^0_{1,1;1,-1})/12\,, \\
k &= (3\mathcal{F}^1_{1,1;1,1} - 3\mathcal{F}^1_{1,0;1,0} + 3\mathcal{F}^1_{1,1;1,-1} \\
&\quad +\mathcal{F}^0_{1,1;1,1} - \mathcal{F}^0_{1,0;1,0} + \mathcal{F}^0_{1,1;1,-1})/24 \\
k' &= (\mathcal{F}^1_{1,1;1,1} - \mathcal{F}^1_{1,0;1,0} + \mathcal{F}^1_{1,1;1,-1} \\
&\quad -\mathcal{F}^0_{1,1;1,1} + \mathcal{F}^0_{1,0;1,0} - \mathcal{F}^0_{1,1;1,-1})/24 \\
\ell &= (3\mathcal{F}^1_{1,1;0,0} + \mathcal{F}^0_{1,1;0,0})/4\sqrt{2}\,, \\
\ell' &= (\mathcal{F}^1_{1,1;0,0} - \mathcal{F}^0_{1,1;0,0})/4\sqrt{2}\,,
\end{aligned}
\tag{5.5}
$$

with the notation $\mathcal{F}^T_{S,m_s;S',m'_s} = \langle Sm_sT|\mathcal{F}|S'm'_sT\rangle$. The quasiparticle interaction is defined as the second functional derivative of the energy E with respect to the occupation probabilities $n_{\vec{p}st}$:

$$
\begin{aligned}
\delta E &= \sum_{\vec{p}_1 s_1 t_1} \epsilon_{\vec{p}_1}\, \delta n_{\vec{p}_1 s_1 t_1} \\
&\quad + \frac{1}{2\Omega} \sum_{\substack{\vec{p}_1 s_1 t_1 \\ \vec{p}_2 s_2 t_2}} \mathcal{F}(\vec{p}_1 s_1 t_1; \vec{p}_2 s_2 t_2) \delta n_{\vec{p}_1 s_1 t_1} \delta n_{\vec{p}_2 s_2 t_2},
\end{aligned}
\tag{5.6}
$$

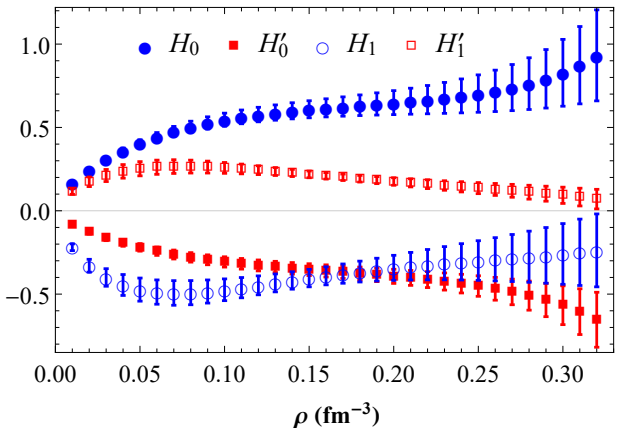

Figure 5.1: Total $L = 0, 1$ Fermi liquid parameters of the relative tensor interaction from two- and three-body forces as a function of the density. Error bars are obtained from the standard deviation of the five chiral potentials considered in the present work. Reprinted from [41].

where Ω is a normalization volume. The quasiparticle interaction $\mathcal{F}$ in momentum space has units fm^2, s_i labels the spin quantum number of quasiparticle i, and t_i labels the isospin quantum number. In the present work we consider contributions to the quasiparticle interaction up to second order in many-body perturbation theory.

5.2 Results

In the present section we focus on the noncentral components of the quasiparticle interaction from the five different chiral nuclear forces (n2lo450, n2lo500, n3lo414, n3lo450, n3lo500) [164, 165, 166, 167, 38, 168]. We focus primarily on the role of three-body forces and second-order perturbative contributions. The quality of the nuclear force models and perturbative many-body method is benchmarked by comparing the nuclear incompressibility, isospin asymmetry energy, and effective mass (which are related to specific central Fermi liquid parameters) with empirical values. We also study the convergence of the Legendre polynomial decomposition for both central and noncentral forces.

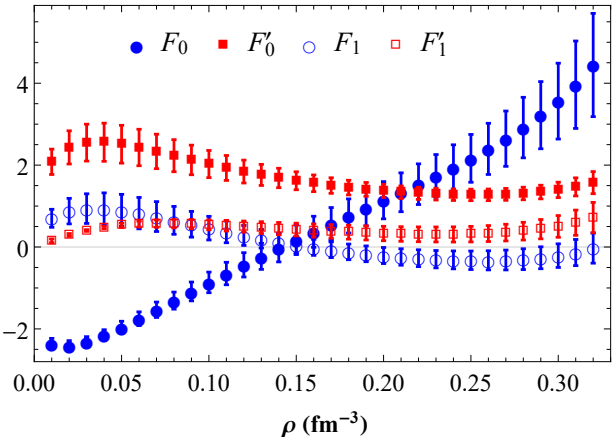

Figure 5.2: Total $L = 0, 1$ Fermi liquid parameters of the spin-independent central parts of the quasiparticle interaction from two- and three-body forces as a function of the density. Error bars are obtained from the standard deviation of the five chiral potentials considered in the present work. Reprinted from [41].

5.2.1 Central components of the quasiparticle interaction

In previous work [162] we have computed the central Fermi liquid parameters in symmetric nuclear matter including the effects of three-body forces. We update those results to include theoretical uncertainties obtained by varying the chiral order and momentum-space cutoff of the nuclear potential. In comparison to Ref. [162] we also consider a larger range of densities in the present calculation. We then use standard relations to study various nuclear observables that are directly related to the low-harmonic central Fermi liquid parameters. Since the tensor Fermi liquid parameters for symmetric nuclear matter are largely unconstrained by empirical data, benchmarking the central terms to empirical data is an important check on the nuclear force models and many-body methods.

In Figs. 5.2 and 5.5 we show the $L = 0, 1$ Fermi liquid parameters associated with the F, F', G, G' components of the quasiparticle interaction. The isotropic spin- and isospin-independent Fermi liquid parameter F_0 is related to the nuclear incompressibility $\mathcal{K} = 9\partial P/\partial\rho$, where $P = \rho^2 \frac{\partial(E/A)}{\partial\rho}$, through

$$\mathcal{K} = \frac{3k_F^2}{M^*}\left(1 + F_0\right). \tag{5.7}$$

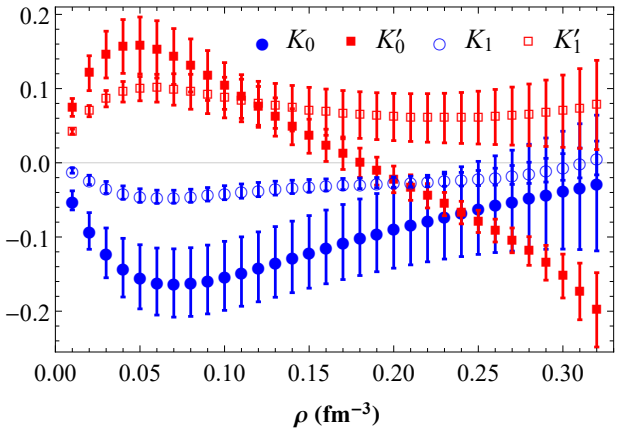

Figure 5.3: Total $L = 0, 1$ Fermi liquid parameters of the center-of-mass tensor interaction from two- and three-body forces as a function of the density. Error bars are obtained from the standard deviation of the five chiral potentials considered in the present work. Reprinted from [41].

From Fig. 5.2 we see that $F_0 < -1$ for $\rho < 0.10\,\mathrm{fm}^{-3}$, which corresponds to the well known instability of nuclear matter to density fluctuations associated with spinodal decomposition and cluster formation. However, the nearly linear dependence of F_0 on the nuclear density results in a strongly increasing nuclear incompressibility, which we show in Fig. 5.6. At $\rho = \rho_0$ the incompressibility lies in the range $190\,\mathrm{MeV} < \mathcal{K} < 380\,\mathrm{MeV}$. While this is consistent with the empirical estimate of $220\,\mathrm{MeV} < \mathcal{K} < 260\,\mathrm{MeV}$ [176], the large theoretical range is due to the fact the n2lo450, n2lo500, and n3lo500 nuclear forces saturate at too low of a density $\rho \simeq 0.14 - 0.15\,\mathrm{fm}^{-3}$. In this case the contribution $\sim 18\rho\frac{\partial(E/A)}{\partial\rho}$ that is linear in the density strongly enhances the nuclear incompressibility.

The quasiparticle effective mass M^* is related to the Landau parameter F_1 through

$$\frac{M^*}{M} = 1 + \frac{F_1}{3}, \tag{5.8}$$

with $M = 938.9182\,\mathrm{MeV}$ the average nucleon mass. From Fig. 5.2 we find that $F_1 > 0$ for $\rho < \rho_0$ and consequently the effective mass is larger than the free-space mass. For $\rho > \rho_0$ the effective mass is typically less than that of a free nucleon, but the decrease in the effective mass

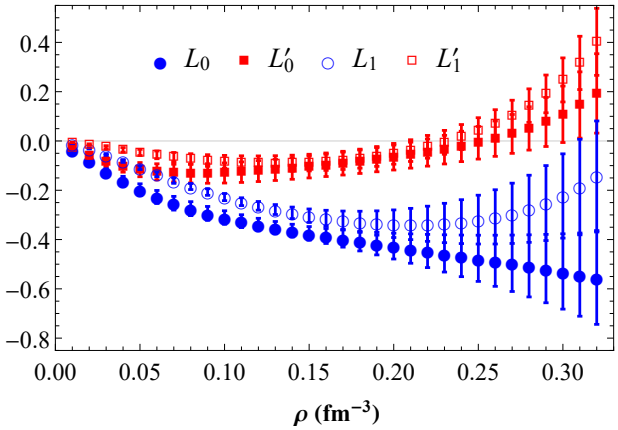

Figure 5.4: Total $L = 0, 1$ Fermi liquid parameters of the cross-vector interaction from two- and three-body forces as a function of the density. Error bars are obtained from the standard deviation of the five chiral potentials considered in the present work. Reprinted from [41].

with increasing density is not nearly as large as in most mean field models and other approaches to scaling masses [130] at first order. The large effective mass is due almost solely to the second-order particle-hole diagram, which gives a contribution $F_1^{(2ph)} \simeq 1$ for all densities up to $\rho = 2\rho_0$. From the study of nuclear level densities in the vicinity of the Fermi surface, the effective mass has been estimated to lie close to that of a free nucleon $M^* \simeq M$. In Fig. 5.7 we show the effective mass as a function of density together with the theoretical uncertainty estimates. At saturation density we find the range $0.9 < M^*/M < 1.1$. Since $M^*/M \to 1$ as $\rho \to 0$, the effective mass must rise rather quickly at low densities.

We define the density-dependent isospin-asymmetry energy $S_2(\rho)$ as the coefficient of the quadratic term in an expansion of the energy per particle of isospin-asymmetric nuclear matter in powers of the parameter $\delta_{np} = \frac{\rho_n - \rho_p}{\rho_n + \rho_p}$:

$$\frac{E}{A}(\rho, \delta_{np}) = \frac{E}{A}(\rho, 0) + S_2(\rho)\delta_{np}^2 + \cdots \tag{5.9}$$

Generically [177, 40] the energy per particle contains non-analytic contributions in δ_{np} beyond the quadratic term in Eq. (5.9) when second-order perturbative corrections are included in the equation

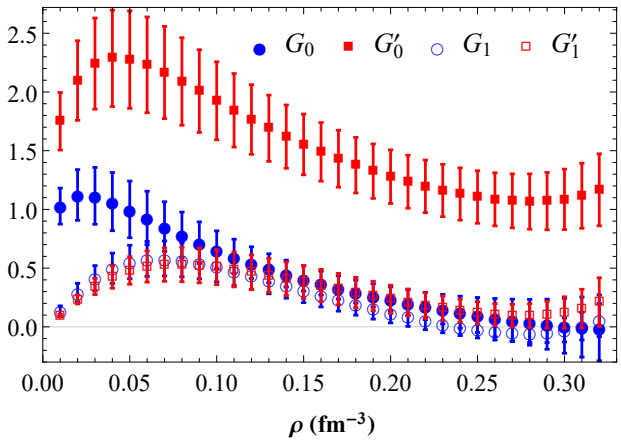

Figure 5.5: Total $L = 0, 1$ Fermi liquid parameters of the spin-dependent central parts of the quasiparticle interaction from two- and three-body forces as a function of the density. Error bars are obtained from the standard deviation of the five chiral potentials considered in the present work. Reprinted from [41].

of state, but at low temperatures it is nevertheless a good approximation to retain only the quadratic term in the expansion in Eq. (5.9). The isospin-asymmetry energy is related to the isotropic part of the F' contribution to the quasiparticle interaction:

$$S_2 = \frac{k_F^2}{6M^*}\,(1 + F_0')\,. \tag{5.10}$$

In Fig. 5.8 we plot $S_2(\rho)$ and associated uncertainties up to twice nuclear matter saturation density. We find the peculiar feature that the variations in the Landau parameter F_1 (which enters into the definition of the effective mass M^*) and in the Landau parameter F_0' are correlated in such a way as to produce a very small error band for the isospin-asymmetry energy up to nuclear saturation density. For instance, at nuclear matter saturation density, we obtain $30\,\mathrm{MeV} < S_2(\rho_0) < 32\,\mathrm{MeV}$, which is consistent with other recent microscopic uncertainty estimates [173, 172] but with a much smaller error band. It is not clear what could lead to the correlation between F_1 and F_0', and therefore we tentatively attribute the very small errors in $S_2(\rho)$ to a chance cancellation.

From Fig. 5.5 we see that G_0' remains large and positive for all densities considered. At nuclear saturation density, we find $1.2 < G_0' < 1.8$, which is consistent with extractions [178] from fitting

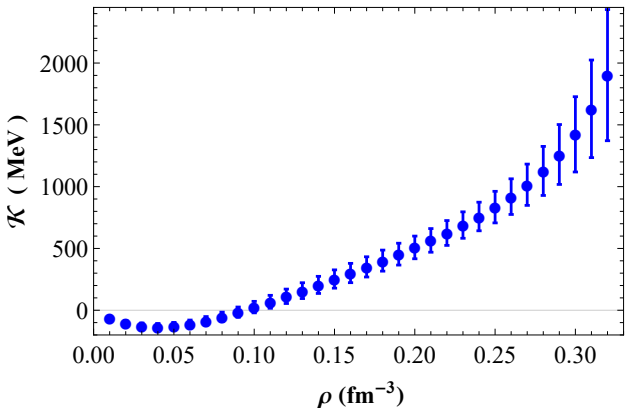

Figure 5.6: Incompressibility of symmetric nuclear matter as a function of the density for the two- and three-body chiral nuclear force models considered in the present work. Reprinted from [41].

the peak energy of giant Gamow-Teller resonances in heavy nuclei. Such fits give a range $1.4 < G_0' < 1.6$ [179] but rely on certain model assumptions related to the shape of the parametrized single-particle potential and the form of the effective interaction. In addition the authors of Ref. [179] find correlations between the value of G_1' and the position of the energy peak of the Gamow-Teller resonance when G_0' is kept fixed, leading to further uncertainties in the extraction of G_0' from resonance data.

Finally, we investigate the convergence of the Legendre polynomial decomposition, Eq. (5.3), for the noncentral components of the quasiparticle interaction. From Figs. 5.1–5.4 we see that in some cases the $L = 1$ Fermi liquid parameters are comparable in magnitude to the $L = 0$ parameters at nuclear matter saturation density. Using the tensor parametrizations in Eq. (5.2), it is expected [136] that the convergence is much improved compared to alternative choices, such as

$$H(\vec{p}_1, \vec{p}_2) S_{12}(\hat{q}) = \frac{q^2}{k_f^2} \tilde{H}(\vec{p}_1, \vec{p}_2) S_{12}(\hat{q}) \tag{5.11}$$

employed in Refs. [134, 158, 127]. In Fig. 5.9 we plot the ten lowest dimensionless Fermi liquid parameters from the n3lo450 potential at nuclear matter saturation density. It is clear that the slowest convergence is in the spin- and isospin-independent part of the quasiparticle interaction F,

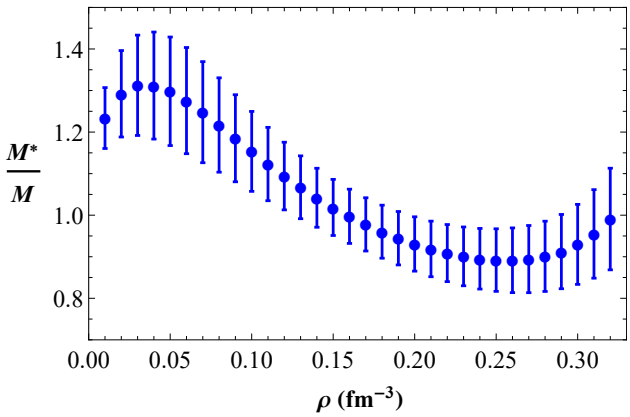

Figure 5.7: Nucleon effective mass in symmetric nuclear matter as a function of the density for the two- and three-body chiral nuclear force models considered in the present work. Reprinted from [41].

which even up to $L = 9$ has contributions greater than 0.1. The Legendre polynomial expansion in all other channels is nearly converged by $L = 5$

5.3 Conclusions and outlook

In the present work we have computed for the first time the full set of central and noncentral contributions to the quasiparticle interaction in symmetric nuclear matter up to twice nuclear saturation density. We have derived general formulas that allow one to extract the associated scalar functions from appropriate linear combinations of spin- and isospin-space matrix elements. Both two- and three-body forces are included at first- and second-order in perturbation theory, with the involved numerical calculations of the second-order diagrams benchmarked against model interactions. Three-body forces at the Hartree-Fock level are shown to give important contributions to the relative tensor and cross-vector interactions. Indeed, the isovector cross-vector interaction is dominated by three-body forces, in particular the two-pion exchange term proportional to the low-energy constant c_4, and only the second-order particle-hole diagram leads to a modest reduction of the strength in this channel. While the relative tensor force from the free-space nucleon-nucleon interaction is enhanced in the medium by three-body forces and second-order perturbative corrections, the center-of-mass tensor force remains relatively weak.

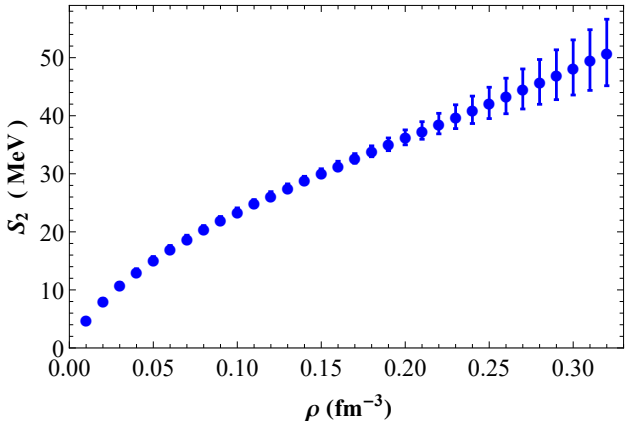

Figure 5.8: Isospin-asymmetry energy as a function of the density for the two- and three-body chiral nuclear force models considered in the present work. Reprinted from [41].

We have considered five different nuclear force models in order to estimate theoretical uncertainties. Up to nuclear saturation density, the relative tensor force in both the isoscalar and isovector channels is well constrained by microscopic many-body theory, which should be valuable for efforts to include effective tensor forces in mean-field modeling and density functional theory. In addition we find robust evidence for a strong isovector cross-vector interaction which is not normally included in mean-field models and may be important for spin-dependent phenomena. We benchmark the quality of our results against bulk nuclear matter properties, such as the incompressibility, isospin-asymmetry energy, and nucleon effective mass, which are directly related to selected central Fermi liquid parameters. While the theory uncertainties are sometimes large, in all cases the results are consistent with empirical constraints.

The present calculations are a step toward the microscopic description of response functions in nuclear matter consistent with equations of state exhibiting realistic nuclear saturation properties. In the future this work will be extended to isospin-asymmetric nuclear systems with applications to neutrino processes in neutron stars and supernovae.

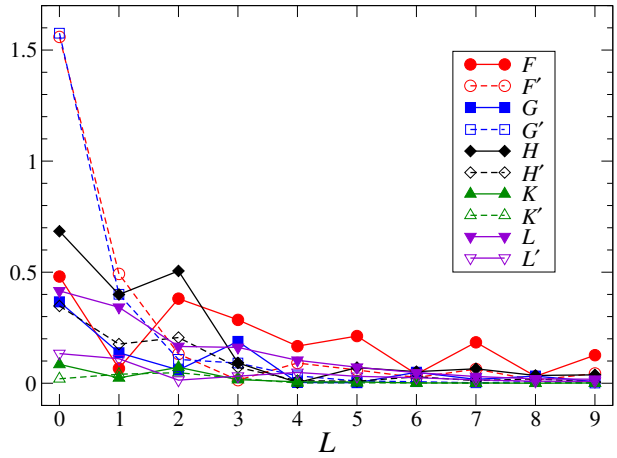

Figure 5.9: Convergence of the Legendre polynomial expansion for each of the different contributions to the quasiparticle interaction. Results are shown only for n3lo450 two- and three-body forces at nuclear matter saturation density. Terms up to $L = 9$ are considered. Reprinted from [41].

6. NUCLEON EFFECTIVE MASS

6.1 Introduction

The nucleon effective mass was first used to describe the dynamics of nucleons interacting with a momentum dependent potential by treating them as quasi-nucleons with an effective mass, M*, interacting with a potential independent of momentum. The effective mass can be thought of more generally as encoding the momentum and energy dependence of a single-particle potential. The nucleon effective mass is an important organizing concept in the theoretical description of dynamical and thermodynamical properties of nuclear many-body systems. In the context of nuclear astrophysics, the effective mass influences entropy generation in core-collapse supernovae [180] and the composition of the evolving matter [181], the strength of nuclear pairing in the neutron star inner crust and core [182, 183], superfluid entrainment [184] and its effect on pulsar glitches. In quantum many-body theory the effective mass is related to the momentum dependence of the nucleon single-particle energy and consequently to the density of states. Therefore, by examining nuclear level densities in the vicinity of the Fermi surface, the effective mass is inferred [185, 186] to lie close to that of a free nucleon $M^* \simeq M$. Below the Fermi surface, the distribution of deeply bound states implies a lower value of the effective mass on the order of $M^* \simeq 0.7M$ [187]. The effective mass above the Fermi surface can be deduced from the energy dependence of phenomenological nucleon-nucleus optical potentials, and again a value of $M^* \simeq 0.7M$ is needed for a consistent description of experimental data [4]. It is well known [5] that these general features are reproduced in microscopic calculations of the effective mass when second-order perturbative contributions to the nucleon self-energy are included.

In isospin-asymmetric nuclear matter, protons and neutrons will experience different single-particle potentials with different strengths and momentum dependences, the latter resulting in a splitting of the proton and neutron effective masses. In mean field theories [188, 189] this splitting is traditionally encoded through the isoscalar M_s^* and isovector M_v^* effective masses defined

according to

$$\frac{1}{M^*_{n,p}} = (1 \pm \delta_{np})\frac{1}{M^*_s} \mp \delta_{np}\frac{1}{M^*_v}, \tag{6.1}$$

where (-) is for neutron and (+) is for proton.

This parametrization is particularly convenient since the isoscalar and isovector effective masses depend only on the nucleon density. In addition, certain experimental observables, such as the nuclear electric dipole polarizability, are directly controlled by the isovector effective mass M^*_v. It is also common in the literature to consider the difference in neutron and proton effective masses as a function of density and isospin-asymmetry:

$$M^*_{n-p} = \frac{M^*_n - M^*_p}{M} \tag{6.2}$$

A global analysis [190] of experimental and theoretical predictions for the isospin-asymmetry energy $E_{sym}(\rho)$ and its slope $L(\rho)$ was used to extract the difference between the neutron and proton single-particle potentials with the conclusion that $M^*_{n-p}(\rho_0, \delta_{np}) \simeq 0.27\,\delta_{np}$. More recently, an investigation [191] of the isovector giant dipole resonance and isoscalar giant quadrupole resonance data for ^{208}Pb was used to deduce values for the isoscalar and isovector effective masses of $M^*_s(\rho_0) = (0.91 \pm 0.05)M$ and $M^*_v(\rho_0) = (0.80 \pm 0.03)M$, which implies a value $M^*_{n-p}(\rho_0, \delta_{np}) \simeq (0.27 \pm 0.15)\delta_{np}$, consistent with Ref. [190].

The above results, as well as microscopic many-body calculations [192, 193] with realistic nuclear force models, indicate that in isospin-asymmetric nuclear matter at saturation density, the neutron effective mass is larger than the proton effective mass. This is naturally explained by the properties of the nucleon-nucleon interaction, which at low momenta is more strongly attractive in the isospin-singlet $T = 0$ channel. In neutron-rich matter it is therefore expected that the proton single-particle potential will be deeper than the neutron single-particle potential. For momenta larger than the characteristic mass scale $m_\sigma \sim 550\,\text{MeV}$ associated with the intermediate-range attraction in the nucleon-nucleon potential, isovector interactions grow more strongly repulsive and eventually lead to an isospin inversion in the nuclear single-particle potential whereby a proton

experiences a more repulsive mean field potential than a neutron [192, 175]. This results in a stronger momentum dependence of the proton single-particle energy and consequently a smaller effective mass.

Recent heavy-ion collision data [194] for the relative yields of high-momentum protons and neutrons, however, appear to show a preference for $M^*_{n-p}(\rho_0) < 0$. Fast particle emission in the pre-equilibrium phase has been suggested [195, 196, 197] to be a particularly sensitive probe of the neutron-proton effective mass splitting, as lighter particles will experience greater acceleration and larger final momenta. The double ratio of neutron-to-proton yields from ^{124}Sn$-^{124}$Sn and ^{112}Sn$-^{112}$Sn reactions at beam energies of $E/A = 50, 120\,\text{MeV}$ were shown to be more consistent with transport simulations [197] employing the SLy4 Skyrme interaction (with $M^*_{n-p}(\rho_0) = -0.15\delta_{np}$) compared to the SkM* Skyrme interaction (with $M^*_{n-p}(\rho_0) = 0.30\delta_{np}$). This is a puzzle in light of the general theoretical arguments for $M^*_{n-p}(\rho_0) > 0$ described above, but additional experiments together with a broader range of mean field models and transport codes may shed further light on the issue.

In the present work we perform a systematic study of the neutron-proton effective mass splitting in neutron-rich matter from the perspective of chiral effective field theory. A central aim is to identify a range of energies for which the proton-neutron effective mass splitting is large, which may help guide future experimental investigations of this quantity in medium-energy heavy-ion collisions. We employ as a starting point realistic chiral two- and three-body forces from which we compute the proton and neutron self-energies in isospin-asymmetric nuclear matter and extract the associated effective masses. To assess theoretical uncertainties we consider chiral nucleon-nucleon potentials at next-to-next-to-leading order (N2LO) and N3LO, varying also the resolution scale.

6.2 Results

The effective mass is usually written as a product of terms that represent these dependences.

$$\frac{M^*}{M} = \frac{M^*_E}{M}\frac{M^*_k}{M} \tag{6.3}$$

where

$$\frac{M_k^*}{M} = \left(1 + \frac{M}{k}\frac{\partial U}{\partial k}\right)^{-1} \tag{6.4}$$

and

$$\frac{M_E^*}{M} = 1 - \frac{\partial U}{\partial E} \tag{6.5}$$

with U being the optical potential.

The nucleon effective mass calculated in nuclear matter from a set of five chiral interactions is shown in Fig. 6.1. The effective mass peaks at the Fermi momentum before flattening off to a value of 1 at high momentum.

The neutron-proton effective mass splitting is given by Eq. (6.2) and expressed in terms of the optical potential is given by

$$m_{n-p}^* = \frac{M\left(\frac{1}{k_f^p}\frac{dU_p}{dk}\Big|_{k_f^p} - \frac{1}{k_f^n}\frac{dU_n}{dk}\Big|_{k_f^n}\right)}{\left[1 + \frac{M}{k_f^p}\frac{dU_p}{dk}\Big|_{k_f^p}\right]\left[1 + \frac{M}{k_f^n}\frac{dU_n}{dk}\Big|_{k_f^n}\right]}. \tag{6.6}$$

The effective mass splitting is shown in Fig. 6.2. The dashed lines represent current phenomenological estimates of the effective mass splitting and the colored lines represent microscopic calculations of the effective mass splitting from a set of chiral interactions. The results from chiral EFT are not only within current phenomenological estimates [198], but predict a more narrow range of values.

6.3 Conclusions

In this ongoing work we aim to identify a range of energies for which the proton-neutron effective mass splitting is large by performing microscopic calculations of the nucleon effective mass in nuclear matter.

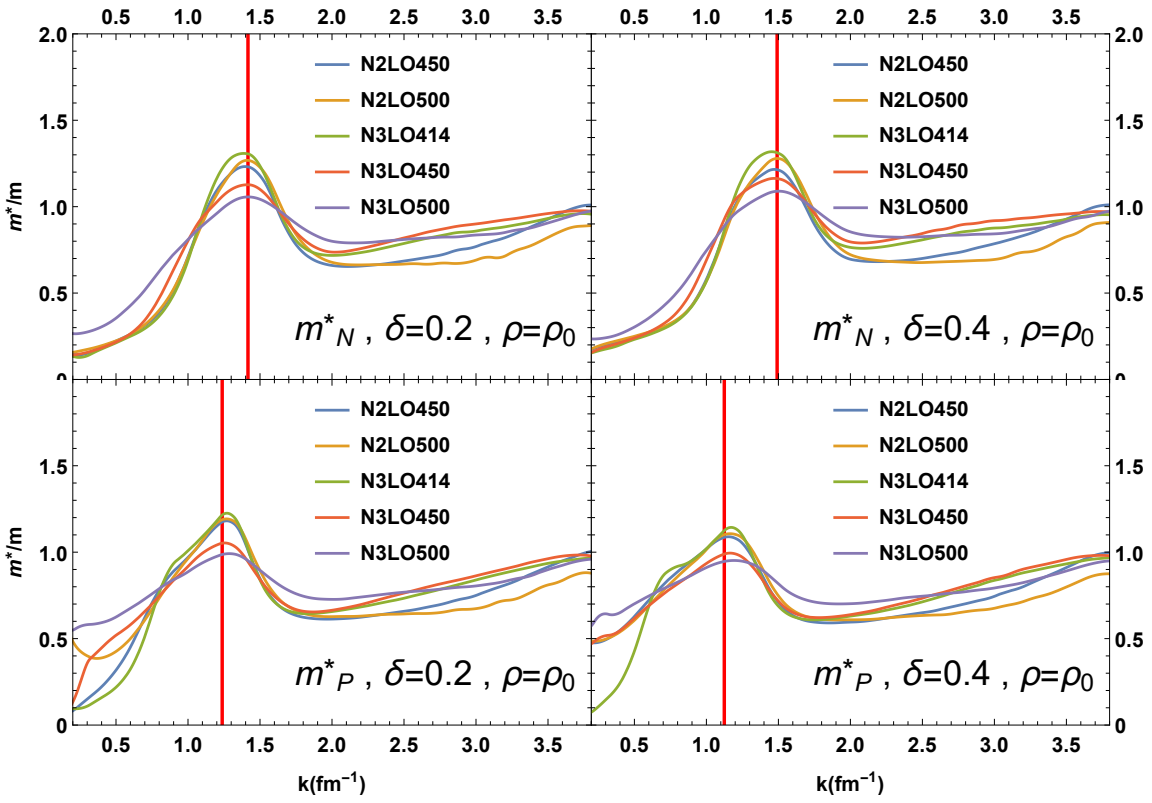

Figure 6.1: Nucleon effective mass at saturation density calculated from different chiral interactions plotted as a function of momentum. The neutron effective masses are shown on the top row and the proton effective masses are shown on the bottom row. The left column has an isospin asymmetry of 0.2 and the right column has an isospin asymmetry of 0.4. The Fermi momentum is shown by the red line.

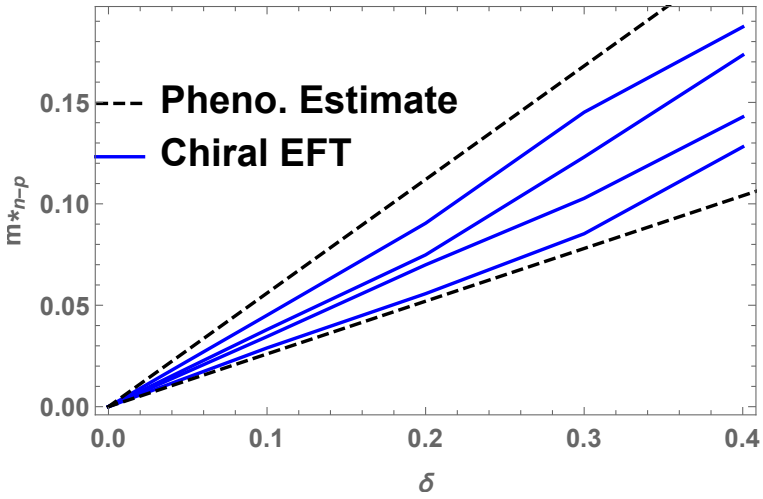

Figure 6.2: Neutron-proton effective mass splitting calculated from different chiral interactions (blue) plotted as a function of momentum. Current phenomenological estimates (dashed black).

7. SPECTRAL FUNCTION

The spectral function gives the probability of removing a nucleon with momentum in the single-particle state nlj from a nucleus A and the residual nucleus $A-1$ having an excitation energy E. The spectral function is given by

$$S_{nlj}(E) = \frac{1}{\pi} \frac{W_{nlj}(E)}{(E - E_{nlj})^2 + W_{nlj}(E)^2}, \tag{7.1}$$

where

$$W_{nlj}(E) = \int_0^\infty \bar{\Psi}^2_{nlj}(r) \frac{W(r,E)}{m^*(r,E)/m} dr, \tag{7.2}$$

and $W(r,E)$ is the imaginary term of the optical potential and $\Psi_{nlj}(r)$ is the wave function of the state.

7.1 Spectral Function from Dispersive Optical Potential

Dispersive optical potentials are constrained by the dispersion relation that links the imaginary and real terms, in addition to enforcing causality, to construct more realistic phenomenological optical potentials. In the dispersive approach, the optical potential has both real and imaginary terms $U(r,E) = V(r,E) + iW(r,E)$, however, the real term is written as a sum of Hartree-Fock and dispersive contributions:

$$V(r,E) = V_{HF}(r,E) + \Delta V(r,E). \tag{7.3}$$

The dispersive contribution is related to the imaginary term according to the dispersion relation which is given by

$$\Delta V(r,E) = \frac{P}{\pi} \int_{-\infty}^{\infty} \frac{W(r,E)}{E' - E} dE', \tag{7.4}$$

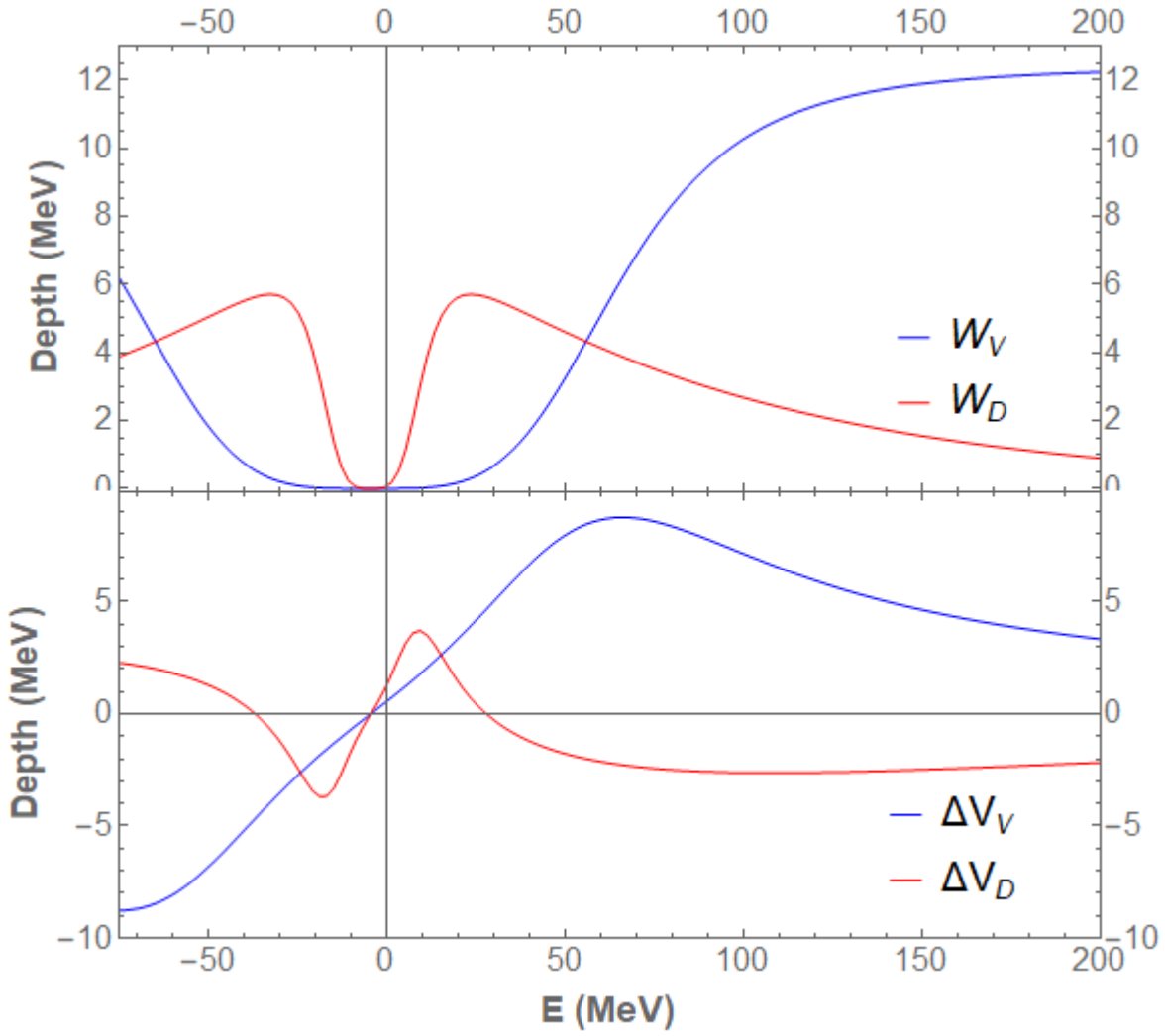

Figure 7.1: Shown in the top plot are the volume and surface imaginary terms from a dispersive optical potential, with their real counterparts shown in the bottom plot.

where one can see that knowledge of the imaginary part is needed along the entire energy domain. In practice [199, 200] the imaginary term is assumed to be symmetric about the Fermi energy, leading to the dispersive contributions to the real term to be skew-symmetric as seen in Fig. 7.1. The imaginary term is typically determined from a traditional phenomenological approach that involves an optimization of the model parameters to best reproduce scattering data. Once the imaginary term is determined, the dispersive contribution to the real term follows from the dispersion relation, leaving only the Hartree-Fock contribution to the real term. The Hartree-Fock

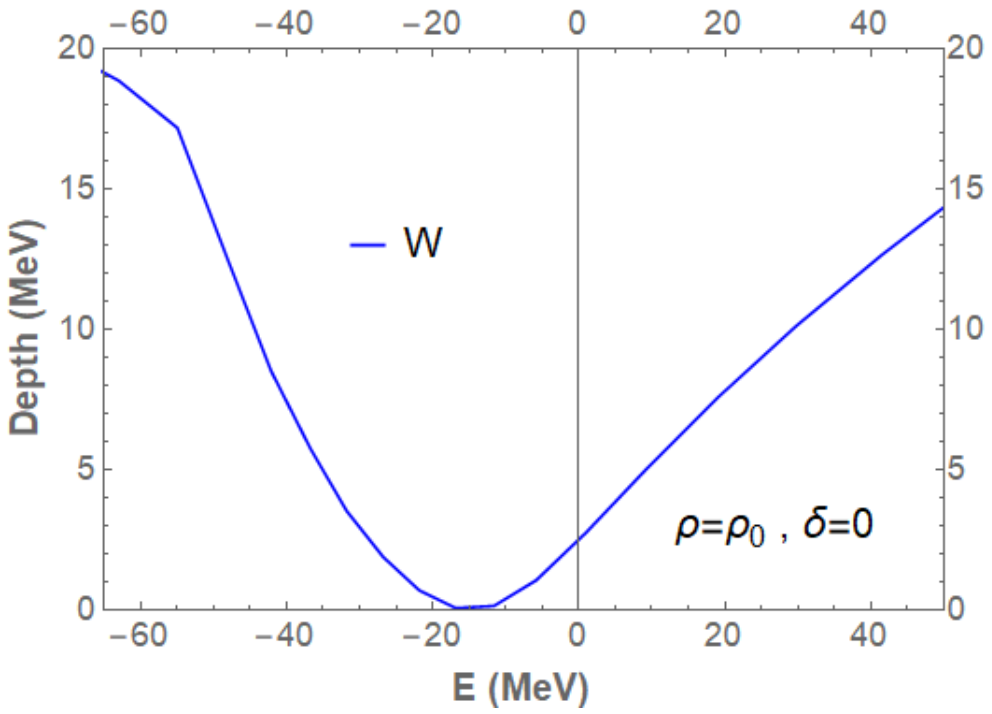

Figure 7.2: Energy dependence of the imaginary depth of the microscopic opitcal potential shown to be symmetric about the Fermi energy, which is ≈ -17 MeV for symmetric nuclear matter.

term is then fit to both scattering data and bound-state energies with the assumption of linear energy dependence for negative energies. This consistent treatment of positive and negative energy states is a clear advantage of the dispersive approach compared to traditional methods.

7.2 Spectral Function from Microscopic Optical Potential

As a first step we aim to test the assumptions of the dispersive optical potential analysis in our microscopic framework. One of the key assumptions needed to compute the integral in the dispersion relation is the symmetry in the energy dependence of the imaginary strength, since there are few empirical constraints of the imaginary term in the negative energy regime. In Fig. 7.2 we show the depth of the imaginary term plotted as a function of energy, and an approximate symmetry about the Fermi energy is exhibited.

The next key assumption of the dispersive optical potential approach is the linear energy dependence of the Hartree-Fock contribution for negative energies. In Fig. 7.3 , we show that this is

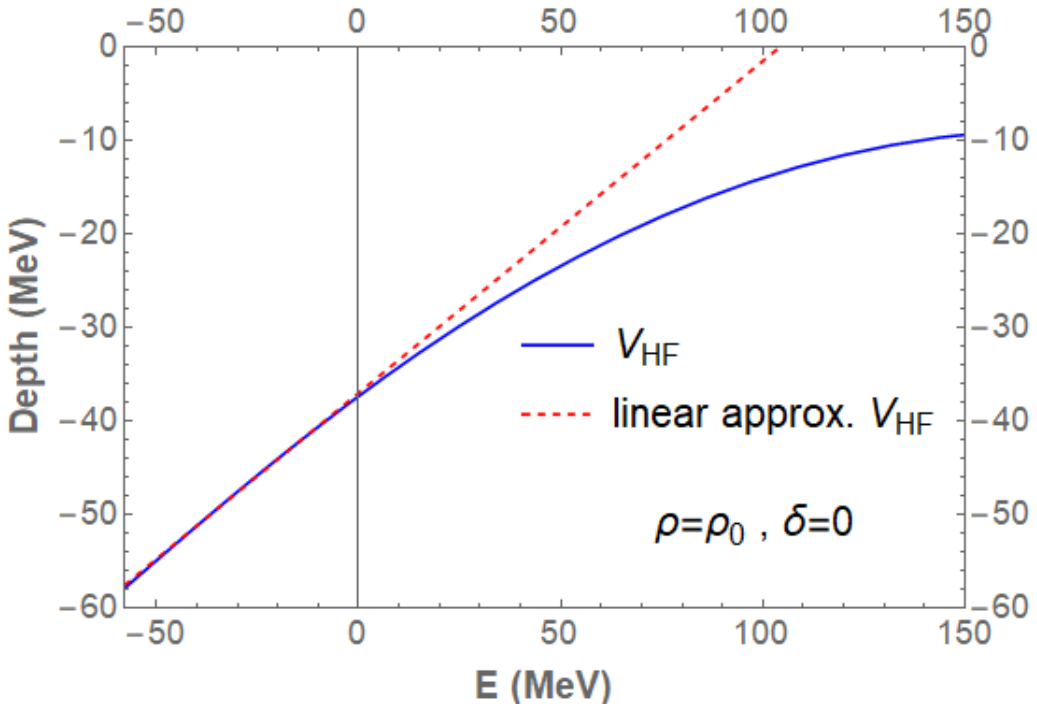

Figure 7.3: The Hartree-Fock contribution to the microscopic optical potential from chiral EFT.

an excellent approximation of our microscopic calculations of the Hartree-Fock contributions.

An additional approximation employed by many dispersive optical potential analyses is the energy independence of geometry parameters, in addition to assuming that real and imaginary volume parameters are equivalent. In [201], it is shown in great detail that neither of these assumptions hold in general.

In Fig. 7.4 spectral functions for ^{40}Ca calculated from microscopic optical potentials are plotted as a function of energy. Compared to phenomenological studies, the energies for states near the Fermi energy are in reasonable agreement.

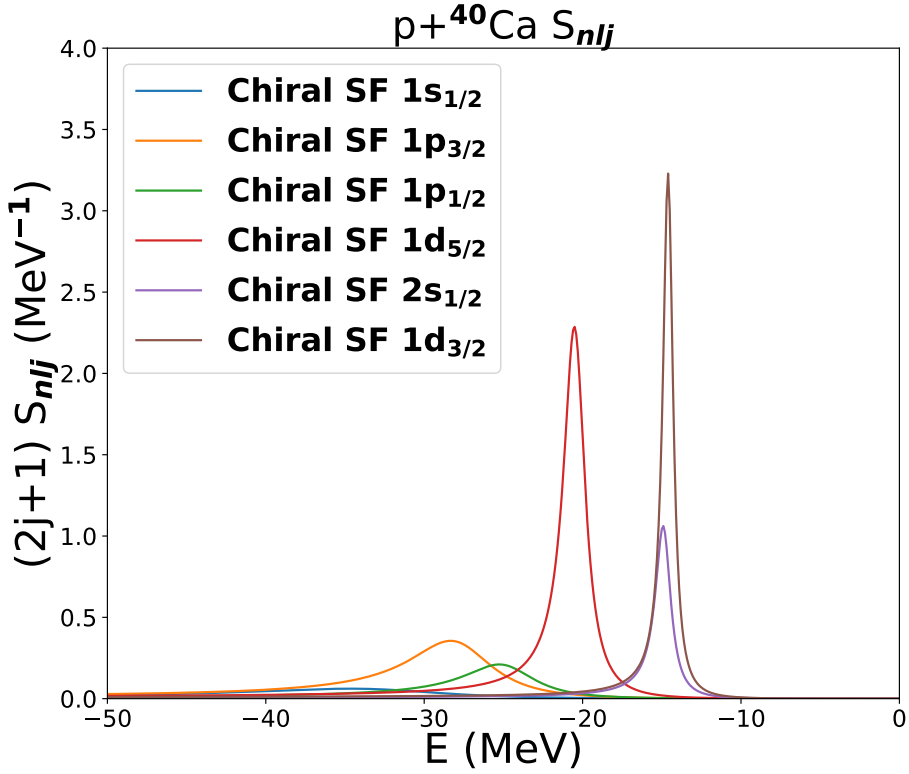

Figure 7.4: Nucleon spectral functions for bound states in ^{40}Ca from chiral effective field theory.

8. CONCLUSIONS AND OUTLOOK

I have developed microscopic nucleon-nucleus optical potentials based on chiral nuclear forces, calculated through many-body perturbation theory. My work extended results for the nucleon optical potential in nuclear matter to optical potentials for nucleons interacting with nuclei and ultimately to a global nucleon-nucleus optical potential suitable for exotic isotopes. This global optical potential yields good results in preliminary benchmarks to elastic scattering data. In addition to satisfactorily reproducing scattering data, comparisons to state-of-the-art phenomenological global optical potentials revealed inadequacies in their isovector terms. As rare isotope beam facilities begin to perform experiments on increasingly neutron-rich isotopes, knowledge of the isovector terms of the optical potential will be crucial for making realistic theoretical predictions of these reactions.

There are many avenues for continuing this line of research. Among those are several ways of improving the microscopic calculations. For example, the density matrix expansion calculated at the Hartree-Fock level is known [48, 63] to produce a stronger spin-orbit interaction than is required from traditional mean field theory studies of finite nuclei by about 20-50%. The inclusion of multi-pion-exchange processes has been shown [64] to reduce the strength of the one-body spin-orbit interaction in finite nuclei. In future works we intend to account for these processes by including G-matrix correlations in the density matrix expansion as outlined in Ref. [56]. Additionally in future work we plan to implement next-to-next-to-next-to-leading order (N3LO) three-body forces [35, 36, 37, 78, 79, 80] as well as a wider class of chiral potentials [117, 202] to better assess the theoretical uncertainties.

Separate from improvements to the calculations, there are several topics that are very natural applications for these microscopic optical potentials. In the future we plan to compute neutron-capture cross sections on exotic isotopes and more thoroughly explore theoretical uncertainties [117, 202] associated with the isovector part of the nuclear optical potential. This microscopic global optical potential may also be used as a base in the construction of a new phenomenological

global optical in a Bayesian framework. New phenomenological optical potentials based on microscopic physics with incorporated uncertainty estimates will surely be a very important contribution to the future study of nuclear reactions.

REFERENCES

[1] A. Idini, C. Barbieri, and P. Navrátil *Phys. Rev. Lett.*, vol. 123, p. 092501, Aug 2019.

[2] R. Machleidt and D. R. Entem, "Chiral effective field theory and nuclear forces," *Phys. Rep.*, vol. 503, no. 1, pp. 1 – 75, 2011.

[3] R. L. Varner, W. J. Thompson, T. L. McAbee, E. J. Ludwig, and T. B. Clegg, "A global nucleon optical model potential," *Phys. Rep.*, vol. 201, no. 2, pp. 57 – 119, 1991.

[4] A. J. Koning and J. P. Delaroche, "Local and global nucleon optical models from 1 kev to 200 MeV," *Nucl. Phys. A*, vol. 713, no. 3, pp. 231 – 310, 2003.

[5] J. P. Jeukenne, A. Lejeune, and C. Mahaux, "Many-body theory of nuclear matter," *Phys. Rep.*, vol. 25, no. 2, pp. 83 – 174, 1976.

[6] A. Lejeune and P. E. Hodgson, "Microscopic optical model analyses of proton and neutron elastic scattering cross sections," *Nucl. Phys. A*, vol. 295, no. 2, pp. 301 – 308, 1978.

[7] L. F. Hansen, F. S. Dietrich, B. A. Pohl, C. H. Poppe, and C. Wong, "Test of microscopic optical model potentials for neutron elastic scattering at 14.6 MeV over a wide mass range," *Phys. Rev. C*, vol. 31, pp. 111–119, Jan 1985.

[8] J. S. Petler, M. S. Islam, R. W. Finlay, and F. S. Dietrich, "Microscopic optical model analysis of nucleon scattering from light nuclei," *Phys. Rev.*, vol. C32, pp. 673–684, 1985.

[9] E. Bauge, J. P. Delaroche, and M. Girod *Phys. Rev. C*, vol. 58, pp. 1118–1145, Aug 1998.

[10] J. W. Holt, N. Kaiser, G. A. Miller, and W. Weise, "Microscopic optical potential from chiral nuclear forces," *Phys. Rev. C*, vol. 88, p. 024614, Aug 2013.

[11] M. Toyokawa, K. Minomo, M. Kohno, and M. Yahiro, "Roles of chiral three-nucleon forces in nucleon–nucleus scattering," *J. Phys. G*, vol. 42, no. 2, p. 025104, 2015.

[12] J. W. Holt, N. Kaiser, and G. A. Miller, "Microscopic optical potential for exotic isotopes from chiral effective field theory," *Phys. Rev. C*, vol. 93, p. 064603, Jun 2016.

[13] H. S. Camarda, F. S. Dietrich, and T. W. Phillips *Phys. Rev. C*, vol. 39, p. 1725, 1989.

[14] E. Bauge, J. P. Delaroche, and M. Girod *Phys. Rev. C*, vol. 63, p. 024607, 2001.

[15] A. K. Kerman, H. McManus, and R. Thaler *Ann. Phys. (N.Y.)*, vol. 8, p. 551, 1959.

[16] F. A. Brieva and J. R. Rook, "Nucleon-nucleus optical model potential: (1). nuclear matter approach," *Nucl. Phys. A*, vol. 291, no. 2, pp. 299 – 316, 1977.

[17] L. Ray and G. W. Hoffmann, "Relativistic and nonrelativistic impulse approximation descriptions of 300–1000 MeV proton + nucleus elastic scattering," *Phys. Rev. C*, vol. 31, pp. 538–560, Feb 1985.

[18] C. Elster, T. Cheon, E. F. Redish, and P. C. Tandy, "Full-folding optical potentials in elastic proton-nucleus scattering," *Phys. Rev. C*, vol. 41, pp. 814–827, Mar 1990.

[19] H. F. Arellano, F. A. Brieva, and W. G. Love, "Nonrelativistic full-folding model of nucleon elastic scattering at intermediate energies," *Phys. Rev. C*, vol. 41, pp. 2188–2201, May 1990.

[20] H. F. Arellano, F. A. Brieva, and W. G. Love *Phys. Rev. C*, vol. 52, p. 301, 1995.

[21] M. Vorabbi, P. Finelli, and C. Giusti *Phys. Rev. C*, vol. 93, p. 034619, 2016.

[22] M. Vorabbi, P. Finelli, and C. Giusti, "Proton-Nucleus Elastic Scattering: Comparison between Phenomenological and Microscopic Optical Potentials," 2018.

[23] C. R. Chinn, C. Elster, and R. M. Thaler *Phys. Rev. C*, vol. 48, p. 2956, 1993.

[24] R. Crespo, R. C. Johnson, and J. A. Tostevin *Phys. Rev. C*, vol. 48, p. 351, 1993.

[25] S. J. Waldecker, C. Barbieri, and W. H. Dickhoff *Phys. Rev. C*, vol. 84, p. 034616, 2011.

[26] R. J. Charity, J. M. Mueller, L. G. Sobotka, and W. H. Dickhoff, "Dispersive-optical-model analysis of the asymmetry dependence of correlations in Ca isotopes," *Phys. Rev. C*, vol. 76, p. 044314, Oct 2007.

[27] K. Egashira, K. Minomo, M. Toyokawa, T. Matsumoto, and M. Yahiro, "Microscopic optical potentials for He4 scattering," *prc*, vol. 89, p. 064611, June 2014.

[28] J. Rotureau, P. Danielewicz, G. Hagen, G. R. Jansen, and F. M. Nunes, "Microscopic optical potentials for Calcium isotopes," 2018.

[29] J. Rotureau, P. Danielewicz, G. Hagen, F. M. Nunes, and T. Papenbrock, "Optical potential from first principles," *Phys. Rev. C*, vol. 95, p. 024315, Feb 2017.

[30] M. Toyokawa, M. Yahiro, T. Matsumoto, K. Minomo, K. Ogata, and M. Kohno *Phys. Rev. C*, vol. 92, p. 024618, Aug 2015.

[31] V. Durant, P. Capel, L. Huth, A. Balantekin, and A. Schwenk, "Double-folding potentials from chiral effective field theory," *Phys. Lett. B*, vol. 782, pp. 668 – 674, 2018.

[32] S. Weinberg, "Phenomenological lagrangians," *Physica A*, vol. 96, no. 1, pp. 327 – 340, 1979.

[33] E. Epelbaum, H.-W. Hammer, and U.-G. Messner *Rev. Mod. Phys.*, vol. 81, p. 1773, 2009.

[34] A. J. Koning, S. Hilaire, and M. C. Duijvestijn, "Talys-1.0," *Proc. of the Int. Conf. on Nucl. Data for Science and Technology, EDP Sciences*, 2008.

[35] I. Tews, T. Krüger, K. Hebeler, and A. Schwenk *Phys. Rev. Lett.*, vol. 110, p. 032504, 2013.

[36] C. Drischler, A. Carbone, K. Hebeler, and A. Schwenk *Phys. Rev. C*, vol. 94, no. 5, p. 054307, 2016.

[37] N. Kaiser and V. Niessner *Phys. Rev. C*, vol. 98, p. 054002, Nov 2018.

[38] L. Coraggio, J. W. Holt, N. Itaco, R. Machleidt, L. E. Marcucci, and F. Sammarruca *Phys. Rev. C*, vol. 89, p. 044321, 2014.

[39] C. Wellenhofer, J. W. Holt, N. Kaiser, and W. Weise *Phys. Rev. C*, vol. 89, p. 064009, 2014.

[40] C. Wellenhofer, J. W. Holt, and N. Kaiser *Phys. Rev. C*, vol. 92, p. 015801, 2015.

[41] J. W. Holt, N. Kaiser, and T. R. Whitehead, "Tensor fermi liquid parameters in nuclear matter from chiral effective field theory," *Phys. Rev. C*, vol. 97, p. 054325, May 2018.

[42] J. S. Bell and E. J. Squires, "A formal optical model," *Phys. Rev. Lett.*, vol. 3, pp. 96–97, Jul 1959.

[43] Y. Lim and J. W. Holt, "Structure of neutron star crusts from new skyrme effective interactions constrained by chiral effective field theory," *Phys. Rev. C*, vol. 95, p. 065805, Jun 2017.

[44] J. P. Jeukenne, A. Lejeune, and C. Mahaux, "Optical-model potential in finite nuclei from reid's hard core interaction," *Phys. Rev. C*, vol. 16, pp. 80–96, Jul 1977.

[45] S. Kosugi and H. Yoshida, "On the energy dependence of the imaginary optical-model potential for proton scattering from 40 Ca," *Nucl. Phys.*, vol. A373, pp. 349–362, 1982.

[46] S. K. Bogner, R. J. Furnstahl, and L. Platter *Eur. Phys. J. A*, vol. 39, pp. 219–241, 2009.

[47] B. Gebremariam, T. Duguet, and S. K. Bogner *Phys. Rev. C*, vol. 82, p. 014305, 2010.

[48] J. W. Holt, N. Kaiser, and W. Weise, "Microscopic optical potential for exotic isotopes from chiral effective field theory," *Eur. Phys. J. A*, vol. 47, 2011.

[49] J. W. Negele and D. Vautherin *Phys. Rev. C*, vol. 5, p. 1472, 1972.

[50] S. K. Bogner, A. Schwenk, R. J. Furnstahl, and A. Nogga *Nucl. Phys. A*, vol. 763, p. 59, 2005.

[51] J. W. Holt, N. Kaiser, and W. Weise *Phys. Rev. C*, vol. 79, p. 054331, May 2009.

[52] K. Hebeler and A. Schwenk *Phys. Rev. C*, vol. 82, p. 014314, 2010.

[53] J. W. Negele and K. Yazaki, "Mean free path in a nucleus," *Phys. Rev. Lett.*, vol. 47, pp. 71–74, Jul 1981.

[54] S. Fantoni, B. L. Friman, and V. R. Pandharipande *Phys. Lett.*, vol. B104, pp. 89–91, 1981.

[55] B. Gebremariam, S. K. Bogner, and T. Duguet *Nucl. Phys. A*, vol. 851, pp. 17–43, 2011.

[56] Y. N. Zhang, S. K. Bogner, and R. J. Furnstahl *Phys. Rev. C*, vol. 98, p. 064306, 2018.

[57] N. Kaiser *Eur. Phys. J. A*, vol. 48, p. 36, 2012.

[58] F. A. Brieva and J. R. Rook, "Nucleon-nucleus optical model potential: (ii). finite nuclei," *Nucl. Phys. A*, vol. 291, no. 2, pp. 317 – 341, 1977.

[59] R. B. Wiringa, V. G. J. Stoks, and R. Schiavilla, "Accurate nucleon-nucleon potential with charge-independence breaking," *Phys. Rev. C*, vol. 51, pp. 38–51, Jan 1995.

[60] C. Lagrange and A. Lejeune, "Phenomenological and microscopic optical model analyses of the interaction of low-energy nucleons with Nb-93," *Phys. Rev.*, vol. C25, pp. 2278–2291, 1982.

[61] M. Kohno, D. W. L. Sprung, S. Nagata, and N. Yamaguchi, "Incident energy dependence of the effective interaction and radius of the optical model potential," *Phys. Lett.*, vol. 137B, pp. 10–14, 1984.

[62] S. Goriely and J.-P. Delaroche *Phys. Lett.*, vol. B653, p. 178, 2007.

[63] J. W. Holt, M. Rho, and W. Weise *Phys. Rept.*, vol. 621, p. 2, 2016.

[64] N. Kaiser and W. Weise *Nucl. Phys. A*, vol. 836, p. 256, 2010.

[65] F. A. Brieva and J. R. Rook, "Nucleon-nucleus optical model potential: (iii). the spin-orbit component," *Nucl. Phys. A*, vol. 297, no. 2, pp. 206 – 230, 1978.

[66] R. H. McCamis, T. N. Nasr, J. Birchall, N. E. Davison, W. T. H. van Oers, P. J. T. Verheijen, R. F. Carlson, A. J. Cox, B. C. Clark, E. D. Cooper, S. Hama, and R. L. Mercer, "Elastic scattering of protons from 40,42,44,48Ca from 20 to 50 MeV and nuclear matter radii," *Phys. Rev. C*, vol. 33, pp. 1624–1633, May 1986.

[67] K. Yagi, H. Ejiri, M. Furukawa, Y. Ishizaki, M. Koike, K. Matsuda, Y. Nakajima, I. Nonaka, Y. Saji, E. Tanaka, and G. Satchler, "Excitation of low-lying levels in Ca40 by (p , p') scattering at ep = 55 MeV," *Phys. Lett.*, vol. 10, no. 2, pp. 186 – 191, 1964.

[68] H. Sakaguchi, M. Nakamura, K. Hatanaka, A. Goto, T. Noro, F. Ohtani, H. Sakamoto, and S. Kobayashi, "65 MeV polarized proton elastic scattering and the effective two-body interaction range," *Phys. Lett. B*, vol. 89, no. 1, pp. 40 – 43, 1979.

[69] A. Nadasen, P. Schwandt, P. P. Singh, W. W. Jacobs, A. D. Bacher, P. T. Debevec, M. D. Kaitchuck, and J. T. Meek, "Elastic scattering of 80-180 MeV protons and the proton-nucleus optical potential," *Phys. Rev. C*, vol. 23, pp. 1023–1043, Mar 1981.

[70] E. Koltay, L. Meskó, and L. Végh, "Levels of 41Sc from the 40Ca(p, p)40Ca reaction," *Nucl. Phys. A*, vol. 249, no. 1, pp. 173 – 181, 1975.

[71] A. Auce, A. Ingemarsson, R. Johansson, M. Lantz, G. Tibell, R. F. Carlson, M. J. Shachno, A. A. Cowley, G. C. Hillhouse, N. M. Jacobs, J. A. Stander, J. J. v. Zyl, S. V. Förtsch, J. J. Lawrie, F. D. Smit, and G. F. Steyn *Phys. Rev. C*, vol. 71, p. 064606, Jun 2005.

[72] J. F. Dicello and G. Igo, "Proton total reaction cross sections in the 10-20-MeV range: Calcium-40 and Carbon-12," *Phys. Rev. C*, vol. 2, pp. 488–499, Aug 1970.

[73] R. F. Carlson, A. J. Cox, J. R. Nimmo, N. E. Davison, S. A. Elbakr, J. L. Horton, A. Houdayer, A. M. Sourkes, W. T. H. van Oers, and D. J. Margaziotis *Phys. Rev. C*, vol. 12, pp. 1167–1175, Oct 1975.

[74] R. F. Carlson, A. J. Cox, N. E. Davison, T. Eliyakut-Roshko, R. H. McCamis, and W. T. H. van Oers *Phys. Rev. C*, vol. 49, pp. 3090–3097, Jun 1994.

[75] M. R. Mumpower, R. Surman, G. C. McLaughlin, and A. Aprahamian *Prog. Part. Nucl. Phys.*, vol. 86, pp. 86–126, 2016.

[76] F. J. Fattoyev, J. Piekarewicz, and C. J. Horowitz, "Neutron skins and neutron stars in the multimessenger era," *Phys. Rev. Lett.*, vol. 120, p. 172702, Apr 2018.

[77] T. R. Whitehead, Y. Lim, and J. W. Holt *Phys. Rev. C*, vol. 100, p. 014601, Jul 2019.

[78] N. Kaiser and B. Singh, "Density-dependent NN interaction from subleading chiral three-nucleon forces: Long-range terms," *Phys. Rev. C*, vol. 100, p. 014002, 2019.

[79] C. Drischler, K. Hebeler, and A. Schwenk, "Chiral interactions up to next-to-next-to-next-to-leading order and nuclear saturation," *Phys. Rev. Lett.*, vol. 122, p. 042501, 2019.

[80] J. W. Holt, M. Kawaguchi, and N. Kaiser, "Implementing chiral three-body forces in terms of medium-dependent two-body forces," 2020.

[81] H. D. Vries, C. D. Jager, and C. D. Vries, "Nuclear charge-density-distribution parameters from elastic electron scattering," *At. Data Nucl. Data Tables*, vol. 36, no. 3, pp. 495 – 536, 1987.

[82] S. F. Hicks, S. E. Hicks, G. R. Shen, and M. T. McEllistrem *Phys. Rev. C*, vol. 41, pp. 2560–2570, Jun 1990.

[83] J. M. Mueller, R. J. Charity, R. Shane, L. G. Sobotka, S. J. Waldecker, W. H. Dickhoff, A. S. Crowell, J. H. Esterline, B. Fallin, C. R. Howell, C. Westerfeldt, M. Youngs, B. J. Crowe, and R. S. Pedroni *Phys. Rev. C*, vol. 83, p. 064605, Jun 2011.

[84] E. L. Hjort, F. P. Brady, J. L. Romero, J. R. Drummond, D. S. Sorenson, J. H. Osborne, B. McEachern, and L. F. Hansen *Phys. Rev. C*, vol. 50, pp. 275–281, Jul 1994.

[85] R. Alarcon, J. Rapaport, and R. Finlay, "Nucleon elastic scattering from 40Ca between 11 and 48 MeV," *Nucl. Phys. A*, vol. 462, no. 3, pp. 413 – 444, 1987.

[86] R. P. DeVito, S. M. Austin, W. Sterrenburg, and U. E. P. Berg *Phys. Rev. Lett.*, vol. 47, pp. 628–631, Aug 1981.

[87] J. D. Reber and J. D. Brandenberger *Phys. Rev.*, vol. 163, pp. 1077–1083, Nov 1967.

[88] J. H. Osborne, F. P. Brady, J. L. Romero, J. L. Ullmann, D. S. Sorenson, A. Ling, N. S. P. King, R. C. Haight, J. Rapaport, R. W. Finlay, E. Bauge, J. P. Delaroche, and A. J. Koning *Phys. Rev. C*, vol. 70, p. 054613, Nov 2004.

[89] G. M. Honoré, W. Tornow, C. R. Howell, R. S. Pedroni, R. C. Byrd, R. L. Walter, and J. P. Delaroche *Phys. Rev. C*, vol. 33, pp. 1129–1140, Apr 1986.

[90] W. Tornow, E. Woye, G. Mack, C. Floyd, K. Murphy, P. Guss, S. Wender, R. Byrd, R. Walter, T. Clegg, and H. Leeb *Nucl. Phys.*, vol. A385, p. 373, 1982.

[91] R. Becker, W. Guindon, and G. Smith *Nucl. Phys.*, vol. 89, p. 154, 1966.

[92] R. Shane, R. Charity, J. Elson, L. Sobotka, M. Devlin, N. Fotiades, and J. O'Donnell *Nucl. Instrum. Methods Phys. Res.*, vol. A614, p. 468, 2010.

[93] C. J. Horowitz, A. Arcones, B. Cote, I. Dillmann, W. Nazarewicz, I. U. Roederer, H. Schatz, A. Aprahamian, D. Atanasov, A. Bauswein, T. C. Beers, J. Bliss, M. Brodeur, J. A. Clark, A. Frebel, F. Foucart, C. J. Hansen, O. Just, A. Kankainen, G. C. McLaughlin, J. M. Kelly, S. N. Liddick, D. M. Lee, J. Lippuner, D. Martin, J. Mendoza-Temis, B. D. Metzger, M. R. Mumpower, G. Perdikakis, J. Pereira, B. W. O'Shea, R. Reifarth, A. M. Rogers, D. M. Siegel, A. Spyrou, R. Surman, X. Tang, T. Uesaka, and M. Wang *J. Phys. G: Nucl. Part. Phys.*, vol. 46, p. 083001, 2019.

[94] L. Nilsson, M. Drosg, D. M. Drake, and A. Lindholm *Phys. Rev. C*, vol. 21, pp. 902–905, Mar 1980.

[95] R. W. Finlay, W. P. Abfalterer, G. Fink, E. Montei, T. Adami, P. W. Lisowski, G. L. Morgan, and R. C. Haight, "Neutron total cross sections at intermediate energies," *Phys. Rev. C*, vol. 47, pp. 237–247, Jan 1993.

[96] A. B. Balantekin, J. Carlson, D. J. Dean, G. M. Fuller, R. J. Furnstahl, M. Hjorth-Jensen, R. V. F. Janssens, B.-A. Li, W. Nazarewicz, F. M. Nunes, W. E. Ormand, S. Reddy, and B. M. Sherrill, "Nuclear theory and science of the facility for rare isotope beams," *Mod. Phys. Lett. A*, vol. 29, no. 11, p. 1430010, 2014.

[97] B. C, C. L. Fryer, K. Belczynski, O. Korobkin, M. Chruska, N. Vassh, M. R. Mumpower, J. Lippuner, T. M. Sprouse, R. Surman, and R. Wollaeger, "The origin of r-process elements in the milky way," *Astrophys. J.*, vol. 855, p. 99, mar 2018.

[98] D. Kasen, B. Metzger, J. Barnes, E. Quataert, and E. Ramirez-Ruiz, "Origin of the heavy elements in binary neutron-star mergers from a gravitational-wave event," *Nature*, vol. 551, pp. 80–84, Nov 2017.

[99] B. A. Brown, "Mirror charge radii and the neutron equation of state," *Phys. Rev. Lett.*, vol. 119, p. 122502, Sep 2017.

[100] F. G. Perey, "Optical-model analysis of proton elastic scattering in the range of 9 to 22 MeV," *Phys. Rev.*, vol. 131, pp. 745–763, Jul 1963.

[101] M. Catacora-Rios, G. B. King, A. E. Lovell, and F. M. Nunes, "Exploring experimental conditions to reduce uncertainties in the optical potential," *Phys. Rev. C*, vol. 100, p. 064615, Dec 2019.

[102] G. B. King, A. E. Lovell, L. Neufcourt, and F. M. Nunes, "Direct comparison between bayesian and frequentist uncertainty quantification for nuclear reactions," *Phys. Rev. Lett.*, vol. 122, p. 232502, Jun 2019.

[103] T. R. Whitehead, Y. Lim, and J. W. Holt, "Neutron elastic scattering on calcium isotopes from chiral nuclear optical potentials," *Phys. Rev. C*, vol. 101, p. 064613, Jun 2020.

[104] F. D. Becchetti and G. W. Greenlees, "Nucleon-nucleus optical-model parameters, A40e50 MeV," *Phys. Rev.*, vol. 182, pp. 1190–1209, Jun 1969.

[105] D. Wilmore and P. Hodgson, "The calculation of neutron cross-sections from optical potentials," *Nucl. Phys.*, vol. 55, pp. 673 – 694, 1964.

[106] S. P. Weppner, R. B. Penney, G. W. Diffendale, and G. Vittorini, "Isospin dependent global nucleon-nucleus optical model at intermediate energies," *Phys. Rev. C*, vol. 80, p. 034608, Sep 2009.

[107] J. Rapaport, V. Kulkarni, and R. W. Finlay, "A global optical-model analysis of neutron elastic scattering data," *Nucl. Phys. A*, vol. 330, no. 1, pp. 15 – 28, 1979.

[108] X.-H. Li and L.-W. Chen, "Isospin dependent global neutron–nucleus optical model potential," *Nucl. Phys. A*, vol. 874, pp. 62 – 80, 2012.

[109] X. Li and C. Cai, "Global dispersive optical model potential for proton as projectile in the energy region up to 200 MeV," *Nucl. Phys. A*, vol. 801, no. 1, pp. 43 – 67, 2008.

[110] T. Furumoto, K. Tsubakihara, S. Ebata, and W. Horiuchi, "Microscopic global optical potential for nucleon-nucleus systems in the energy range 50–400 MeV," *Phys. Rev. C*, vol. 99, p. 034605, Mar 2019.

[111] R. Xu, Z. Ma, Y. Zhang, Y. Tian, E. N. E. van Dalen, and H. Müther, "Global analysis of isospin dependent microscopic nucleon-nucleus optical potentials in a dirac-brueckner-hartree-fock approach," *Phys. Rev. C*, vol. 94, p. 034606, Sep 2016.

[112] M. R. Mumpower, R. Surman, G. C. McLaughlin, and A. Aprahamian, "The impact of individual nuclear properties on r-process nucleosynthesis," *Prog. Part. Nucl. Phys.*, vol. 86, pp. 86 – 126, 2016.

[113] A. Spyrou, S. N. Liddick, A. C. Larsen, M. Guttormsen, K. Cooper, A. C. Dombos, D. J. Morrissey, F. Naqvi, G. Perdikakis, S. J. Quinn, T. Renstrøm, J. A. Rodriguez, A. Simon, C. S. Sumithrarachchi, and R. G. T. Zegers *Phys. Rev. Lett.*, vol. 113, p. 232502, Dec 2014.

[114] S. N. Liddick, A. Spyrou, B. P. Crider, F. Naqvi, A. C. Larsen, M. Guttormsen, M. Mumpower, R. Surman, G. Perdikakis, D. L. Bleuel, A. Couture, L. Crespo Campo, A. C. Dombos, R. Lewis, S. Mosby, S. Nikas, C. J. Prokop, T. Renstrom, B. Rubio, S. Siem, and S. J. Quinn, "Experimental neutron capture rate constraint far from stability," *Phys. Rev. Lett.*, vol. 116, p. 242502, Jun 2016.

[115] T. RAUSCHER, "The path to improved reaction rates for astrophysics," *International Journal of Modern Physics E*, vol. 20, no. 05, pp. 1071–1169, 2011.

[116] S. Goriely and J. P. Delaroche, "The isovector imaginary neutron potential: A key ingredient for the r-process nucleosynthesis," *Physics Letters B*, vol. 653, no. 2, pp. 178 – 183, 2007.

[117] P. Reinert, H. Krebs, and E. Epelbaum, "Semilocal momentum-space regularized chiral two-nucleon potentials up to fifth order," *Eur. Phys. J. A*, vol. 54, p. 86, 2018.

[118] A. Gezerlis, I. Tews, E. Epelbaum, M. Freunek, S. Gandolfi, K. Hebeler, A. Nogga, and A. Schwenk, "Local chiral effective field theory interactions and quantum monte carlo applications," *Phys. Rev. C*, vol. 90, p. 054323, Nov 2014.

[119] J. D. Holt, S. R. Stroberg, A. Schwenk, and J. Simonis, "Ab initio limits of atomic nuclei," 5 2019.

[120] https://www.trwhitehead.com/WLH.

[121] L. D. Landau *Sov. Phys. JETP*, vol. 3, p. 920, 1957.

[122] L. D. Landau *Sov. Phys. JETP*, vol. 5, p. 101, 1957.

[123] L. D. Landau *Sov. Phys. JETP*, vol. 8, p. 70, 1959.

[124] A. B. Migdal and A. I. Larkin *Sov. Phys. JETP*, vol. 18, p. 717, 1964.

[125] G. E. BROWN, "Landau, brueckner-bethe, and migdal theories of fermi systems," *Rev. Mod. Phys.*, vol. 43, pp. 1–14, Jan 1971.

[126] N. Iwamoto and C. J. Pethick, "Effects of nucleon-nucleon interactions on scattering of neutrinos in neutron matter," *Phys. Rev. D*, vol. 25, pp. 313–329, Jan 1982.

[127] P. Haensel and A. Jerzak, "Tensor forces and spin susceptibility of a fermi liquid," *Physics Letters B*, vol. 112, no. 4, pp. 285 – 288, 1982.

[128] S.-O. Bäckman, G. Brown, and J. Niskanen, "The nucleon-nucleon interaction and the nuclear many-body problem," *Physics Reports*, vol. 124, no. 1, pp. 1 – 68, 1985.

[129] J. Wambach, T. Ainsworth, and D. Pines, "Quasiparticle interactions in neutron matter for applications in neutron stars," *Nuclear Physics A*, vol. 555, no. 1, pp. 128 – 150, 1993.

[130] B. Friman and M. Rho, "From chiral lagrangians to landau-fermi liquid theory of nuclear matter," *Nuclear Physics A*, vol. 606, no. 1, pp. 303 – 319, 1996.

[131] O. Benhar and M. Valli, "Shear viscosity of neutron matter from realistic nucleon-nucleon interactions," *Phys. Rev. Lett.*, vol. 99, p. 232501, Dec 2007.

[132] A. Pastore, D. Davesne, Y. Lallouet, M. Martini, K. Bennaceur, and J. Meyer, "Nuclear response for the skyrme effective interaction with zero-range tensor terms. ii. sum rules and instabilities," *Phys. Rev. C*, vol. 85, p. 054317, May 2012.

[133] O. Benhar, A. Cipollone, and A. Loreti, "Weak response of neutron matter at low momentum transfer," *Phys. Rev. C*, vol. 87, p. 014601, Jan 2013.

[134] P. Haensel and J. Dabrowski, "The deformation of the fermi surface and magnetic susceptibility of neutron matter," *Nuclear Physics A*, vol. 254, no. 1, pp. 211 – 220, 1975.

[135] A. Schwenk and B. Friman, "Polarization contributions to the spin dependence of the effective interaction in neutron matter," *Phys. Rev. Lett.*, vol. 92, p. 082501, Feb 2004.

[136] E. Olsson, P. Haensel, and C. J. Pethick, "Static response of fermi liquids with tensor interactions," *Phys. Rev. C*, vol. 70, p. 025804, Aug 2004.

[137] S. Bacca, K. Hally, C. J. Pethick, and A. Schwenk, "Chiral effective field theory calculations of neutrino processes in dense matter," *Phys. Rev. C*, vol. 80, p. 032802, Sep 2009.

[138] C. J. Pethick and A. Schwenk, "Spin response of a normal fermi liquid with noncentral interactions," *Phys. Rev. C*, vol. 80, p. 055805, Nov 2009.

[139] D. Davesne, J. W. Holt, A. Pastore, and J. Navarro, "Effect of three-body forces on response functions in infinite neutron matter," *Phys. Rev. C*, vol. 91, p. 014323, Jan 2015.

[140] L. F. Roberts, G. Shen, V. Cirigliano, J. A. Pons, S. Reddy, and S. E. Woosley, "Protoneutron star cooling with convection: The effect of the symmetry energy," *Phys. Rev. Lett.*, vol. 108, p. 061103, Feb 2012.

[141] B. Bertoni, S. Reddy, and E. Rrapaj, "Electron-neutron scattering and transport properties of neutron stars," *Phys. Rev. C*, vol. 91, p. 025806, Feb 2015.

[142] T. Otsuka, T. Suzuki, R. Fujimoto, H. Grawe, and Y. Akaishi, "Evolution of nuclear shells due to the tensor force," *Phys. Rev. Lett.*, vol. 95, p. 232502, Nov 2005.

[143] T. Otsuka, T. Matsuo, and D. Abe, "Mean field with tensor force and shell structure of exotic nuclei," *Phys. Rev. Lett.*, vol. 97, p. 162501, Oct 2006.

[144] B. Friman and P. Haensel, "Tensor forces and collective excitations in nuclear matter," *Physics Letters B*, vol. 98, no. 5, pp. 323 – 327, 1981.

[145] L.-G. Cao, G. Colò, H. Sagawa, P. F. Bortignon, and L. Sciacchitano, "Effects of the tensor force on the multipole response in finite nuclei," *Phys. Rev. C*, vol. 80, p. 064304, Dec 2009.

[146] G. Co', V. De Donno, M. Anguiano, and A. M. Lallena, "Magnetic excitations in nuclei with neutron excess," *Phys. Rev. C*, vol. 85, p. 034323, Mar 2012.

[147] B. S. Pudliner, A. Smerzi, J. Carlson, V. R. Pandharipande, S. C. Pieper, and D. G. Ravenhall, "Neutron drops and skyrme energy-density functionals," *Phys. Rev. Lett.*, vol. 76, pp. 2416–2419, Apr 1996.

[148] B. A. Brown and A. Schwenk, "Constraints on skyrme equations of state from properties of doubly magic nuclei and ab initio calculations of low-density neutron matter," *Phys. Rev. C*, vol. 89, p. 011307, Jan 2014.

[149] A. Roggero, A. Mukherjee, and F. Pederiva, "Constraining the skyrme energy density functional with quantum monte carlo calculations," *Phys. Rev. C*, vol. 92, p. 054303, Nov 2015.

[150] M. Buraczynski and A. Gezerlis, "Static response of neutron matter," *Phys. Rev. Lett.*, vol. 116, p. 152501, Apr 2016.

[151] E. Rrapaj, A. Roggero, and J. W. Holt, "Microscopically constrained mean-field models from chiral nuclear thermodynamics," *Phys. Rev. C*, vol. 93, p. 065801, Jun 2016.

[152] T. Lesinski, M. Bender, K. Bennaceur, T. Duguet, and J. Meyer, "Tensor part of the skyrme energy density functional: Spherical nuclei," *Phys. Rev. C*, vol. 76, p. 014312, Jul 2007.

[153] G. A. Lalazissis, S. Karatzikos, M. Serra, T. Otsuka, and P. Ring, "Covariant density functional theory: The role of the pion," *Phys. Rev. C*, vol. 80, p. 041301, Oct 2009.

[154] G. Colò, H. Sagawa, S. Fracasso, and P. Bortignon, "Spin–orbit splitting and the tensor component of the skyrme interaction," *Physics Letters B*, vol. 646, no. 5, pp. 227 – 231, 2007.

[155] W. Zou, G. Colò, Z. Ma, H. Sagawa, and P. F. Bortignon, "Tensor correlations and evolution of single-particle energies in medium-mass nuclei," *Phys. Rev. C*, vol. 77, p. 014314, Jan 2008.

[156] F. Minato and C. L. Bai *Phys. Rev. Lett.*, vol. 110, p. 122501, Mar 2013.

[157] H. Sagawa and G. Colò, "Tensor interaction in mean-field and density functional theory approaches to nuclear structure," *Progress in Particle and Nuclear Physics*, vol. 76, pp. 76 – 115, 2014.

[158] G. Brown, S.-O. Bäckman, E. Oset, and W. Weise, "Calculation of spin-dependent parameters in the landau-migdal theory of nuclei," *Nuclear Physics A*, vol. 286, no. 1, pp. 191 – 210, 1977.

[159] C. Shen, U. Lombardo, N. Van Giai, and W. Zuo, "Neutrino mean free path in neutron stars," *Phys. Rev. C*, vol. 68, p. 055802, Nov 2003.

[160] W. Zuo, C. Shen, and U. Lombardo, "Landau parameters of nuclear matter in the spin and spin-isospin channels," *Phys. Rev. C*, vol. 67, p. 037301, Mar 2003.

[161] N. Kaiser, "Quasi-particle interaction in nuclear matter from chiral pion–nucleon dynamics," *Nuclear Physics A*, vol. 768, no. 1, pp. 99 – 117, 2006.

[162] J. Holt, N. Kaiser, and W. Weise, "Second-order quasiparticle interaction in nuclear matter with chiral two-nucleon interactions," *Nuclear Physics A*, vol. 870-871, pp. 1 – 22, 2011.

[163] J. W. Holt, N. Kaiser, and W. Weise, "Chiral fermi liquid approach to neutron matter," *Phys. Rev. C*, vol. 87, p. 014338, Jan 2013.

[164] D. R. Entem and R. Machleidt, "Accurate charge-dependent nucleon-nucleon potential at fourth order of chiral perturbation theory," *Phys. Rev. C*, vol. 68, p. 041001, Oct 2003.

[165] L. Coraggio, A. Covello, A. Gargano, N. Itaco, D. R. Entem, T. T. S. Kuo, and R. Machleidt, "Low-momentum nucleon-nucleon interactions and shell-model calculations," *Phys. Rev. C*, vol. 75, p. 024311, Feb 2007.

[166] E. Marji, A. Canul, Q. MacPherson, R. Winzer, C. Zeoli, D. R. Entem, and R. Machleidt, "Nonperturbative renormalization of the chiral nucleon-nucleon interaction up to next-to-next-to-leading order," *Phys. Rev. C*, vol. 88, p. 054002, Nov 2013.

[167] L. Coraggio, J. W. Holt, N. Itaco, R. Machleidt, and F. Sammarruca, "Reduced regulator dependence of neutron-matter predictions with perturbative chiral interactions," *Phys. Rev. C*, vol. 87, p. 014322, Jan 2013.

[168] F. Sammarruca, L. Coraggio, J. W. Holt, N. Itaco, R. Machleidt, and L. E. Marcucci, "Toward order-by-order calculations of the nuclear and neutron matter equations of state in chiral effective field theory," *Phys. Rev. C*, vol. 91, p. 054311, May 2015.

[169] E. Epelbaum, H.-W. Hammer, and U.-G. Meissner, "Modern theory of nuclear forces," *Rev. Mod. Phys.*, vol. 81, pp. 1773–1825, Dec 2009.

[170] V. Bernard, E. Epelbaum, H. Krebs, and U.-G. Meissner, "Subleading contributions to the chiral three-nucleon force: Long-range terms," *Phys. Rev. C*, vol. 77, p. 064004, Jun 2008.

[171] V. Bernard, E. Epelbaum, H. Krebs, and U.-G. Meissner, "Subleading contributions to the chiral three-nucleon force. ii. short-range terms and relativistic corrections," *Phys. Rev. C*, vol. 84, p. 054001, Nov 2011.

[172] C. Drischler, K. Hebeler, and A. Schwenk, "Chiral interactions up to next-to-next-to-next-to-leading order and nuclear saturation," *Phys. Rev. Lett.*, vol. 122, p. 042501, Jan 2019.

[173] J. W. Holt and N. Kaiser, "Equation of state of nuclear and neutron matter at third-order in perturbation theory from chiral effective field theory," *Phys. Rev. C*, vol. 95, p. 034326, Mar 2017.

[174] J. W. Holt, N. Kaiser, G. A. Miller, and W. Weise, "Microscopic optical potential from chiral nuclear forces," *Phys. Rev. C*, vol. 88, p. 024614, Aug 2013.

[175] J. W. Holt, N. Kaiser, and G. A. Miller, "Microscopic optical potential for exotic isotopes from chiral effective field theory," *Phys. Rev. C*, vol. 93, p. 064603, Jun 2016.

[176] D. H. Youngblood, H. L. Clark, and Y.-W. Lui, "Incompressibility of nuclear matter from the giant monopole resonance," *Phys. Rev. Lett.*, vol. 82, pp. 691–694, Jan 1999.

[177] N. Kaiser, "Quartic isospin asymmetry energy of nuclear matter from chiral pion-nucleon dynamics," *Phys. Rev. C*, vol. 91, p. 065201, Jun 2015.

[178] G. Bertsch, D. Cha, and H. Toki *Phys. Rev. C*, vol. 24, pp. 533–540, Aug 1981.

[179] M. Bender, J. Dobaczewski, J. Engel, and W. Nazarewicz, "Gamow-teller strength and the spin-isospin coupling constants of the skyrme energy functional," *Phys. Rev. C*, vol. 65, p. 054322, May 2002.

[180] H. A. Bethe *Ann. Rev. Nucl. Part. Sci.*, vol. 38, p. 1, 1988.

[181] P. Donati, P. M. Pizzochero, P. F. Bortignon, and R. A. Broglia, "Temperature dependence of the nucleon effective mass and the physics of stellar collapse," *Phys. Rev. Lett.*, vol. 72, p. 2835, 1994.

[182] N.-C. Chao, J. W. Clark, and C.-H. Yang *Nucl. Phys.*, vol. A179, p. 320, 1972.

[183] O. Sjoberg *Nucl. Phys.*, vol. A265, p. 511, 1976.

[184] N. Chamel *Mon. Not. R. Astron. Soc.*, vol. 388, p. 737, 2008.

[185] G. E. Brown, J. H. Gunn, and P. Gould *Nucl. Phys.*, vol. 46, p. 598, 1963.

[186] G. F. Bertsch and T. T. S. Kuo *Nucl. Phys.*, vol. A112, p. 204, 1968.

[187] C. Mahaux, P. F. Bortignon, R. A. Broglia, and C. H. Dasso *Phys. Rep.*, vol. 120, p. 1, 1985.

[188] M. Farine, J. M. Pearson, and F. Tondeur *Nucl. Phys.*, vol. A696, p. 396, 2001.

[189] J. M. Pearson and S. Goriely *Phys. Rev. C*, vol. 64, p. 027301, 2001.

[190] B.-A. Li and X. Han *Phys. Lett. B*, vol. 727, p. 276, 2013.

[191] Z. Zhang and L.-W. Chen *Phys. Rev. C*, vol. 93, p. 034335, 2016.

[192] W. Zuo, I. Bombaci, and U. Lombardo *Phys. Rev. C*, vol. 60, p. 024605, 1999.

[193] W. Zuo, A. Lejeune, U. Lombardo, and J. F. Mathiot *Eur. Phys. J. A*, vol. 14, p. 469, 2002.

[194] D. D. S. Coupland, M. Youngs, Z. Chajecki, W. G. Lynch, M. B. Tsang, Y. X. Zhang, M. A. Famiano, T. K. Ghosh, B. Giacherio, M. A. Kilburn, J. Lee, H. Liu, F. Lu, P. Morfouace, P. Russotto, A. Sanetullaev, R. H. Showalter, G. Verde, and J. Winkelbauer *Phys. Rev. C*, vol. 94, p. 011601, 2016.

[195] V. Baran, M. Colonna, V. Greco, and M. D. Toro *Phys. Rept.*, vol. 410, p. 335, 2005.

[196] J. Rizzo, M. Colonna, and M. D. Toro *Phys. Rev. C*, vol. 72, p. 064609, 2005.

[197] Y. Zhang, M. B. Tsang, Z. Li, and H. Liu *Phys. Lett. B*, vol. 732, p. 186, 2014.

[198] B.-A. Li, B.-J. Cai, L.-W. Chen, and J. Xu, "Nucleon effective masses in neutron-rich matter," *Progress in Particle and Nuclear Physics*, vol. 99, pp. 29 – 119, 2018.

[199] W. Tornow, Z. P. Chen, and J. P. Delaroche, "Proton mean field in 40Ca between -60 MeV and +200 MeV deduced from a dispersive optical-model analysis," *Phys. Rev. C*, vol. 42, pp. 693–706, Aug 1990.

[200] C. H. Johnson and C. Mahaux, "Neutron 40Ca mean field between -80 and +80 MeV from a dispersive optical-model analysis," *Phys. Rev. C*, vol. 38, pp. 2589–2609, Dec 1988.

[201] T. R. Whitehead, Y. Lim, and J. W. Holt, "Microscopic global optical potential for rare isotope reactions," 9 2020.

[202] F. Sammarruca, L. E. Marcucci, L. Coraggio, J. W. Holt, N. Itaco, and R. Machleidt, "Nuclear and neutron matter equations of state from high-quality potentials up to fifth order of the chiral expansion," 2018.